

MITIGATING THE EFFECTS OF LOW-INERTIA ON HVDC-RICH AC GRIDS

by Khadijat Jose



School of Engineering
Cardiff University
Cardiff, United Kingdom

Yr Ysgol Peirianeg
Prifysgol Caerdydd
Caerdydd, Deyrnas Unedig

*THESIS SUBMITTED FOR THE DEGREE OF
DOCTOR OF PHILOSOPHY*

Cardiff, 2019

To my family

Declaration

This work has not been submitted in substance for any other degree or award at this or any other university or place of learning, nor is being submitted concurrently in candidature for any degree or other award.

Signed: Jose Khadijat Folashade  (candidate) Date: 22/05/2019

STATEMENT 1

This thesis is being submitted in partial fulfilment of the requirements for the degree of Doctor of Philosophy (PhD)

Signed: Jose Khadijat Folashade  (candidate) Date: 22/05/2019

STATEMENT 2

This thesis is the result of my own independent work/investigation, except where otherwise stated, and the thesis has not been edited by a third party beyond what is permitted by Cardiff University's Policy on the Use of Third Party Editors by Research Degree Students. Other sources are acknowledged by explicit references. The views expressed are my own.

Signed: Jose Khadijat Folashade  (candidate) Date: 22/05/2019

STATEMENT 3

I hereby give consent for my thesis, if accepted, to be available online in the University's Open Access repository and for inter-library loan, and for the title and summary to be made available to outside organisations.

Signed: Jose Khadijat Folashade  (candidate) Date: 22/05/2019

Contents

Declaration	i
Acknowledgements	vi
Abstract	vii
Abbreviations	viii
List of Figures	x
List of Tables	xiv
Chapter 1 Introduction	xv
1.1 Background	2
1.2 Objectives of this thesis	6
1.3 Thesis structure	7
1.4 List of Publications	8
1.4.1 Journal Papers	8
1.4.2 Conference Papers	8
1.4.3 International Workshops and Presentations	9
1.5 List of Contributions	9
Chapter 2 Literature Review	11
2.1 Introduction	12
2.2 Power System Changes	12
2.2.1 Future Energy Scenarios	13
2.3 Wind Technology	15
2.3.1 Fixed Speed Wind Turbines	17
2.3.2 Limited Variable Speed Wind Turbines with Variable Rotor Resistance	18
2.3.3 Variable Speed Wind Turbines	19
2.3.3.1 VSWTs with Partial-Scale Converter	19
2.3.3.2 VSWTs with Full Power Converter	20
2.3.4 Summary of WT Topologies	21
2.4 High Voltage Direct Current Transmission Systems	22

2.4.1	Line Commutated Converters.....	23
2.4.2	Voltage Source Converters.....	24
2.4.2.1	Two-Level Converters	25
2.4.2.2	Three-Level Converters	26
2.4.2.3	Modular Multilevel Converters.....	26
2.5	Frequency Regulation in Power Systems.....	28
2.5.1	Mandatory Frequency Response	29
2.5.2	Enhanced Frequency Response.....	30
2.6	Inertia.....	31
2.7	Grid Code Requirements on WTs and HVDC for Frequency Support.....	34
2.7.1	Limited Frequency Sensitive Mode	35
2.7.2	Frequency Sensitive Mode	36
2.8	Inertia Response from WTs	37
2.8.1	Synthetic Inertia or Inertia Emulation	38
2.8.2	Temporary Overproduction or Fast Power Reserve.....	39
2.8.3	Recovery Phase.....	40
2.9	Inertia Response from HVDC.....	41
2.10	Summary.....	44
Chapter 3 Inertial Contribution from VSWTs.....		46
3.1	Introduction	47
3.2	Control of VSWTs	48
3.2.1	Aerodynamic Model	49
3.2.2	Drive Train Model.....	50
3.2.3	Electrical Model of the PMSG	50
3.2.4	Back-to-Back Converters Controls.....	50
3.3	Inertial Contribution from WTs.....	53
3.4	Test System Modelling.....	54
3.5	Frequency Support at Different Penetration Levels	56
3.6	Inertial Contribution from PMSG-WTs - Case Study.....	57
3.6.1	Impact of Wind Speed on Frequency Support	58
3.6.2	Impact of Filters on WT Recovery Power	59
3.6.3	Energy Capability of WTs due to Increased Torque	60
3.7	Summary.....	62

Chapter 4 Coordination of Fast Frequency Support from Multi-Terminal HVDC Grids and Offshore Wind Farms	64
4.1 Introduction	65
4.2 Modelling and Control of DC Grid Converters	65
4.2.1 Droop Control	66
4.3 VSC Modelling	67
4.3.1 Inner-loop Controllers	68
4.3.2 Outer-loop Controllers	69
4.3.3 DC Link	70
4.4 Wind Farm Converter Control	71
4.4.1 WTs Temporary Overproduction	71
4.5 Simplified power system model	72
4.6 MTDC Fast Frequency Support Schemes	74
4.6.1 Coordinated Control Scheme	74
4.6.2 Alternative Coordinated Control Scheme	75
4.6.3 Dual-Loop Control Scheme	76
4.6.4 Drawbacks of Fast Frequency Control Schemes	77
4.7 Auxiliary Dead-band Controller	78
4.8 Test System	80
4.9 Small-Signal Stability Study	81
4.10 Simulations and Analysis	83
4.10.1 Case 1 – Single Imbalance	84
4.10.2 Case 2 – Opposing Frequency Trends	87
4.11 Fast Frequency Controllers with Proposed ADC Scheme	90
4.12 DC Grids with Different Frequency Control Modes	91
4.13 Summary	92
Chapter 5 Experimental Validation of Fast Frequency Support from MTDC Grids	94
5.1 Introduction	95
5.2 Description of Experimental Platform	95
5.2.1 VSC-HVDC Test Rig	96
5.2.2 DC Network Cabinet	96
5.2.3 AC Grid Simulator	97
5.2.4 Real Time Digital Simulator	98

5.3	RSCAD Modelling	99
5.4	Master-Slave Control	100
5.5	Experimental System Setup	102
5.6	Simulation Setup	105
5.7	Experimental Results	105
5.7.1	No Control	106
5.7.2	ACC scheme fitted in VSC2 only	107
5.7.3	DLC scheme fitted in VSC2 only	108
5.7.4	ACC scheme fitted in all converters	109
5.7.5	DLC scheme fitted in all converters	110
5.8	Comparison of Simulation and Experimental Results	111
5.8.1	Experimental Validation of Auxiliary Dead-band Controller	113
5.9	Summary	114
Chapter 6 Conclusions		117
6.1	General Conclusions	118
6.1.1	Inertial contribution from large scale VSWTs	118
6.1.2	Fast frequency support from MTDC grids and offshore wind farms	119
6.1.3	Experimental validation of fast frequency support from MTDC Grids	120
6.2	Future Research	121
6.2.1	Frequency Support from VSWTs considering varying wind speeds	121
6.2.2	Small-signal study of reduced 29 bus GB model considering increased VSC-HVDC penetration in grid	121
6.2.3	Selective frequency support from onshore ac grids connected to MTDC grids	121
Appendix I		124
Appendix II		128
Appendix III		129
Appendix IV		130
References		134

Acknowledgements

I would like to express my deepest and sincere gratitude to my brilliant supervisors, Prof. Jun Liang and Dr Carlos Ugalde-Loo, who continuously provided me with invaluable technical guidance, advice and support throughout my PhD study. Many thanks to Prof Jenkins for the advice and feedback received during our numerous CIREGS meetings. I would also like to thank Dr Daniel Adeuyi, Dr Tibin Joseph and Dr Gen Li for their collaborations, time, support and assistance in setting-up the experiment platform in the power electronic lab. In addition, I would like to thank the Engineering and Physical Sciences Research Council (EPSRC), for the funding me and giving me opportunity to carry out this PhD research.

I would also like to thank all my colleagues and friends at Cardiff University for all the motivation and inspiration I got from them. They have all made this time an interesting one while being supportive and understanding the ups and downs of a PhD study. Finally, I would like to thank my parents, my siblings and my husband, Adesegun for their love, prayers, support and encouragement. I am most grateful to them for taking care of Ahmed while I studied.

Abstract

The integration of large-scale power from renewable energy sources (RESs) via high voltage direct current (HVDC) transmission will contribute to the achievement of energy targets made by the government of several nations. This will help to reduce greenhouse gas emissions and combat climate change. With variable-speed wind turbines (VSWTs), maximum wind energy can be captured; additionally, multi-terminal HVDC grids (MTDC) can help to connect offshore wind farms (OWFs), solar farms and several countries, thus, aiding cross border trading, balancing services and RES integration. A major component of these technologies is power electronics which makes them not contribute to the system inertia.

The research work presented in this thesis is aimed at investigating the effects of reduced system inertia in an ac grid rich in power electronics (i.e. HVDC and VSWTs) and proposing measures to mitigate these effects. The main contributions of this research work are: (1) investigating the effects of large-scale connection of VSWTs to the GB power system, (2) analysis of inertial contribution of VSWTs, (3) coordination of fast frequency support from MTDC grids and (4) experimental validation of frequency control schemes, including a proposed auxiliary dead-band controller (ADC).

To investigate the inertial contribution from VSWTs, a test system consisting of a three-machine Great Britain (GB) power system connecting full power converter-based VSWTs was modelled. In this test system, the wind generation capacity was varied and the effect on the system frequency response was studied. It was observed that the system frequency deviation and rate of change of frequency (*RoCoF*) increased with the wind penetration increase. This study was followed by analysing the VSWT synthetic inertia capability. The temporary overproduction strategy which allows the release of stored kinetic energy during power imbalances was used.

HVDC grids may provide fast frequency support to ac grids with the aid of supplementary control algorithms. Three fast frequency control schemes are presented. These supplementary control schemes are fitted with all the converters within a four-terminal HVDC grid connecting an OWF and three onshore ac grids. During periods of frequency support, undesirable power flows and reduced power transfers occurred within the grid. To prevent these issues, an ADC algorithm was proposed. The results show that the ADC improves the performance of the supplementary frequency controllers.

An experimental test platform was designed to validate the fast frequency control algorithms and the ADC performance. The three-machine GB power system was implemented in a real-time digital simulator which was connected to a meshed three-terminal HVDC test rig. With this system, the frequency control schemes and ADC were validated.

Abbreviations

ACC	Alternative coordinated control
ADC	Auxiliary dead-band controller
BJT	Bipolar junction transistor
CC	Coordinated control
DFIG	Doubly-fed induction generator
DLC	Dual-loop control
EFR	Enhanced frequency response
ENTSOE	European network of transmission systems operators for electricity
FES	Future energy scenario
FPC	Full power converter
FSWT	Fixed-speed wind turbine
GB	Great Britain
GS	Grid simulator
GSC	Grid side converter
GTAI	Analogue input
GTAO	Analogue output
HiL	Hardware-in-the-loop
HVAC	High voltage alternating current
HVDC	High voltage direct current
IE	Inertia emulation
IGBT	Insulated-gate bipolar transistor
IR	Inertial response
LCC	Line commutated converter
LVSWT	Limited variable-speed wind turbine
MFR	Mandatory frequency response
MMC	Modular multilevel converter
MOSFET	Metal–oxide–semiconductor field-effect transistor
MPP	Maximum power point
MTDC	Multiterminal HVDC
NPC	Neutral-point-clamped
OWF	Offshore wind farm

PCC	Point of common coupling
PLL	Phase locked loop
PMSG	Permanent magnet synchronous generator
PSCAD	Power systems computer aided design
PWM	Pulse-width modulation
ROCOF	Rate of change of frequency
RTDS	Real-time digital simulator
SI	Synthetic inertia
SP	Slow progression
SQSS	Security and quality of supply standard
TD	Two degrees
TO	Temporary overproduction
TSO	Transmission system operator
UK	United Kingdom
VSC	Voltage source converter
VSWT	Variable-speed wind turbine
WPP	Wind power plant
WRIG	Wound rotor induction generator
WT	Wind turbine

List of Figures

Figure 1.1: Average wind profile in Europe (Source: EEA)[5].	2
Figure 1.2: HVDC links around the North Sea	3
Figure 2.1: Global cumulative installed wind power capacity to 2016 [39].	15
Figure 2.2: Comparison of WT sizes to world landmarks [44].	16
Figure 2.3: Conceptual scheme of a general WT [12].	17
Figure 2.4: FSWT - with SCIG [12].	18
Figure 2.5: LVSWT - with WRIG [12].	18
Figure 2.6: VSWT with partial-scale converter or DFIG-WT [12].	20
Figure 2.7: VSWT with FPC – can use SCIG, WRSG or PMSG [12].	21
Figure 2.8: Six-pulse LCC with thyristors [58].	24
Figure 2.9: Two-level VSC [61].	25
Figure 2.10: Three-level NPC converter [61].	26
Figure 2.11: Schematic of an MMC [61].	27
Figure 2.12: System frequency control [76].	29
Figure 2.13: Frequency response services [18].	30
Figure 2.14: Operation in limited frequency sensitive mode. Requirements from (a) generating units and WPPs, (b) dc Converters [87].	35
Figure 2.15: Interpretation of primary, secondary and high frequency response [86].	36
Figure 2.16: UK Grid Code - Minimum active power change for primary, secondary and high frequency response for WPPs in the event of a system frequency deviation of 0.5 Hz [86].	37
Figure 2.17: Synthetic inertia or inertia emulation scheme.	39
Figure 2.18: Temporary overproduction scheme.	40
Figure 2.19: Description of inertia emulation by temporary overproduction and recovery period. (a) WT rotor speed (green) and WT power (blue); and (b) System Frequency.	41
Figure 3.1: PMSG-WT control scheme.	48
Figure 3.2: GSC control scheme for PMSG-WTs.	51
Figure 3.3: NSC control scheme for PMSG-WTs.	52

Figure 3.4: Summary of VSWT control scheme.....	52
Figure 3.5: Temporary overproduction scheme for frequency support as implemented in PSCAD.....	54
Figure 3.6: Three-machine model	55
Figure 3.7: Modified three-machine model	55
Figure 3.8: Impact of increasing wind penetration without supplementary controllers for frequency response. System frequency response after 1800 MW generation loss.....	57
Figure 3.9: Effect of changing wind speed: System response after 1800 MW generation loss (a) System frequency response (b) Power supply from wind farm after imbalance.	59
Figure 3.10: Impact of step torque controls - System response after 1800 MW generation loss (a) System frequency response (b) Power supply from wind farm after imbalance (c) Change in WT torque (d) Change in WT rotor speed.	60
Figure 3.11: Effect of changing the step torque - System response after 1800 MW generation loss: (a) System frequency response, (b) Power supply from wind farm after imbalance.	62
Figure 4.1: Droop control (inner loop not shown as its same as master-slave control).....	67
Figure 4.2: Three-phase representation of a VSC.	67
Figure 4.3: Inner loop control of a VSC.	69
Figure 4.4: Droop control of VSC in study.....	70
Figure 4.5: Wind farm converter control.	71
Figure 4.6: DC voltage - frequency droop for frequency support from wind farms.	72
Figure 4.7: Simplified power system model.	73
Figure 4.8: CC scheme.....	75
Figure 4.9: ACC scheme.....	76
Figure 4.10: DLC Scheme.	77
Figure 4.11: Proposed auxiliary dead-band controller.	78
Figure 4.12: Four terminal VSC-HVDC test system.....	81

Figure 4.13: Response to 10% step increase in wind farm power output. Comparison of small signal model (SS) to averaged model (AM). (a) Power variation in OWF and Grids 1, 2 and 3. (b) DC voltage variation.	82
Figure 4.14: Small-signal stability study of the system. (a) Root locus of the system for variations in droop gain kfv . (b) Root locus of the system for variations in droop gain kpv . In both cases, a zoomed view of the dominant eigenvalues is given by the right-hand side plots.	83
Figure 4.15: Case 1, ACC scheme. System response after a generation loss of 1800 MW in Grid 2.	85
Figure 4.16: Case 1, CC scheme. System response after a generation loss of 1800 MW in Grid 2.	86
Figure 4.17: Case 1, DLC scheme. System response after a generation loss of 1800 MW in Grid 2.	87
Figure 4.18: Case 2, ACC scheme. System response after a generation loss of 1800 MW in Grid 2 and 900 MW demand loss at Grid 3.	88
Figure 4.19: Case 2, CC Scheme. System response after a generation loss of 1800 MW in Grid 2 and 900 MW demand loss in Grid 3.	89
Figure 4.20: Case 2. DLC scheme. System response after a generation loss of 1800 MW in Grid 2 and 900 MW demand loss at Grid 3.	90
Figure 4.21: Comparison of all schemes. System response after a generation loss of 1800 MW in Grid 2 and 900 MW demand loss at Grid 3.	91
Figure 4.22: Effect of the ADC scheme on different control modes in an MTDC system. Frequency variations in: (a) Grid 2; (b) Grids 1 and 3. (c) DC voltage variation. Power injections in (d) VSC2; (e) Grid 1; (f) Grid 3.	92
Figure 5.1: Illustrative diagram of experimental test rig.	96
Figure 5.2: VSC experimental test rig set-up: (a) DC network cabinet, VSC 1,2 & 3 cabinet; Transformers 1,2 & 3 and dSPACE control desk (b) Interior of VSC cabinet and dSPACE unit.	97
Figure 5.3: Real-time system setup: (a) AC Grid Simulator; (b) RTDS.	98
Figure 5.4 : Three-machine GB system.	99
Figure 5.5: Three-machine GB system: Comparison of PSCAD results vs RSCAD results.	100

Figure 5. 6: Master-slave control - master terminal.	101
Figure 5. 7: Master-slave control - slave terminal.....	101
Figure 5.8: Real-time HiL implementation.....	102
Figure 5.9: Signal transmission between RTDS and VSC Test-rig	103
Figure 5.10: System response in VSC2 power setpoint change (a) DC Voltage variation (b) Power flow in converters (c)England & Wales generator power (d) AC grid 2 frequency (e) AC grid current.....	104
Figure 5.11: Three-machine GB system connected to three-terminal VSC-MTDC system in PSCAD.....	105
Figure 5.12: Experimental results: System response after loss of 1320 MW (No Control).....	107
Figure 5.13: Experimental results: System response after loss of 1320 MW (ACC FS fitted in VSC2 only).	108
Figure 5.14: Experimental results: System response after loss of 1320 MW (DLC FS fitted in VSC2 only).	109
Figure 5.15: Experimental results: System response after loss of 1320 MW (ACC FS fitted in all converters).....	110
Figure 5.16: Experimental results: System response after loss of 1320 MW (DLC FS fitted in all converters).....	111
Figure 5.17: PSCAD results (left column) and experimental results (right column) of system response due to 1320 MW generation loss, ACC fitted in all converters. (a) DC Voltage (pu) (b) VSCs 1, 2 and 3 Power (pu) and (c) Frequency of AC Grids 1, 2 and 3.	113
Figure 5.18: PSCAD results (left column) and experimental results (right column) of system response due to 1320 MW generation loss, ACC+ADC fitted in all converters. (a) DC Voltage (pu) (b)VSCs 1, 2 and 3 Power (pu) and (c) Frequency of AC Grids 1, 2 and 3.....	114
Figure A1. 1: Three-machine GB system in PSCAD.....	127
Figure A4. 1: : DC Network Cabinet.....	133

List of Tables

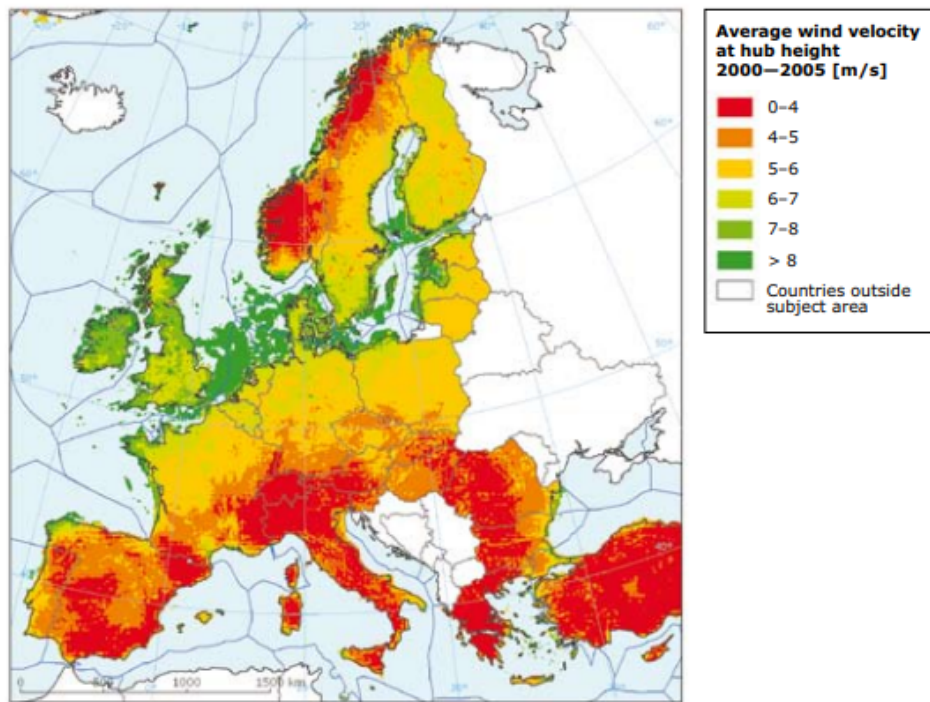
Table 2.1: Expected generation capacity by type in 2030 and 2050 [37].....	14
Table 2.2: Key VSC-HVDC projects (commissioned and in planning).....	28
Table 2.3: Inertia constant of different machines [24], [31], [83].....	33
Table 2.4: Inertia response requirements from different TSOs [25].	44
Table 3.1: RoCoF and frequency deviation of case study while varyong step torque.	61
Table 4.1: WT parameters.....	72
Table 4.2: ADC XNOR logic.....	79
Table 4.3: Frequency control schemes during single imbalance.....	87
Table 4.4: Comparison of support schemes during multiple imbalances.	90
Table 4.6: Control modes of the converters.....	92
Table 5.1: Control mode of the converters	106
Table 5.2: Experimental and PSCAD base values	112
Table A1. 1: Generator parameters (in per unit)	124
Table A1. 2: Governor parameters	125
Table A1. 3: Turbine parameters.....	125
Table A1. 4: AC1A exciter	126
Table A2. 1: Back-to-back converters control parameters	128
Table A2. 2: Aerodynamic model parameters	128
Table A3. 1: Parameters of VSCs and droop coefficients [28].....	129
Table A3. 2: AC System Parameters [136].....	129
Table A4. 1: VSC test rig specifications.....	130
Table A4. 2: Real time simulator specifications.	130
Table A4. 3: Grid simulator specifications.	130
Table A4. 4: Parameters of experimental VSC test rig.....	131
Table A4. 5: Technical parameters of MTDC rig in PSCAD.	132

Chapter 1

Introduction

1.1 Background

The use of fossil fuels to generate electricity must be reduced significantly because they are a major contributor to greenhouse gas emissions which are causing the threat of climate change and global warming. In addition, these fossil fuels are expensive and slowly depleting, raising concerns about securing our energy supply. Considering this, the fossil fuels are being replaced by renewable sources of generation such as wind and solar. The European Environment Agency reports that renewables have cut Europe's carbon emissions by 10% in 2015 and reduced fossil fuel dependency [1]. There has been an increased renewable share in Europe, with countries such as Sweden (60%), Norway (98%) and Germany (42%) leading the way [2]–[4].



Source: EEA, 2008.

Figure 1.1: Average wind profile in Europe (Source: EEA)[5].

Wind is an abundant resource in Europe especially around the United Kingdom (UK) and the North Sea. The total net installed capacity of wind is currently 169 GW in Europe, making wind the second largest form of power generation in this region [6]. Figure 1.1 shows the average wind profile in Europe. In 2017, 3.154

GW of offshore wind power was installed. This makes a total installed offshore wind capacity of 15.780 GW in Europe, with 94 grid connected wind farms and 4,149 wind turbines (WTs) [6]. Some newly installed offshore wind farms (OWFs) include Race Bank (498 MW in the UK), Dudgeon East (402 MW – UK) and Veja Mate (402 MW – Germany) among others [7]. About 66.5 GW offshore wind capacity is expected by 2030 [8]. Although OWFs are located very far away from load centres, they are preferred because wind speeds are higher offshore, which means higher power generation is possible. Also, it is easier to gain planning permission for OWFs than it is for onshore [9]. AC transmission proves economically unsuitable for distances higher than 50 km for cables and 600-800 km for overhead lines [10]–[12]. This is because of higher power losses with ac transmission with increasing lengths. High-voltage direct current (HVDC) transmission provides a better solution for integrating these sources of renewable energy as it can transfer large amounts of power from longer distances to load centres with lower losses and flexible power control [13].

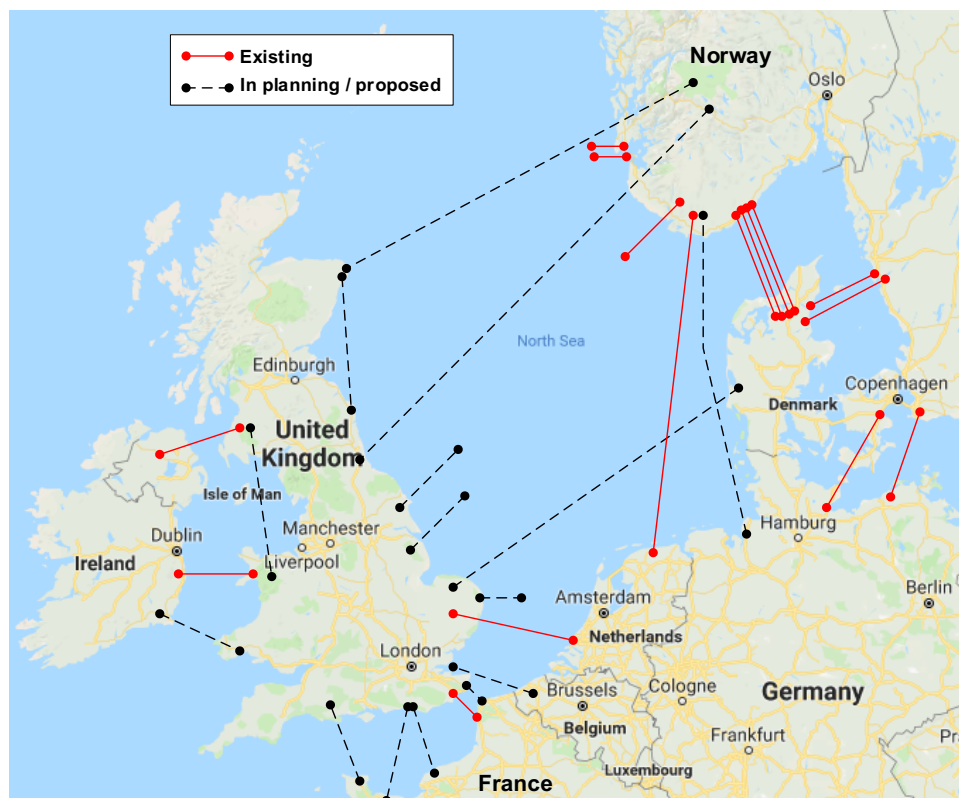


Figure 1.2: HVDC links around the North Sea

Multi-terminal HVDC (MTDC) grids can be formed by interconnecting existing HVDC links to additional VSCs in meshed or radial topologies. This will enable inter-border trading of power and may allow for an improved reliability with minimised assets [13]. In the middle of the Baltic Sea, the Kriegers Flak – Combined Grid Solution [14] will connect OWFs, Baltic 1 (48 MW), Baltic 2 (288 MW) and Kriegers flak (600 MW) to Germany and Denmark [14]. When the wind farms are generating, the power will be transferred to both countries and when wind output is low, the cable will work as a 400 MW interconnector transferring power between Germany and Denmark and vice versa [14]. The project will be operational by Q3 2019. The proposal of the North Sea Offshore Grid (NSOG) is another example of a MTDC grid which can interconnect the grids of the surrounding countries with offshore wind power. The NSOG will bring about economic, environmental and security of supply to the participating countries [15], [16]. Figure 1.2 shows the HVDC links around this region. Although the transition to a cleaner low-carbon power system will lead to energy provision which is sustainable, affordable and secure, there are still several challenges which the power system operator will face in integrating offshore wind energy to the grid.

WTs are supported by power electronic converters which allow a proper control of reactive and active power flow to and from the generator. Power electronics also allow for optimal wind power extraction and variable-speed operation [12]. However, this makes their operation asynchronous with the grid; i.e. the rotational speed of the WTs is decoupled from the grid frequency. It is expected that the OWFs will replace conventional synchronous generators, with bulk power from large OWFs being connected to the grid by HVDC converters [17].

Synchronous generators naturally respond to a frequency change within the power system, this property is called inertia. Inertia enables synchronous generators to quickly release/absorb kinetic energy from their rotating shafts to oppose a frequency decline/rise. With the power electronics-based WTs and HVDC based transmission replacing synchronous generators and HVAC transmission, the total power system inertia will reduce. In a power system with low inertia, the frequency stability changes. When there is a sudden loss of demand/supply, there can be larger frequency swings and higher rate of change of frequency (*RoCoF*) which affects

the protection strategies and generally the operation and security of the power system [18]. Also, the short circuit levels in a power system with low inertia is reduced compared to a system with high inertia. Low short circuit levels indicate a power system is weak and this leads to power quality issues and higher voltage dips. Synchronous generators in a conventional power system contribute to short-circuit levels and inertia. As these are being phased out of operation, the transmission system operator (TSO) needs to make changes to ensure a safe and secure operation [18], [19].

It is important to study the effect of the large penetration of these power electronics-based generation and transmission technologies on the ac system they are connected to. Also, it is vital to study and quantify the provision of ancillary services such as frequency support from WTs and HVDC transmission to guarantee a reliable and quality operation of the future grids. Studies in literature have shown that WTs and HVDC can support the system frequency. Authors in [20]–[24] have proposed control schemes for WTs to automatically detect when there is an ongoing frequency event and to also provide additional power to the grid. Some proposed schemes for providing inertia support from WTs include the synthetic inertia and temporary overproduction schemes. These control schemes extract the kinetic energy stored in the rotating shaft of the WTs. The amount of energy extracted can either be proportional to the *RoCoF* or be a predetermined amount of energy. Although these schemes for providing inertial support are in existence, the authors have not quantified their inertial contribution capability and the effects these controllers may have on a power system.

Also, authors have not investigated the negative effects of WT recovery period on the system frequency. The recovery period is the period after the WT stops providing inertial support, the WT output reduces below its nominal output level before the frequency event and the rotor begins to speed up to return to its original output. This period of recovery influences the system frequency as it may cause an additional frequency decline when the WT is not producing optimal power. This is described further in Section 2.8.3. Authors in [25] proposed a control scheme which reduces the recovery behaviour by extending the recovery time so as to have less effect on the system frequency. The paper showed that the longer the recovery

period the less effect it would have on the frequency. However, they have not shown other means of reducing the recovery period and factors which cause the recovery power to be high. A sensitivity study on these factors will prove beneficial in improving the inertial contribution capability of WTs.

When there is a sudden loss of generation/increase in demand in an ac system, the VSC-HVDCs do not automatically detect this because of their decoupling from the grid. Research on provision of fast frequency support from HVDC transmission systems has been studied vastly in [20], [26]–[29] who have proposed droop controls and inertia support from the capacitances in the dc link and MMC bridges. The behaviour of these controls has however been only studied when the control schemes are placed in only one converter in the MTDC grid. This thesis will study the fast frequency controllers when they are placed in all converters in the dc grid. Also, strategies to coordinate fast frequency support from MTDC grids to connected onshore ac grids will be proposed.

1.2 Objectives of this thesis

This thesis focuses on the analysis and control of variable speed WTs (VSWTs) and MTDC schemes to mitigate low inertia effects caused by their penetration into the power system. The main research objectives of this work include:

- To investigate the frequency effects of increased penetration of wind on a low inertia power system and analyse the inertial contribution from large scale VSWTs.
- To compare the capability of the fast frequency control schemes when placed in all converters in the MTDC grid and design a control system to support the coordination of frequency support in MTDC grids.
- To develop a mathematical model of a MTDC grid, with droop controllers and supplementary frequency control schemes, to carry out small-signal stability studies.
- To experimentally validate the performance of the proposed frequency controller in a hardware-in-the-loop test system.

1.3 Thesis structure

The structure of the thesis is as follows:

Chapter 2 – Literature Review

This chapter addresses HVDC and OWF technology for future power systems. The challenges due to the changes in the generation mix are discussed and current research on inertia support from VSWTs and HVDC is reviewed. The current grid code for frequency regulation in the UK, which aids understanding the TSOs needs from the new technologies, are discussed.

Chapter 3 – Inertial Contribution from Large Scale VSWTs

In this chapter, full power converter (FPC) VSWTs are studied. A simplified three machine power system is modelled and analysis of the inertial contribution of WT generators to the power system is made. A supplementary controller designed to enable WTs to provide inertial support is discussed and the effectiveness of this controller is tested. The frequency support capability of the WTs is analysed for different wind power penetration levels, wind speeds and control parameter settings. The impact of these parameters on wind recovery power after providing inertial response is also considered. These studies were carried out in the PSCAD/EMTDC simulation platform.

Chapter 4 – Coordination of Fast Frequency Support from Multi-Terminal HVDC Grids and Offshore Wind Farms

This chapter addresses the need for frequency support in onshore ac grids when connected by MTDC grids. The behaviour of the MTDC system when all the onshore VSCs are upgraded with supplementary controllers is analysed. An auxiliary dead-band controller (ADC) is proposed and modelled. The ADC is fitted with three supplementary frequency control schemes and their effectiveness is tested on a four terminal HVDC scheme integrated with an OWF. These tests are carried out through MATLAB/Simulink simulations. A small signal stability of the system is also carried out and validated against the time domain simulations.

Chapter 5 – Hardware-in-the-Loop Validation of Auxiliary Dead-band Controller for Fast Frequency Support

The three machine GB power system is modelled in a Real Time Digital Simulator (RTDS) and connected to a physical three terminal VSC-HVDC test rig via a power amplifier. This forms a hardware in the loop (HiL) system, which was used to validate the fast frequency controllers described in Chapter 4.

Chapter 6 – Conclusions

The findings and conclusions of this PhD thesis are discussed in this chapter. Recommendations for future work are also presented.

1.4 List of Publications

1.4.1 Journal Papers

1. **K. F. Jose**, T. Joseph, J. Liang and C.E. Ugalde-Loo, “Auxiliary Dead-Band Controller for the Coordination of Fast Frequency Support from Multi-Terminal HVDC Grids and Offshore Wind Farms,” *IET Renewable Power Generation*, vol. 12, no. 13, pp. 1444-1452, October 2018.

1.4.2 Conference Papers

1. **K. F. Jose**, O. D. Adeuyi, J. Liang and C. E. Ugalde-Loo, "Inertial contribution from large scale variable-speed wind turbines connected to the GB grid," *13th IET International Conference on AC and DC Power Transmission (ACDC 2017)*, Manchester, 2017, pp. 1-6.
2. **K. F. Jose**, O. Adeuyi, J. Liang and C. E. Ugalde-Loo, "Coordination of fast frequency support from multi-terminal HVDC grids," *2018 IEEE International Energy Conference (ENERGYCON)*, Limassol, 2018, pp. 1-6.
3. T. Joseph, **K. Jose**, C. Ugalde-Loo, G. Li and J. Liang, “Real-Time Hardware-in-the-Loop Platform for Power Systems Studies”, 2019 IEEE PES PowerTech Conference, Milan, 2019, pp 1-6.

1.4.3 International Workshops and Presentations

1. K. Jose, “Inertia contribution from large scale VSWTS connected to the GB grid”, 7th HVDC Colloquium, Porto, Portugal, 2016.
2. K. Jose, “Mitigating the effects of low inertia and low short circuit levels in HVDC-rich AC grids”, GE meeting, UK, 2016.
3. K. Jose, “Mitigating the effects of low inertia in HVDC-rich AC grids”, Nigeria Energy Forum, Lagos, Nigeria, 2016.
4. K. Jose, “Fast frequency support from MTDC grids”, Nigeria Energy Forum, Lagos, Nigeria, 2017.

1.5 List of Contributions

The main contributions of this thesis are summarised as follows:

- **Analysis of effect of increased wind penetration on AC grids:** Using the three-machine GB model, the system frequency response from varying converter-based wind generation was studied. Also, the inertial contribution capability of these wind turbines was analysed.
- **Study of fast-frequency control schemes:** Three control schemes for providing frequency support from MTDC schemes were modelled and studied under two conditions i.e. fitting the control scheme in only one converter and fitting the scheme in all converters in the dc grid.
- **Proposal and design of an ADC logic:** The ADC was developed to enable the converters determine what grid is troubled and what grids are responding to this issue without the use of communications. The ADC removed dc voltage instabilities and power oscillations which occurred due to all converters entering frequency sensitive mode.
- **Mathematical modelling:** The mathematical model of a four-terminal MTDC scheme with droop control and supplementary frequency control schemes was developed to determine the effect of the proposed control schemes on the system’s small signal behaviour.
- **Experimental validation of frequency control schemes:** To validate the proposed schemes and ADC, a HiL system made of a three-terminal

VSC system and three-machine GB system was modelled to carry out frequency studies.

Chapter 2

Literature Review

2.1 Introduction

Electric power systems are continuously evolving. Thomas Edison built the first electric power system in 1882 [11]. Although this system was in dc, it was limited to delivering power to only short distances from the generators; therefore ac power systems won the so-called “war of currents” and became more popular [30]. This was thanks to the availability of transformers, ac transmission, polyphase systems and synchronous generators [11], which were developed thanks to Nikola Tesla, L. Gaulard and the Westinghouse Company, among others [31]. These ac systems were simpler and cheaper than their dc counterparts. For instance, there was ease of voltage transformation [30]. However, with changing times, dc transmission is becoming more popular. DC transmission has proven to be more attractive in transmitting vast amounts of power with reduced losses, ease of asynchronous interconnections and economic feasibility [32], [33].

The fuel used for electricity generation was mainly fossil fuel-based sources such as coal, oil and gas, but the world is now moving towards renewable energy sources due to the negative effects which these fossil fuel-based sources have on the climate. A major clean energy source is wind energy, which is abundant offshore but sometimes far from the load centres. With HVDC transmission, wind and other renewable energy sources may form a huge share of countries generation capacities and help achieve the aim of a clean-energy future.

This thesis studies the effects of declining inertia on the GB power system. For an efficient and reliable operation of this changing future power system, the increased penetration of renewable energy transmitted via HVDC needs to be studied in depth. In this chapter, the change in GB generation mix, the state-of-the-art HVDC technology, WT technologies, inertia and frequency response are discussed in detail.

2.2 Power System Changes

To reduce climate change effects due to greenhouse gas emissions and to provide a more sustainable future, the UK agreed to legally binding targets to produce at least 15% and 30% of its total energy consumption (electricity, heating and transport) from renewable energy sources by 2020 and 2030 respectively [34]. Also,

the UK is legally bound by the Climate Change Act 2008 to reduce the greenhouse gas emissions by at least 80% from 1990 levels by 2050 [35], [25].

Coal, gas and other fossil fuel sources are being replaced by renewable energy sources such as wind, solar, biofuels, tidal and hydro energy to meet these targets. Also, with the reduction of emissions, energy demand is also increasing with a growing population. Heat and transport are to be electrified and this will also add to an increased demand for electricity [36] which is expected to be provided by clean sources of energy.

2.2.1 Future Energy Scenarios

The National Grid Future Energy Scenarios 2018 (FES) provides insight on 4 possible pathways the UK may take in achieving its carbon reduction targets. The scenarios depict how the generation mix in the UK may change. They are the steady progression (SP), two degrees (TD), consumer evolution (CE) and community renewables (CR) scenarios. The TD scenario assumes rapid decarbonisation using more centralised technologies such as offshore wind, nuclear, interconnectors and large-scale storage. The SP scenario also works towards decarbonisation with centralised technologies but at a slower rate and does not meet the 2050 target because of lack of available funds to aid faster decarbonisation [35]. The CR and CE scenarios focus on the use of more decentralised technology such as EVs, onshore wind, heat pumps and smart technology. Of these 4 scenarios, TD and CE meet the 2050 targets.

Table 2.1 shows the expected generation capacity change in 2030 and 2050 for the TD and SP scenarios. It can be deduced that although both scenarios are different, generating electricity from coal is recognised to be detrimental to the environment and all 12.7 GW of coal generation will be shut down and replaced by other forms of energy by 2030. Gas generation is still a big part of the generation mix in SP unlike in the TD scenario, where it is reduced to 9.5 GW by 2050. There is also an increase in offshore wind and other renewable energy sources in both scenarios. The TD and SP scenarios are discussed because they focus more on centralised technologies such as offshore wind and HVDC interconnections, which are of focus in this thesis.

Table 2.1: Expected generation capacity by type in 2030 and 2050 [37].

<i>All capacities shown in GW</i>	2017	2030		2050	
		TD	SP	TD	SP
Biomass	3.3	5.9	4.7	3.7	1.8
CCS	0.0	0.9	0.0	12.1	6.7
Coal	12.7	0.0	0.0	0.0	0.0
Gas	34.9	30.7	41.4	9.5	36.2
Hydro	1.8	2.0	2.0	2.1	2.0
Interconnectors	4.0	19.8	15.1	19.8	15.1
Marine	0.0	3.3	0.1	6.1	0.9
Nuclear	9.2	9.0	2.9	18.6	15.2
Onshore wind	11.5	19.5	15.5	22.3	16.4
Offshore wind	6.1	29.9	24.8	43.4	35.0
Other renewables	1.8	2.9	2.1	5.7	2.7
Other thermal	1.5	0.8	1.1	0.2	0.8
Solar	12.4	24.3	16.4	43.7	27.3
Storage	2.9	8.9	5.9	17.3	11.8
Vehicle to Grid	0.0	1.0	0.2	17.9	15.6
Waste	1.3	2.0	1.7	1.9	1.7
Total	103.5	160.9	133.9	224.3	189.1

In summary, in both cases, the generation mix of the UK power system is projected to change and renewable energy sources will play a part in this change, although a lot more in the TD scenario. In the TD scenario, in 2050, wind and solar will form about 30% and 20% of the total generation capacities respectively, compared to 17% and 12% in 2017.

These changes in generation mix may add more complexity and changes to the way the power system is being operated. These renewable sources (wind and solar) are not directly coupled to the grid or do not have moving parts (in the case of solar) and therefore do not contribute to system inertia. A replacement in a large proportion of conventional generators by solar and wind technology would reduce the system inertia, which can lead to frequency instability if their control is not approached appropriately.

2.3 Wind Technology

Presently, wind energy is the most exploited renewable energy source [38]. Due to the wide distribution of the wind resource around the world, there is an increasing growth in the amount of wind power being installed worldwide, with 54.6 GW more wind capacity being added in 2016 [39]. A huge share to this growth was from China, where 23.4 GW of new capacity came online in the year. Europe and North America are the two other big wind markets in the world. Figure 2.1 shows the top wind energy markets in the world with their installation capacities. The total wind capacity at the end of 2016 was 486.6 GW, representing a cumulative market growth of more than 12% from the previous year [39]. Wind Europe (formerly the European Wind Energy Association) believes that wind energy could be the backbone of Europe's future energy system. It is also reported in 2017 that wind accounted for 44% of the new installations across Europe and now covers 11% of Europe's electricity demand [40].

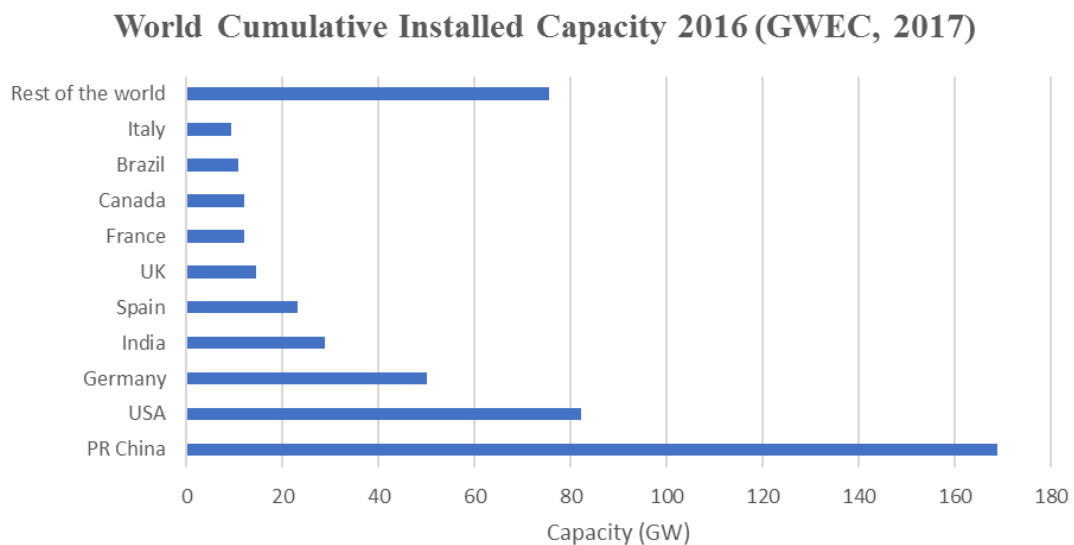


Figure 2.1: Global cumulative installed wind power capacity to 2016 [39].

The advancements being made in WT technology has enabled wind to be a viable and competitive source of energy today [41]. WT technology has grown over the years increasing from capacities of as little as 300 kW in 1989 [12] to present day capacities of 12 MW per turbine as in GE's Haliade-X offshore turbine [42]. The rotor diameters and heights have increased over years to increase potential energy capture and sophisticated power electronics have been added to allow variable

speed operation [41], [43]. WTs are becoming as high as some of the tall landmarks in the world, as shown in Figure 2.2.

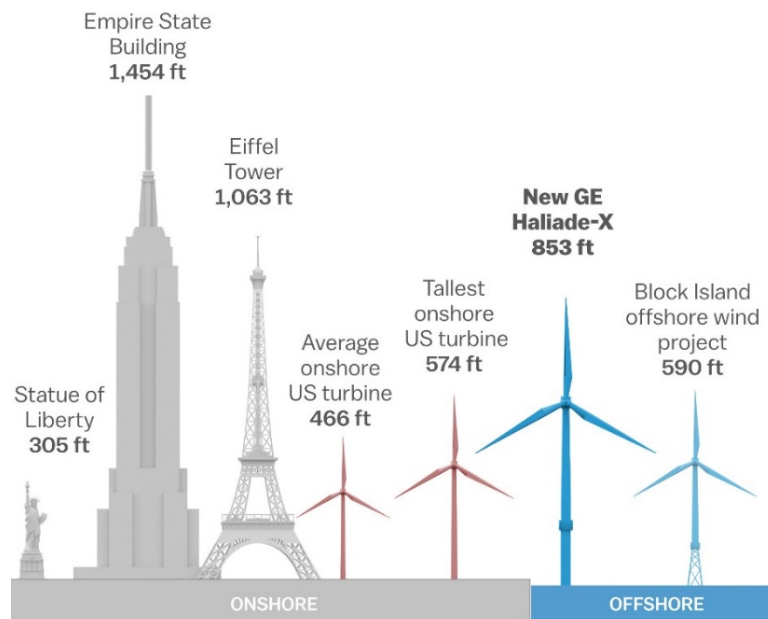


Figure 2.2: Comparison of WT sizes to world landmarks [44].

Offshore and onshore WTs have the same general operation. A WT produces electricity by capturing the energy in the wind. This energy spins its two or three rotor blades. Based on the orientation of the rotor shaft, WTs can be categorised as horizontal axis WTs (HAWTs) and vertical axis WTs (VAWTs). Figure 2.3 shows a general HAWT scheme. The rotor blades are connected to the generator via its shaft and the rotor motion turns the generator shaft to create electricity. Sometimes, the rotor blades are connected to the generator via a gearbox [43]. The gearbox adapts the angular speed of the rotor to the high speed of the generator [12]. However, this configuration has a high failure rate [45] and some WT topologies, such as the direct drive, have been created to remove the gearbox component and operate at lower rotational speeds [12], [46]. The generator converts the rotational energy to electrical energy at 690 V. Depending on the generator there may be power electronics converters connected at the generator terminals. The power output goes to a step-up transformer which increases the voltage to the appropriate collection voltage [43].

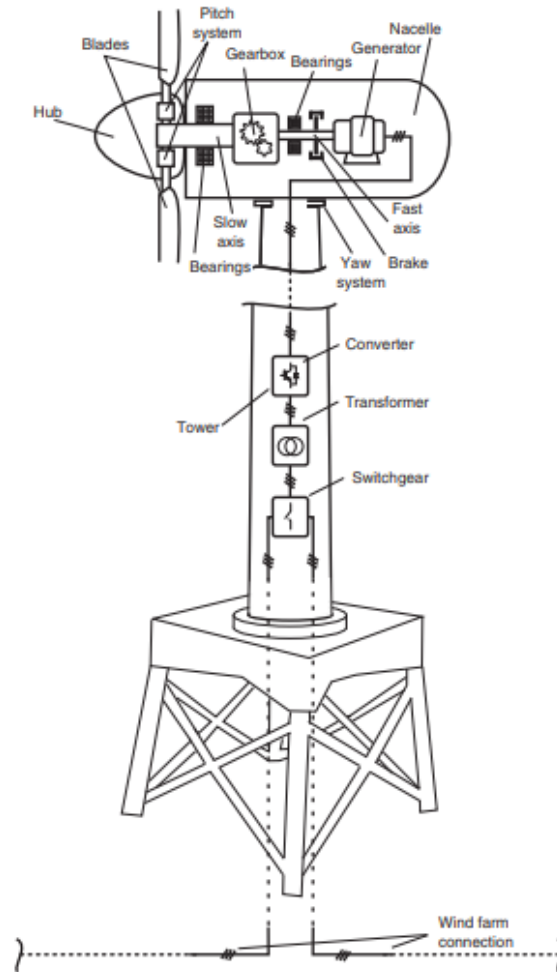


Figure 2.3: Conceptual scheme of a general WT [12].

The power extracted by the WTs is not the same as the power in the airflow. The Betz limit defines the maximum coefficient of power C_p of the WT as 59.3%. This means that a WT cannot capture more than 59.3% of the kinetic energy in the wind [43].

2.3.1 Fixed Speed Wind Turbines

This simple WT topology is mainly used for smaller turbines [12], [47]. It was used by many Danish WT manufacturers in the 1980s and 90s and was commonly known as the Danish concept [12], [48]–[50]. The fixed speed wind turbine (FSWT) operates over and near the grid synchronous speed [43]. Shown in Figure 2.4, the FSIG is made of a multiple-stage gearbox connecting the three-bladed rotor to a squirrel cage induction generator (SCIG), which is directly connected to the grid through a transformer [12], [51]. The FSWT is usually provided with capacitor

banks for reactive power compensation to magnetise the SCIG [12], [48]. If left to take its reactive power directly for the grid, the FSWT draws varying amounts and this can lead to the grid voltage fluctuations [49]. As its power level changes, the slip varies only slightly between 1-2%, maintaining its fixed speed operation [52].

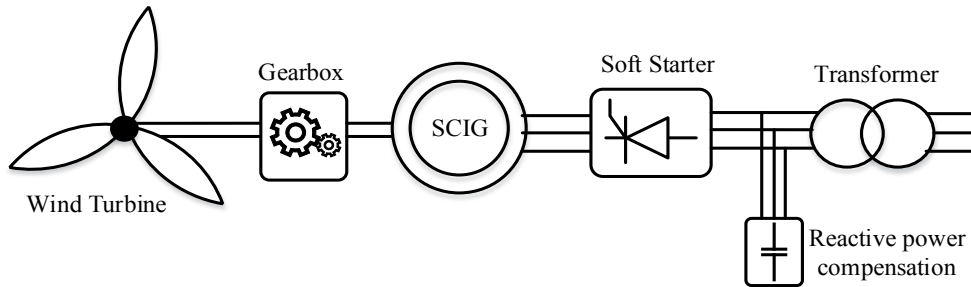


Figure 2.4: FSWT - with SCIG [12]

2.3.2 Limited Variable Speed Wind Turbines with Variable Rotor Resistance

Shown in Figure 2.5, the limited variable speed wind turbine (LVSWT) concept replaced the SCIG of the FSWT with wound rotor induction generator (WRIG) and introduced a variable rotor resistance [12]. The machine slip can be changed by varying the rotor resistance through a converter. Therefore, it allowed for the generator speed operation range to be increased (0 to 10%) [12], [53]. They were commercially called Optislip and were developed by the Danish manufacturer Vestas [12]. This means of allowing for partial variable speed operation requires controlling energy extracted from the WRIG by dissipation of extra power in the external resistor [48]. This topology allowed improved aerodynamic efficiency but lower generator efficiency [12].

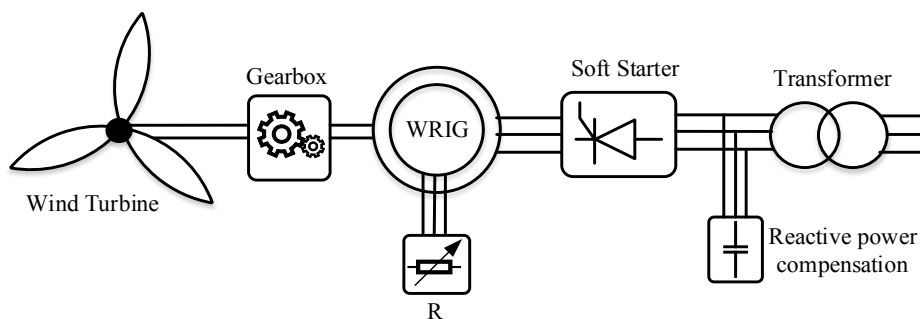


Figure 2.5: LVSWT - with WRIG [12].

2.3.3 Variable Speed Wind Turbines

The VSWTs were developed to increase the speed range of operation. They can operate over a wide range of speeds as the rotational speed of the WT can be adapted to the changing wind speeds, thus allowing maximum power capture. These WTs are also more “grid friendly” because they are easier to control and can thus adhere to grid codes. They are suitable for high power applications like offshore wind farms [54]. The common topologies are the doubly fed induction generator (DFIG)-WT with partial-scale power converter and the direct driven permanent magnet synchronous generator (PMSG)-WT with FPC [12].

2.3.3.1 VSWTs with Partial-Scale Converter

A DFIG-WT configuration is shown in Figure 2.6. It is a VSWT with a WRIG whose stator is connected directly to the grid while its rotor is excited via a partial-scale power converter [49]. The partial-scale power converter decouples the electrical and mechanical frequencies, thus allowing control of the rotor speed for a variable speed operation (0.7 to 1.3 pu) [54]. It also allows for a proper active and reactive power control [12]. Also, the power electronics in this topology allows independent control of the grid side and machine side, thus allowing the WT to meet the grid code requirements with regards to frequency control and fault-ride through capability. The converter rating is usually about 25-30% of the generator rating making it a more economical turbine [48], [54]. However, the use of slip rings in the DFIG-WT to extract power from the rotor is a major drawback, as slip rings are a major cause of failure in the machine [12].

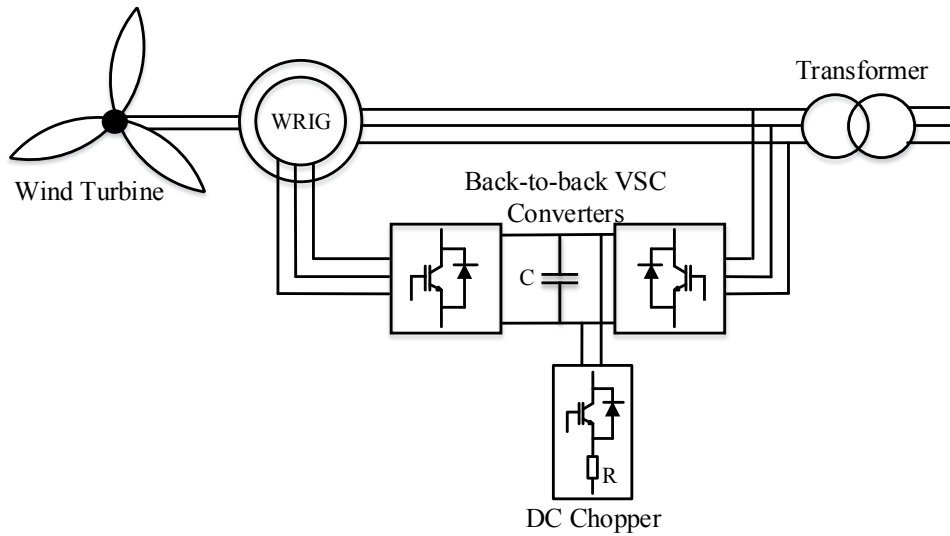


Figure 2.6: VSWT with partial-scale converter or DFIG-WT [12].

2.3.3.2 VSWTs with Full Power Converter

A VSWT topology with FPC is shown in Figure 2.7. It can extract the maximum available power from the wind by utilizing the full speed range of the machine. This configuration can make use of several types of generators such as the SCIG, wound rotor synchronous generator, and PMSG. These WT are direct driven, connected to the grid through the FPC and may come with or without a gearbox. All the power from the machine is passed to the grid through the converter; therefore, the grid frequency is completely isolated from the machine frequency. Like the VSWT with partial-scale converters, the FPC based WT can also provide fault ride through, voltage and frequency support to the grid as required in grid codes. However, they have higher costs because the converter is of the same rating as the electrical machine. They also have more power losses in the power converters because all the power goes through them [48].

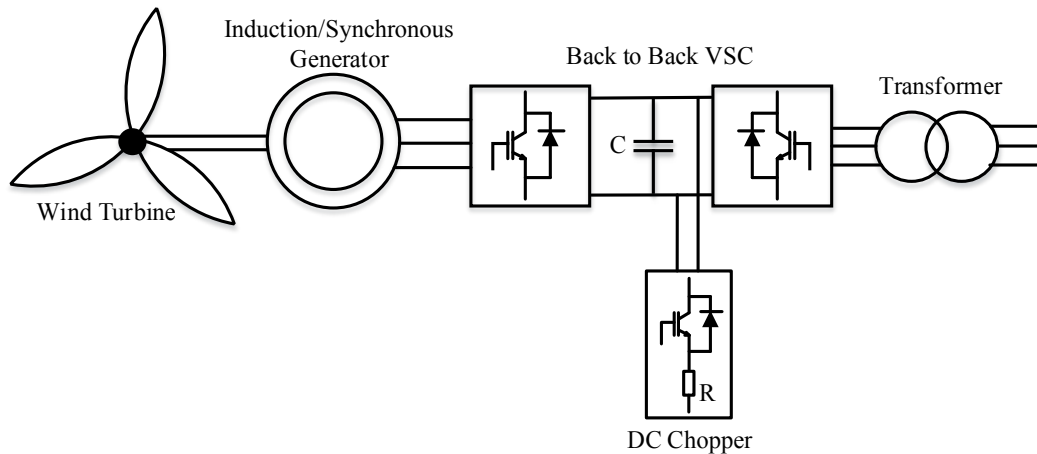


Figure 2.7: VSWT with FPC – can use SCIG, WRSG or PMSG [12].

2.3.4 Summary of WT Topologies

FSWTs are simple and robust in construction; however, they are limited to one speed and cannot provide more power with higher wind speeds [51]. The flexibility of the FSWT was improved on by introducing the LVSWT; however, these have high losses and had limited response to grid code requirements. The DFIG-VSWTs response to grid code requirements is much improved and could also provide much better variable speed operation. However, because these are not completely decoupled from the grid, a proper fault ride through operation is complicated. Also, the WT cannot operate in the full speed range because of the partial scale converter [54]. Presently, DFIG-WTs are dominating the wind energy markets because of their costs, despite their disadvantages. As the cost of permanent magnets and power electronics has reduced considerably in recent years, the PMSG-VSWTs with FPC are expected to take over the wind market [12]. They offer variable speed operation with the possibility to transfer all generated wind power to the grid [48]. Also, they have low maintenance costs, wider operating range and a higher efficiency [47]. Their complete decoupling from the grid and enhanced fault-ride through capability make of them a much preferred option for offshore applications [54].

2.4 High Voltage Direct Current Transmission Systems

High voltage ac (HVAC) transmission has been the backbone in power systems for more than one hundred years [33]. It has been used for bulk power transfer over long distances. It also provided a cost-efficient solution to integrate renewable energy sources [38]. However, it is losing its place to HVDC technology. This is because HVAC transmission systems have higher power losses and higher costs as the transmission length increases. In addition, they need reactive power compensation due to the losses. The break-even distance in which HVDC transmission becomes cheaper than HVAC transmission is 500-800 km for overhead lines and 50 km for submarine cables [31], [32]. Above this break-even distance, HVAC may become less suitable to transfer power from renewable energy sources such as OWFs when they are located very far from the load centres.

Initially, there was no technology to increase or decrease dc voltage levels like the ac transformers. However, in the 1930s, Rene Thury introduced the idea of dc voltage transformation by connecting dc generators in series to achieve the desired voltage. Power could be distributed at the desired voltage level using dc batteries at the terminal station [32]. These series connected dc generators were used from 1882 to 1925. An important example is the 125 kV 20 MW 230 km Moutiers-Lyon interconnection, which was operated from 1906 to 1936 and used eight series connected dc generators [55]–[57].

The continuous development of power electronic technologies has been a dominant factor in the growth of HVDC transmission systems. HVDC systems began to gain popularity for long distance power transmission when mercury valves were developed for its application between the 1920s and 1930s [31], [32], [55]. The first commercial HVDC link was located between the island of Gotland and Swedish mainland, it was started in 1954 [30], [55]. This Gotland 1 HVDC link was 98 km long and carried 20 MW at ± 100 kV. It was later shut down in 1986 [55].

In the 1970s, the availability of thyristors made HVDC transmission more attractive and the mercury-arc valves began to be replaced by them. The 320 MW back-to-back Eel River interconnection scheme between the Canadian provinces of Quebec and New Brunswick was the first to be developed based on this technology

[31]. The Gotland 2 and 3 links with rated voltage 150 kV and transmission capacity of 130 MW are another example of thyristor-based converters. These thyristor-based converters are called line commutated converters (LCC) or current source converters (CSC). Since the 90s, insulated gate bipolar transistors (IGBTs) were developed for use in HVDC transmission. The first system employing IGBT technology was created in 1997 by ABB in a 3 MW, 10 kV demonstrator project with 10 km overhead dc lines in Hällsjön, Sweden [58]. This IGBT-based converter is called the voltage source converter (VSC). There are now more than 100 HVDC transmission systems around the world [30] with voltage ratings as high as ± 1100 kV. The operation of these systems is described next.

2.4.1 Line Commutated Converters

The LCC or CSC technology uses the thyristor valve technology to convert ac to dc power and vice versa [31]. The LCC is a mature technology and the largest LCC-HVDC converter station to date is the Zhundong-Sichuan project in China. It has a 10 GW capacity, a record distance of 2600 km and it also has the highest voltage rating of ± 1100 kV [59]. The LCC converter technology can transfer large amounts of power over long distances with lower losses and lower costs than VSC-HVDC technology [32], [33]. However, it has disadvantages, such as its high risk of commutation failure when ac disturbances occur - especially in the inverter station [12]. LCCs are unable to provide reactive power support and need reactive power compensation instead. This reactive power requirement increases with the increase of transmitted power causing the converter station to occupy a lot of space [60]. LCCs require a strong ac system to commute; therefore, they are not suitable for black start support operation¹. They also have a requirement for large ac and dc harmonic filters. Finally, the direction of power flow can only be changed by reversing the voltage polarity, current reversal is not possible. This operation is complicated and makes it difficult to use in a multi-terminal grid [60].

¹ Black start support is the ability of the converter to restore power to the ac grid it is connected to [12]

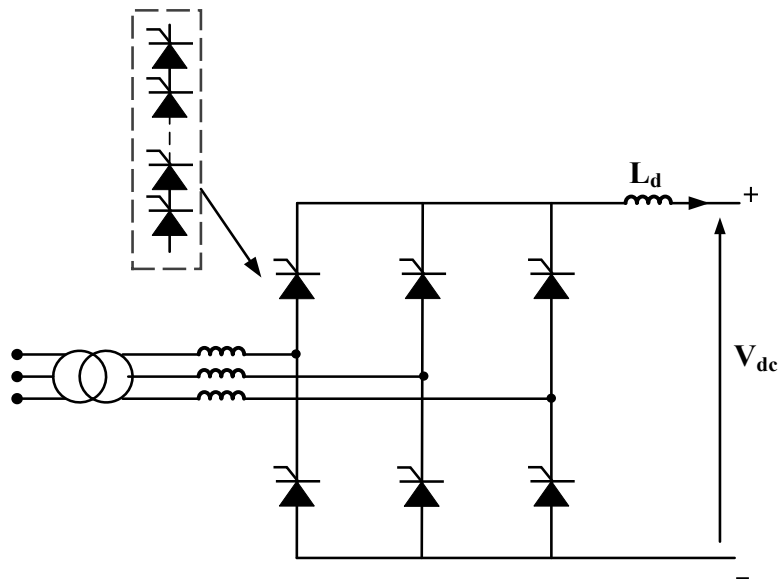


Figure 2.8: Six-pulse LCC with thyristors [58].

Figure 2.8 shows a six-pulse LCC in rectifier mode. Each thyristor valve is made of series connected thyristors to achieve the required dc bus voltage. The inverter or rectifier operation of a converter is determined by the thyristors' firing angle. Thyristors have high voltage ratings; they can block up to 8.5 kV and carry up to 5 kA current [12]. Because of this, they can transfer bulk amounts of power. The inductance L_d at the dc side acts as an energy storage element in the LCCs. It holds the dc current constant forming a current source on the dc side which is why they are called CSCs [55].

2.4.2 Voltage Source Converters

The backbone of the VSC technology is the IGBT - a device which combines the advantages of the metal-oxide semiconductor (MOSFET) and bipolar junction transistor (BJT) [12]. It is fully controllable with its easy turn on and off operation and this allows its power flow regulation to be faster than in the LCC technology [12]. The first commercially available VSC-HVDC was the 50 MW Gotland Scheme in Sweden, using 70 km cables at ± 80 kV [12]. VSCs can control active and reactive power independently at the ac side. VSCs can absorb and generate reactive power, meaning they do not need extensive reactive power compensation like in the LCC-HVDC transmission [60]. Also, in the VSC, current polarity reversal is possible, which makes the technology more viable for underground

power transmission and for MTDC grids, where it is important to keep a constant dc voltage. VSCs do not need to be connected to a strong ac system to start-up and can generate their own ac voltage; therefore, they are suitable to provide black start support. For this reason, they are very suitable to connect to weak grids and wind farms. The requirement for harmonic filtering is reduced in VSCs compared to LCCs [12], [60].

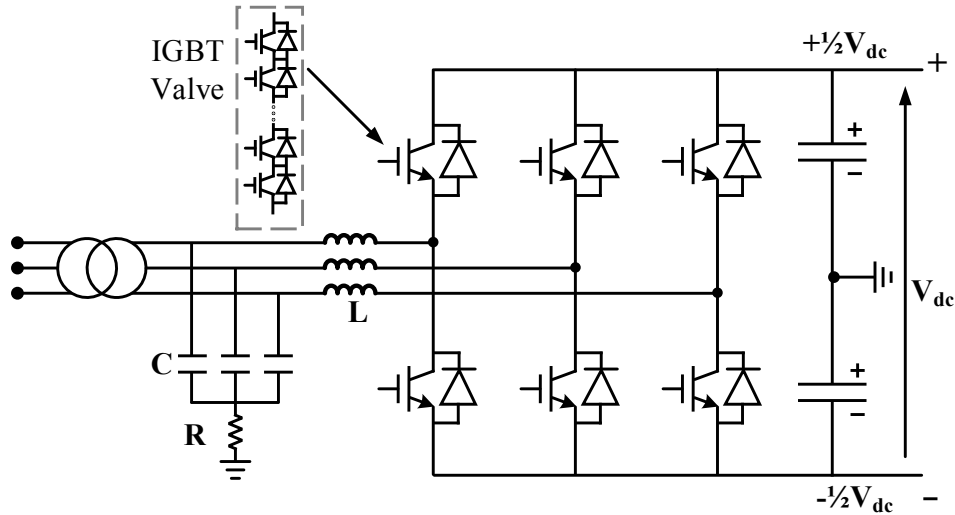


Figure 2.9: Two-level VSC [61].

2.4.2.1 Two-Level Converters

Figure 2.9 shows a two-level VSC which was used in the first-generation models of VSCs. Each valve contains IGBTs with inverse-parallel diodes [59]. This converter uses pulse width modulation (PWM) to generate two levels of dc voltage ($+\frac{1}{2}V_{dc}$ and $-\frac{1}{2}V_{dc}$) from the three phase ac voltages in a rectifier. Similarly in the inverter, the output ac voltages are also created by alternating between $+\frac{1}{2}V_{dc}$ and $-\frac{1}{2}V_{dc}$ [55], [59]. For two-level converters, a high switching frequency is required to obtain a smooth sinusoidal waveform [55], but this means more power losses in the converter from switching. Also, this converter topology has relatively high filtering requirements to smoothen the outputs and reduce harmonics. However, its filter requirement is still much smaller than the LCC-HVDC [60]. A two-level VSC station is around 50% the size of an LCC station [60].

2.4.2.2 Three-Level Converters

Shown in Figure 2.10, the three-level VSC with neutral point clamping (NPC) is the second generation VSC-HVDC [60]. This technology was developed around 2000. They were built with the aim to reduce switching losses in the converters and lower harmonic distortion - thus reducing the number of filters needed [12], [60]. The converter transformers also have a reduced insulation requirement in the three-level NPC due to reduced dV/dt stresses (unlike the two-level VSC) [60].

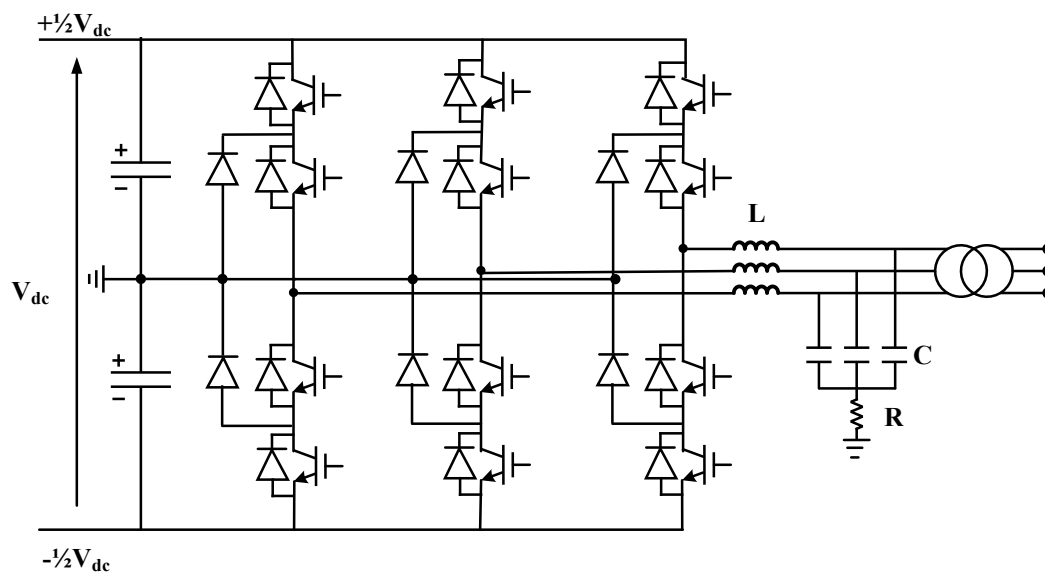


Figure 2.10: Three-level NPC converter [61].

2.4.2.3 Modular Multilevel Converters

Proposed by Marquardt and first implemented in 2010 by Siemens in the 85 km long, 400 MW and ± 200 kV Trans Bay Cable project, this converter concept built on the three-level idea, showing the benefits of having a higher switching level than their two-level predecessors [12], [60], [62]. Modular multilevel converters (MMCs) can synthesise a waveform which is as close to sinusoidal as possible [60]. This is done by having several cells or submodules which are stacked together to build a single valve. Each submodule consists of the IGBT switches, parallel diodes and its own separate capacitor [12]. The submodules can be full-bridge or half-bridge [12], [63] as shown in Figure 2.11. One submodule per arm is switched at a time, which

results in voltage increments at each switching instant and thus building the ac waveform [60].

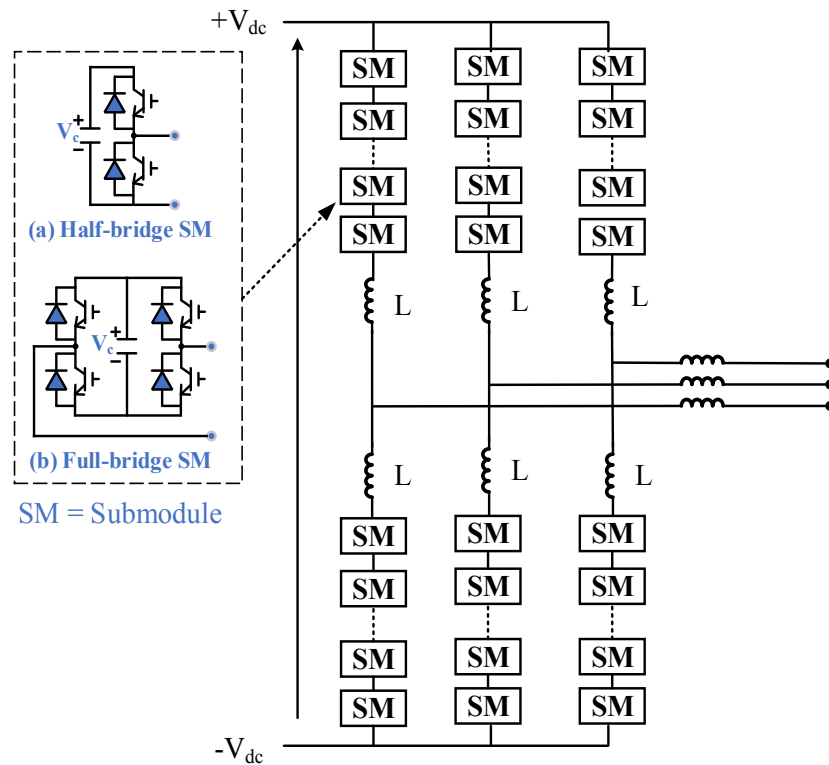


Figure 2.11: Schematic of an MMC [61].

Because the MMC uses several submodules to create smaller voltage steps, the switching frequency is lower, resulting in lower frequency losses. Also, there is reduced voltage stress on the insulation of the converter transformers because of a lower dV/dt thanks to lower voltage steps [60]. Furthermore, there are lower harmonics produced and thus a reduced need for filters than in the two and three-level VSCs. The nature of this type of converter makes it easier to manufacture and maintain [12]. The MMC is better than the NPC three-level converter during faults and unbalanced operation and has a reduced risk of failure/collapse, making it more suitable to follow strict grid codes [60]. The world's first ever 800 kV MMC was recently developed by Chinese power equipment suppliers – Tebian Electric Apparatus (TBEA). With this increased voltage level, MMC capacity can be as high as 5000 MW [64].

Over the years, several VSC-HVDC projects have been commissioned for different applications such as integrating renewable energy, interconnections,

embedded dc lines and asynchronous connections. A list of key VSC-HVDC projects (in construction and commissioned) are provided in Table 2.2.

Table 2.2: Key VSC-HVDC projects (commissioned and in planning).

Project	Location	DC Voltage (kV)	Converter Type	Power (MW)	Length (km)	Year Commissioned
Hallsjon, Sweden [65]	Sweden	±10	2 level	50	10	1997
Murray Link [65]	Australia	±150	3 level NPC	220	180	2002
Trans-Bay Cable [65]	USA	±200	MMC	400	85	2010
East-West Link [66]	Ireland-UK	±200	2-level	500	261	2012
Inelfe [55]	France-Spain	±320	MMC	2*1000	60	2013
Nan'ao Multiterminal (MTDC) [67]	China	±160	MMC	200	9.3	2013
Skagerrak 4 [65], [68]	Denmark-Norway	500	2-level	700	244	2014
Zhousan Multiterminal (MTDC) [67]	China	±200	MMC	1000	141	2014
BorWin 3	Germany	±320	MMC	900	160	2019
Nemo project [69]	Belgium-UK	400	MMC	1000	140	2019

2.5 Frequency Regulation in Power Systems

A power system operator's main duties are to ensure customers are always supplied with electricity and to ensure a balance between demand and supply. Following a frequency event such as a loss of generation, National Grid requires that a set of actions are followed to return the system frequency to 50 Hz as soon as possible [18], [70]. Frequency response providers increase or decrease their output as requested to reduce the power imbalance. This is called frequency containment/management. The Security and Quality of Supply Standard (SQSS) sets out methodologies for operating and planning the GB transmission system [71]. It states that the system frequency of the GB grid must not exceed 50 Hz by more than ±1% (±0.5 Hz) under normal operating conditions [72]. Also, the National

Grid sets its own limits to $\pm 0.4\%$ (± 0.2 Hz) of the nominal frequency. These limits are achieved by setting the governor droop of some connected frequency sensitive generators between 3-5% [73], [74]. This requirement is classified as a continuous service. Additional limits set by the grid code and SQSS also requires that when there is a generation loss up to 1800 MW, the minimum allowable frequency has to be limited to 49.2 Hz with the frequency restored to 49.5 Hz within 1 minute [75]. This response is referred to as occasional service and is usually provided by both generation increase and load reduction in the power system.

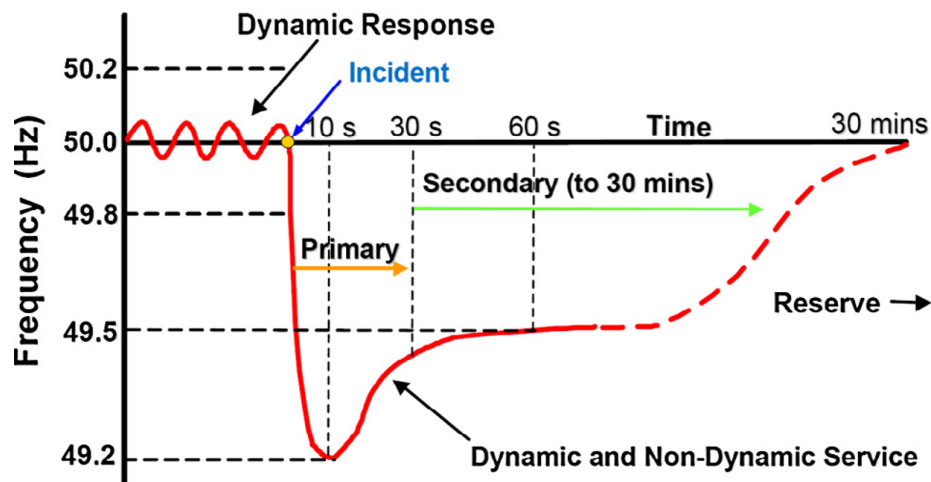


Figure 2.12: System frequency control [76].

National Grid defines 2 categories of frequency response as the dynamic and non-dynamic frequency response. The dynamic response is the continuously provided service which ensures that second by second changes on the system are managed. The non-dynamic response or occasional service is a discrete service that will be triggered at a defined frequency deviation [77].

These frequency response services provided by the National Grid are classified in the next subsection.

2.5.1 Mandatory Frequency Response

This is defined as an automatic change in active power output in response to a frequency change and it is a mandatory service for all connected large generators (≥ 100 MW) to provide. These generators which include large synchronous generators, HVDC converters, onshore and offshore power park modules can provide one or a combination of the following services:

- Primary Response: which is provided within 10 seconds of an event and can be sustained for a further 20 seconds. These are also called frequency containment reserves.
- Secondary Response: which is provided within 30 seconds of the event and can be sustained for a further 30 minutes. The generators are also called frequency restoration reserves.
- High Frequency Response: reduction of active power within 10 seconds of a high frequency event and can be sustained indefinitely.

2.5.2 Enhanced Frequency Response

The Enhanced Frequency Response (EFR) is a dynamic service where the active power is changed proportionally in response to system frequency. The service is aimed at improving the system frequency management before a fault occurs and maintaining it closer to 50 Hz. The service providers must be capable of responding within 1 second of frequency deviation and operate in a frequency sensitive mode [78]. National Grid procured 200 MW of EFR through a tendering exercise in July 2016, with most providers being battery energy storages which can reach their full output within one second. EFR is expected to deliver its response for 15 minutes [18]. Figure 2.13 shows the design of EFR by National Grid. It is expected that it works with primary and secondary response.

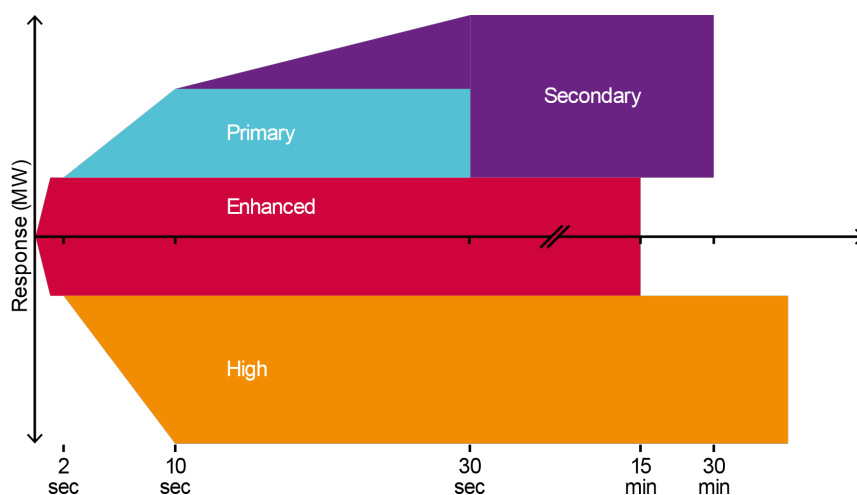


Figure 2.13: Frequency response services [18].

2.6 Inertia

The property of the conventional synchronous generators which makes them inherently responsive to changes in system frequency is called inertia [17], [79]. Inertia is a property of an object which resists change to its original state of motion. In power systems comprising of synchronous generators or motors, the inertia determines how much the frequency drops after a disturbance. The moment of inertia, J (unit kgm^2), is a measure of the strength of the system when there are transient changes in frequency and it is proportional to the kinetic energy stored within the rotating shafts of generators and motors directly connected to the power system [80]. The kinetic or rotational energy is defined as:

$$E_{kin} = \frac{1}{2}J\omega_{0m}^2 \quad (2.1)$$

where ω_{0m} is the base rotational speed of the electrical machine in rad/s.

The inertia constant H (unit s or MWs/MVA) is defined as the ratio of kinetic energy in Watt-seconds at rated speed to the VA base of the machine [31]. After an imbalance, the inertia constant is also significant to the amount of time the generator can continue to provide its rated power relying solely on its kinetic energy [17], [81]. The inertia constant can be expressed as:

$$H = \frac{E_{kin}}{VA_{base}} = \frac{1}{2} \frac{J\omega_{0m}^2}{VA_{base}} \quad (2.2)$$

Rearranging expression (2.2) gives

$$J = \frac{2H}{\omega_{0m}^2} VA_{base} \quad (2.3)$$

When there is an imbalance between the electrical and mechanical torques acting on the rotor of a generator, there is either an acceleration (or deceleration) torque, T_a . The machine's equation of motion describes this acceleration as:

$$T_a = J \frac{d\omega_m}{dt} = T_m - T_e \quad (2.4)$$

where ω_m is the angular velocity of the rotor (unit rad/s), t is time (unit s), T_m is the mechanical torque and T_e is the electrical torque of the generator. Substituting J in expression (2.4) yields,

$$T_a = \frac{2H}{\omega_{0m}^2} VA_{base} \frac{d\omega_m}{dt} = T_m - T_e \quad (2.5)$$

Rearranging expression (2.5), we obtain:

$$2H \frac{d}{dt} \left(\frac{\omega_m}{\omega_{0m}} \right) = \frac{T_m - T_e}{VA_{base}/\omega_{0m}} \quad (2.6)$$

Equation (2.6) can be converted to per unit by using $T_{base} = VA_{base}/\omega_{0m}$

This gives:

$$\bar{T}_a = 2H \frac{d\bar{\omega}_r}{dt} = \bar{T}_m - \bar{T}_e \quad (2.7)$$

where $\bar{\omega}_r$ is the rotor velocity in per unit and all items with overbars indicate they are in per unit. Equation (2.7) is the classical swing equation of a machine. The swing equation can be rearranged as shown below:

$$\frac{d\bar{\omega}_r}{dt} = \frac{\bar{T}_m - \bar{T}_e}{2H} \quad (2.8)$$

The derivative term, $d\bar{\omega}_r/dt$ represents the *RoCoF*. It is observed that the *RoCoF* is inversely proportional to the inertia constant, H . This indicates that the higher the value of H is, the lower the *RoCoF* and the slower the machine is to changing dynamics, making it easier to regulate. The dampers on a car suspension can be seen as an analogy to the system inertia [82].

Since frequency is a global parameter, the power system inertia can also be represented by an equivalent value:

$$H_{system} = H_{machine} \times \frac{S_{bmachine}}{S_{bsystem}} \quad (2.9)$$

$$H_{equivalent} = H_{m1} \times \frac{S_{bm1}}{S_b} + H_{m2} \times \frac{S_{bm2}}{S_b} + \dots + H_{mn} \times \frac{S_{bmn}}{S_b} \quad (2.10)$$

WTs connected via power converters do not inherently contribute to system inertia because their frequency is decoupled from the grid frequency. With an $x\%$ of penetration from WTs, the new power system inertia is calculated as:

$$H_{system,new} = (1 - x)H_{system} \quad (2.11)$$

Equation (2.11) shows that with an $x\%$ penetration from WTs, the total power system inertia will reduce by the same percentage. This inertia reduction can lead to a higher *RoCoF* during a frequency event. Having a higher *RoCoF* because of the reduced power system inertia constant poses several risks. During a frequency event such as loss of generation, a power system with low inertia can face the risk of loss of mains protection relays if it uses *RoCoF* relays. These relays on detecting a threshold *RoCoF* can disconnect some installed distributed generation and the power being supplied to the power system will reduce further, causing a deeper decline in the system frequency [81]. Table 2.3 shows the inertia constants for various machines.

Table 2.3: Inertia constant of different machines [24], [31], [83].

Machine	Inertia, H(s)
Thermal generating unit	2 to 10
Hydraulic Unit	2 to 4
Synchronous motor	2
Synchronous condenser	1-1.25

National Grid has identified the following system needs to mitigate the effects of reduced inertia and *RoCoF*. These are:

1. Taking actions to increase the system inertia would reduce the *RoCoF* but this option is less economic than reducing the largest credible loss.

Adding 3 GW of synchronous generation to increase inertia will have approximately the same effect on RoCoF as reducing the largest loss by 100 MW [18], [84].

2. Desensitizing *RoCoF* relays will allow operation at lower levels of inertia [84]. The current *RoCoF* setting of loss of mains protection devices is 0.125 Hz/s for generators rated above 5 MW [85]. This was based on a power system which had a high minimum inertia. In anticipation of the decline in inertia, National Grid has plans to increase this limit to 0.5 Hz/s for synchronous generators and 1 Hz/s for non-synchronous generators [85].
3. Introduction of new frequency response products. Faster acting frequency response products will help to reduce the *RoCoF*, but National Grid still believes that some inertia will still be required to hold the frequency long enough to allow the very fast frequency response to trigger [84].
4. Synchronous compensators which can provide benefits of adding inertia to the system without generating active power [84].

2.7 Grid Code Requirements on WTs and HVDC for Frequency Support

As it is important to maintain frequency stability, WTs and other renewable sources may have to take up more tasks, which conventional power plants have provided. As more wind power plants (WPPs) are integrated into the power system, system operators are putting in place stringent requirements to allow for frequency support from them and from HVDC transmission systems. For example, Irish regulators have found in studies that with a penetration of 60-70% of total generated capacity from wind, their system frequency stability may be compromised and now require WPPs to provide power reserves [86]. All onshore and offshore WPPs and dc converters in the UK, with registered capacity above 50 MW, must have the capability of participating in frequency control at all times. There are 2 modes of operation which they must adhere to, these are frequency sensitive mode (FSM) and limited frequency sensitive mode (LFSM) [87].

2.7.1 Limited Frequency Sensitive Mode

In the LFSM, the WPPs and dc converters must be capable of maintaining constant active power for system frequency changes between the range of 49.5 to 50.5 Hz. The active power output of the WPPs has to be independent of the system frequency in this range. Also, below 49.5 Hz to 47 Hz, the active power drop in the WPPs must not exceed 5%. This applies to all WPPs with a rated capacity both less and greater than 50 MW. DC converters with power input from National Grid (i.e. exporting power to dc grid) must maintain constant active power between 49.5 to 50.5 Hz and their active power input must not drop below 40% for frequency drops below 49.5 Hz [86], [87]. This control mode is shown in Figure 2.14.

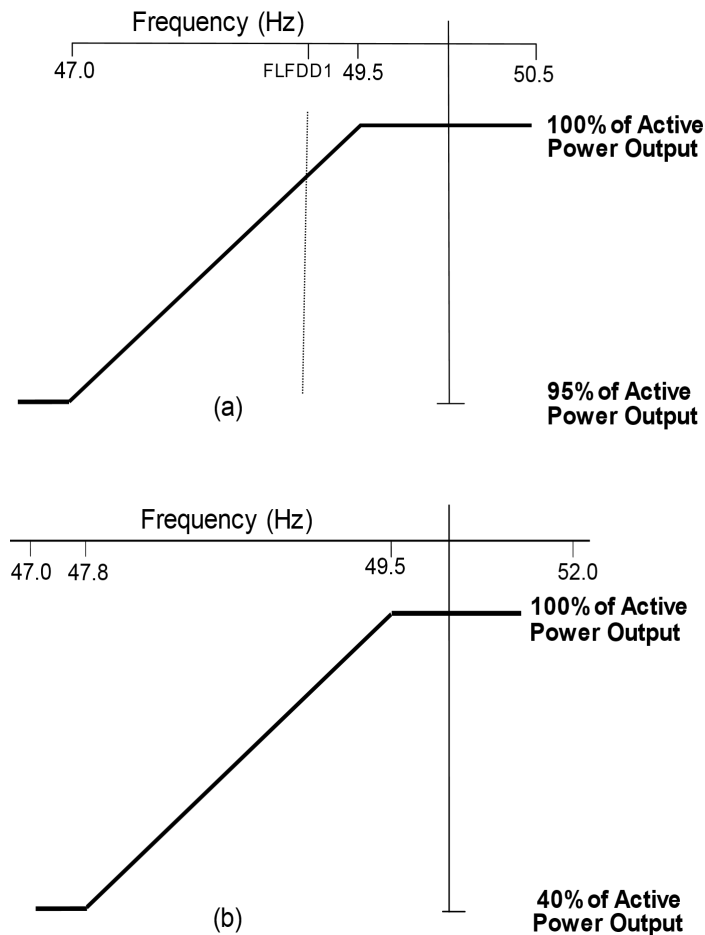


Figure 2.14: Operation in limited frequency sensitive mode. Requirements from (a) generating units and WPPs, (b) dc Converters [87].

2.7.2 Frequency Sensitive Mode

The WPPs, generating units or dc converter stations participating in the FSM are considered to be providing a system ancillary service. WPPs with a registered capacity greater than 50 MW can participate in this service and are no longer required to operate in LFSM [86]. In FSM, WPPs provide primary response, secondary response and/or high frequency response as previously described in Section 2.5.1.

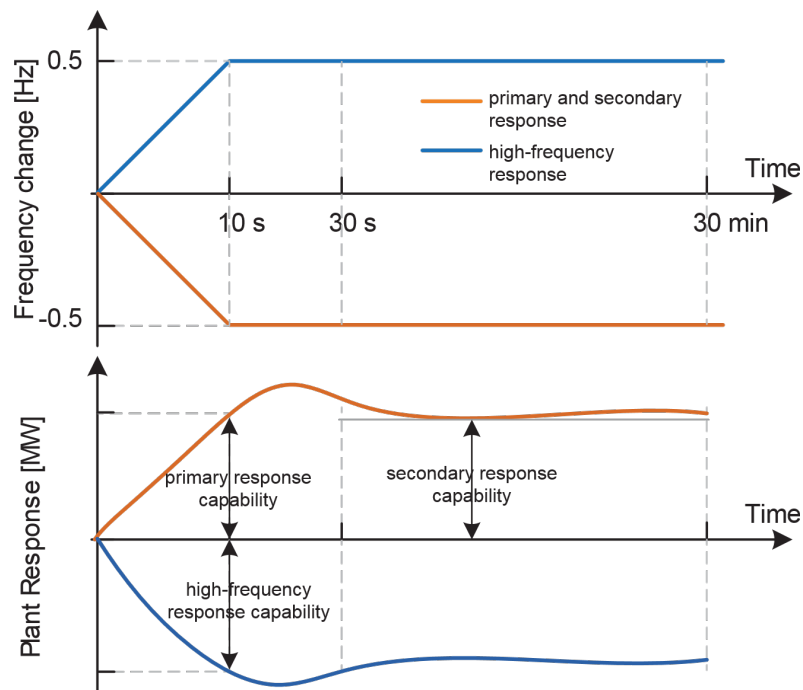


Figure 2.15: Interpretation of primary, secondary and high frequency response [86].

The minimum frequency response requirement is shown for a 0.5 Hz change in frequency. They must provide frequency response at least to the solid boundaries shown in Figure 2.16. This shows that for a ± 0.5 Hz change in frequency, the generators can provide a $\pm 10\%$ active power change.

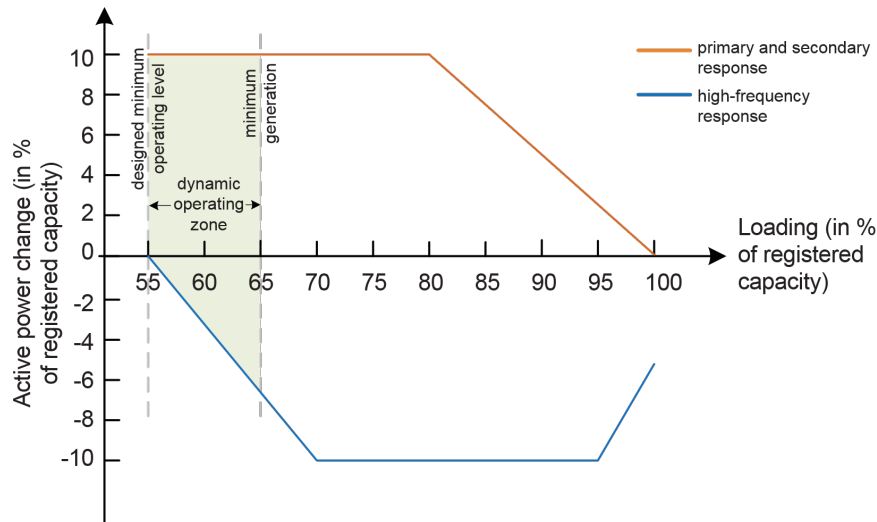


Figure 2.16: UK Grid Code - Minimum active power change for primary, secondary and high frequency response for WPPs in the event of a system frequency deviation of 0.5 Hz [86].

As seen in Figure 2.16, if the WPP is fully loaded (i.e. 100% of registered capacity) it cannot provide an active power change and therefore cannot provide frequency response. Therefore, WPPs in the UK (and also in Ireland) are currently required to operate derated so that they can ramp up their power output by at least 10% of their registered capacity if they choose to participate in FSM [86]. The grid code also highlights two limits: the minimum generation level (MGL) and the designed minimum operating level (DMOL). At the MGL, the WPP and/or dc converter is required to provide high and low frequency response. When the frequency is high, the active power is expected to fall below the MGL but not below the DMOL. The DMOL is the output at which the WPP and/or dc converter does not provide high frequency response. At this point, the WPP is not obliged to reduce its power output unless the frequency is at or above 50.5 Hz. The dead band of frequency control devices in the FSM must be ± 0.015 Hz at most [87].

2.8 Inertia Response from WTs

When suitable control schemes are included, WTs can be made to provide inertia response to the power system. The inertial service WTs provide is sometimes called synthetic inertia (SI), inertia emulation (IE) or inertial response (IR) [88]–[90]. The terms “synthetic” and “emulation” are used because inertia is not a natural behaviour of WTs since their frequency is decoupled from the grid’s frequency.

The SI controller allows the extraction of stored kinetic energy from the WT blades and rotor to capture more energy from the wind. Several control strategies have been proposed for inertia response from WTs. The WTs can either be operating at their maximum power point (MPP) or be de-loaded i.e. maintain some power reserve which they can release for inertial or primary response. This can be done by making the WTs operate at a reduced rotor speed, increased pitch angle or by combining both [91], [92]. De-loading WTs strictly for inertial support is uneconomical as the WTs are not operating at their MPP [81], [91].

In MPP operation, different control methods have been proposed with the controllers fitted to the rotor-side converter of the VSWTs. These controllers can be torque-based, power-based or rotor-speed based [21], [89], [91]. The most common approach is the WT deceleration. Following a frequency drop, the controllers force a change in the WT active power output by slowing down the rotor of the turbine and extracting the available kinetic energy in it [88], [89], [92]. The energy released in this topology can be proportional to the frequency deviation or the *RoCoF* or it can be a predetermined value. Based on this, two proposed controls are discussed here [89], [92], [93]. These are (i) SI or IE and (ii) temporary overproduction (TO) or fast power reserve.

2.8.1 Synthetic Inertia or Inertia Emulation

The SI method forces the rotor speed to follow the *RoCoF* of the ac grid when there is an imbalance, therefore, emulating the behaviour of a synchronous generator. This method takes real time measurements of the *RoCoF* and releases kinetic energy proportional to it. This method scheme is shown in Figure 2.17. Since it uses a derivative control, it is sensitive to noise and can also cause stability problems [89].

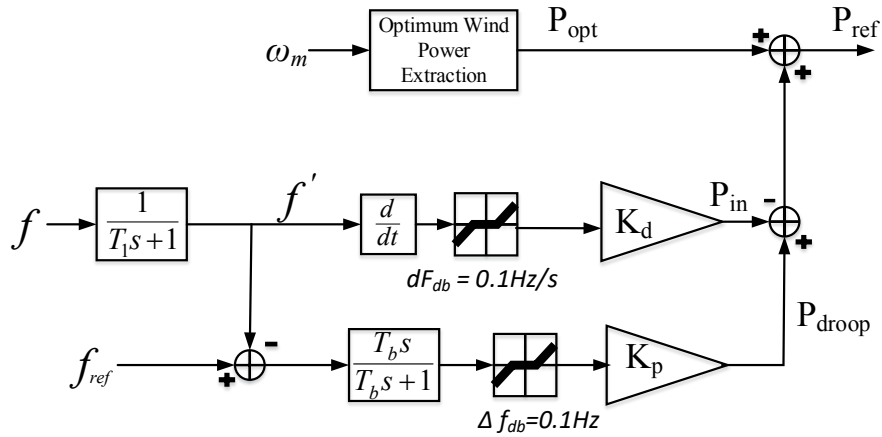


Figure 2.17: Synthetic inertia or inertia emulation scheme.

During normal operation, the reference power P_{ref} is determined by the optimum wind power extraction control (i.e. $P_{ref} = P_{opt}$). When a power imbalance occurs, extra power is provided by the synthetic inertial response P_{in} and sometimes a droop response P_{droop} as shown in Figure 2.17. P_{in} is calculated by taking a derivative of the filtered grid frequency (f') and calculated as:

$$P_{in} = K_d * 2\pi f * \frac{df'}{dt} \quad (3.1)$$

The grid frequency is filtered to reduce noise in the measurements which can affect the differentiation and lead to variations in the output P_{in} , thereby causing instabilities in the drive-train of the WT [23], [89]. The additional P_{droop} can be added to help further limit frequency deviation and to also delay the rotor acceleration period, thus, delaying the start of the recovery phase [94].

2.8.2 Temporary Overproduction or Fast Power Reserve

In this method, an additional power/torque is provided for a short period of time. Unlike the SI method, the amount of power provided in the TO method is not dependent on the $RoCoF$ and it does not emulate a directly-connected synchronous generator [23], [95]. It can either be a predetermined value [93], [96] or proportional to the Δf , with a maximum injection equal to the predetermined value [96]. A general TO control scheme is shown in Figure 2.18. In this chapter, the TO method is selected to provide inertial support as it avoids the derivative terms which

introduces noise in measurements and introduce transient torques, which are harmful for the WT drive-train [97]. In the TO method, a constant step increase in torque is applied for a predefined amount of time when a frequency deviation occurs [98]. Its response is much faster and stronger than the SI method because it does not depend on the real-time frequency variations [24], [89]. Comparing the two major VSWTs, due to the presence of a FPC, the PMSG-WT is capable of providing a higher power due to its higher overloading capability than a DFIG-WT of the same power rating and inertia constant [89].

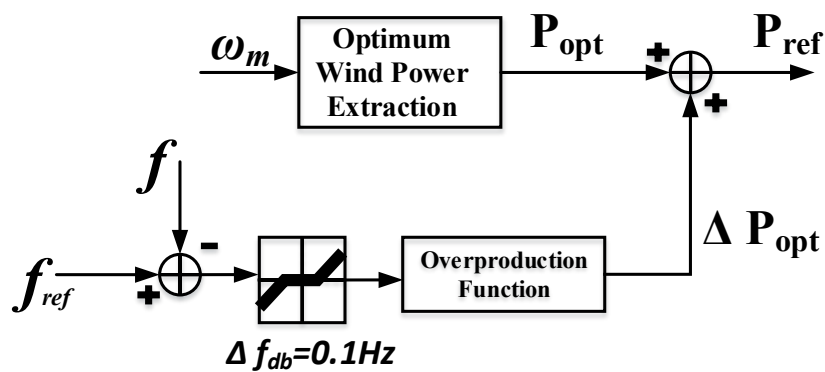


Figure 2.18: Temporary overproduction scheme.

2.8.3 Recovery Phase

The recovery phase is the period in which the SI or TO of power is removed and the WT begins to accelerate back to its pre-disturbance operating point. The overproduction/fast reserve release period is always followed by an underproduction or recovery phase, as shown in Figure 2. 19. The recovery period can cause an extra frequency deviation, with a nadir which could be even more than when no frequency control is used. This can also be worse when there is a high penetration of wind, or at higher wind speeds.

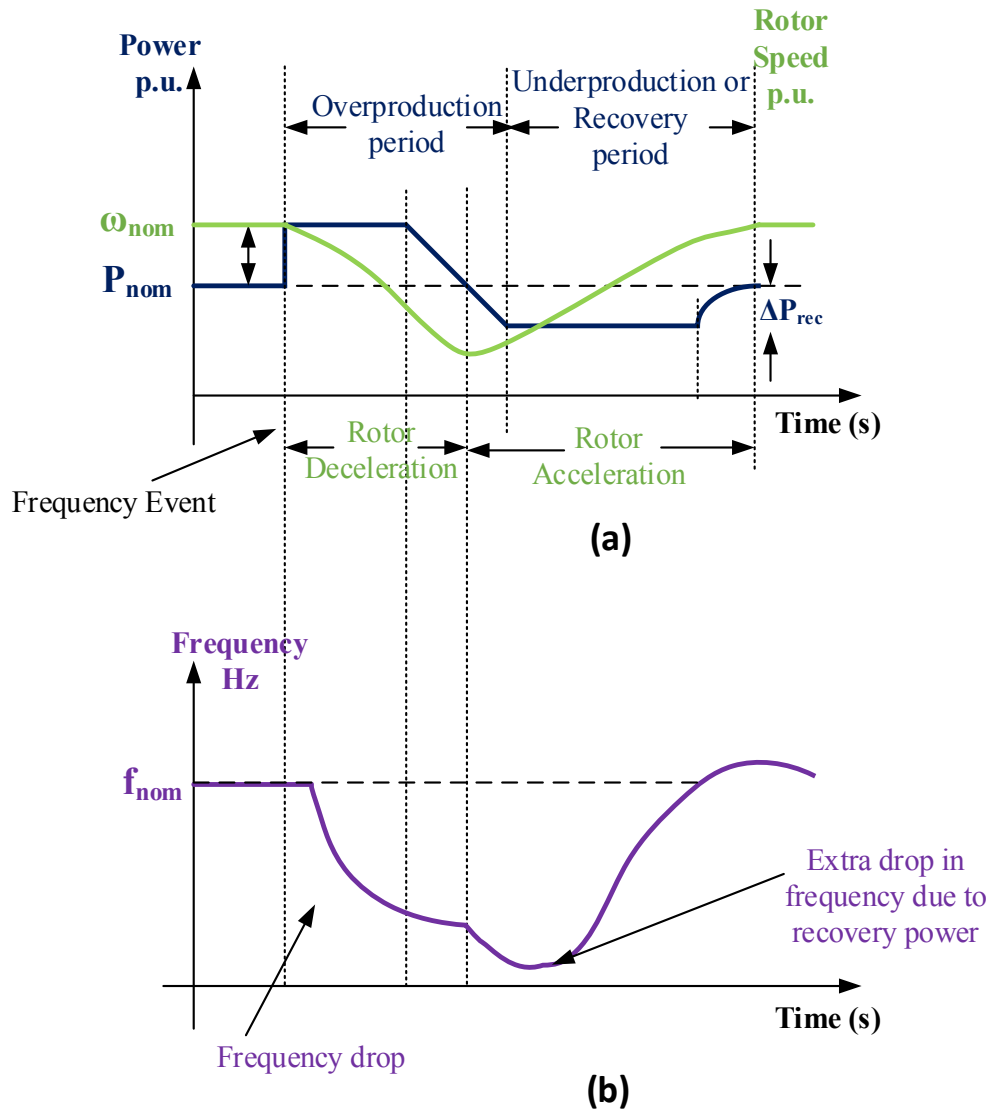


Figure 2. 19: Description of inertia emulation by temporary overproduction and recovery period. (a) WT rotor speed (green) and WT power (blue); and (b) System Frequency.

2.9 Inertia Response from HVDC

When WPPs are connected to the grid via HVAC transmission, they can receive directly the frequency measurements and use the mentioned SI control systems to provide support. However when they are connected by HVDC transmission, they are decoupled again from the grid [99]. There are supplementary controllers for HVDC which either extracts stored energy in the dc link capacitor [90], from connected offshore WPP [88], [100], [101] or from other onshore grids [28]. To

provide frequency support, HVDC transmission systems can have communication-based or communication-free controls. Communication-based frequency support control uses communication channels such as optical fibre and SCADA [101]–[103] to transmit frequency measurements between the different converter stations in the dc grid [29], [101]. Communications-free control schemes which use local signals, such as dc voltage, to reflect the changes in the ac grid frequency at the OWF have been developed [27], [28], [104], [105]. With these methods, response times during frequency support are minimised and potential issues arising from long distance transmission are eliminated [106]. In addition, the need for a large investment in communication links is removed, together with risks associated to communication delays and signal interruptions [107]. Moreover, it has been shown in [101] that communication-free schemes can achieve a quite similar frequency support performance as communication-based methods. In MTDC grids, without OWFs providing extra power to the grids, the different converter stations can provide additional support when needed via droop control and via the exchange of frequency containment reserves between countries [27], [103], [108].

Several fast frequency control schemes have been proposed in literature. The main schemes are based on proportional droop controllers: f - P droop, f - V_{dc} droop and dual loop (which combines f - V_{dc} - P characteristics) [26]–[28]. A derivative-based supplementary control scheme has been proposed which produces extra power proportional to the $RoCoF$. However, this method does not provide as much support as the proportional droop control methods because it deals with a lot of noise due to the derivative block which creates the need for the output to be filtered thus creating less response [127], [137].

National Grid places emphasis on the difference between fast active power injection (sometimes referred to as SI) and system inertia in their System Operability Framework 2016 [18]. They define system inertia as previously done in Section 2.6 but fast active power injection (or fast power reserve) or SI (or IE) is defined as the transfer of power from a system, which does not naturally contribute to system inertia but is able to do so, using controls and measurements.

The primary response requirements have been clearly discussed in the grid codes of the GB and several other countries. Also, as system inertia is a natural response, grid codes do not make emphasis on it. However, inertia response from WPPs has not been included in the grid code requirements of GB but several studies have been carried out by the National Grid to test its possible deployment and how much of it will be required [84]. SI has been studied by National Grid in partnership with Orsted and Siemens in the enhanced frequency control capability project. Trials have been carried out on WTs and the capability of a WPP to provide SI has been examined. Their results have shown the possibility of achieving reduced frequency deviations with SI from WPPs. Moreover, they have shown that no additional investments will be needed to use the capabilities of WTs to contribute to inertia. The issues of recovery period and recovery power are recognised and the need to mitigate or reduce recovery power is emphasised.

Other transmission system operators have also required WTs provide inertial response with the aim of allowing an efficient and economic use of WTs in their grids. Hydro-Quebec have been the first to add SI requirements to their grid codes. Also, in Ireland, where the goal of 75% wind penetration level by 2020 has been set, the TSOs EirGrid and SONI have identified the need to add more inertia to the power system. They have included this as an ancillary service called fast frequency response (FFR), which is similar to the SI in Quebec, although it does not specify a minimum power contribution. In Brazil, the TSO (Operador Nacional do Sistema Electrico) included SI requirements in their last two electricity auctions and expected to also add these requirements to their grid codes [25].

Table 2.4: Inertia response requirements from different TSOs [25].

Criterion	Requirements		
	IESO	HQ	Ireland
Minimum duration	10	9	8
Least Power Contribution	10% pre-disturbance	6% nominal	---
Frequency Threshold	-0.3 Hz	-0.3 to -1 Hz	---
Maximum response delay (s)	0.5	1.5	2
Minimum output for availability	25% nominal	25% nominal	--
Maximum Subsequent power drop below pre-disturbance	5% pre-disturbance	20% nominal	---
Maximum time between two consecutive activations	---	2 min	---

2.10 Summary

This chapter discussed the expected future changes in power systems due to the increasing penetration of renewable energy sources such as offshore wind in response to climate change and the renewable energy directive made in 2009 by the European Union. The state-of-the-art on wind technology and HVDC transmission were also discussed. The advantages of VSC-HVDC over LCC-HVDC and HVAC, such as independent control of reactive and active power, less reactive power compensation, power reversal and ease in integrating offshore wind power were also presented.

Frequency regulation in the GB power system, which includes mandatory and enhanced frequency response services, are discussed. The grid code requirements from WTs and HVDC for primary frequency support were introduced. Inertia and its impact on frequency deviation and *RoCoF* was discussed. The reducing system inertia will lead to an increasing *RoCoF* and this will affect protection systems and relays. Inertial and primary frequency response from WTs and HVDC systems was discussed.

As it is well known that WTs will constitute a major source of the GB generation mix, inertia support requirements from them must be defined by the National Grid. This will be discussed in Chapter 3 alongside the inertia contribution from large-scale VSWTs connected to the GB grid. Gaps identified such as recovery power in WTs and coordination of frequency support from multiterminal HVDC schemes, are also discussed and tackled in the next chapters.

Chapter 3

Inertial Contribution from Large Scale VSWTs

3.1 Introduction

In the future GB system, interconnections and renewable energy especially from wind will replace fossil fuel generation. As described in the previous chapter, VSWTs are more suitable for offshore applications because of their ability to capture more wind at variable speeds and to comply with grid code requirements.

Unlike FSWTs, VSWTs utilise power electronic converters and the electrical machine's rotor speed is decoupled from the network frequency [74], [109]; therefore, they do not contribute to system inertia. If FSWTs formed a major part of the future GB system's wind contribution, there would not be a significant change in the system inertia and frequency nadir after a generation loss as with VSWTs [109], [110]. However, if a majority of the wind energy is captured by the VSWT technology, there would be a decline in inertia which in turn would pose a challenge to the operation and control of the future power system [109]. The high penetration of FPC based WTs needs to be planned as there will be a higher *RoCoF* and frequency deviations during power imbalances than in a purely conventional generation scenario [17], [103], [111]. A high *RoCoF* will result in unlimited tripping of loss-of-mains protection relays on distributed generators [85], with the large frequency deviation resulting in an increase in the need for frequency containment reserves in the power system.

In this chapter, analysis of the inertia contribution of WT generators to the GB power system is made. A supplementary controller designed to enable WTs to provide inertial support is discussed and the effectiveness of this controller is tested. A simplified three-machine representation of the GB grid incorporating VSWTs has been developed to carry out frequency studies. The machines represent the power systems of England and Wales, South Scotland and North Scotland. The frequency support capability of the WTs is analysed for different wind power penetration levels. The impact of wind speed and of supplementary inertia controllers on the level of frequency support and recovery power are also assessed. For completeness, the system response with and without frequency response is compared with an equivalent system featuring synchronous generation only.

3.2 Control of VSWTs

With increasing sizes of WTs, VSWTs became preferred to FSWTs. This is mainly because of the ability of VSWTs to comply with Grid Code connection requirements. With converter control in VSWTs, they can achieve rapid and accurate power regulation over a higher speed range than the synchronous machines which are not allowed to go beyond certain speeds [89]. Their rotor speeds can be controlled between 0.7 and 1.2 p.u. [112]. The DFIG and FPC based WTs are the most common variable-speed topologies [43]. PMSGs are used in WTs with FPC arrangements as they can be operated with and without a gearbox, a component that is a common source of failures. PMSGs have reduced losses and lighter weight than DFIGs, hence they are particularly suitable for larger WTs [43], [93].

A conventional VSWT control scheme is discussed in this section. Figure 3.1 below shows the control scheme of the PMSG-WT. It consists of 2 fully rated VSCs connected back-to-back. PWM is used to implement current controllers developed in the dq reference frame.

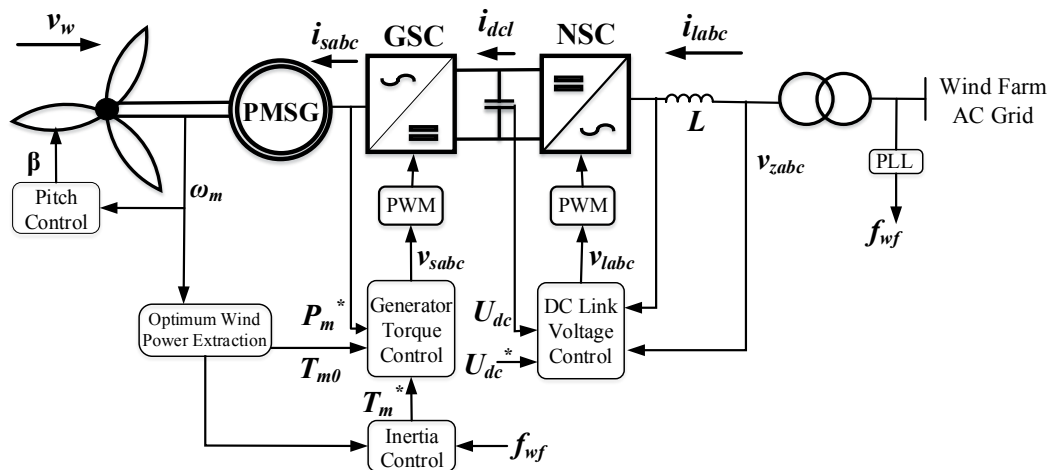


Figure 3.1: PMSG-WT control scheme.

3.2.1 Aerodynamic Model

The mechanical power extracted by the WT at wind speed V_w is described by the expression below:

$$P_m = 0.5\rho AC_p(\lambda, \beta)V_w^3 \quad (3.2)$$

$$T_m = P_m/\omega_t \quad (3.3)$$

where ρ is the air density (kg/m^3), A is the swept area of the turbine (m^2), C_p is the power coefficient which depends on the tip speed ratio λ and the turbine's pitch angle, β (deg), T_m is the mechanical/aerodynamic torque and ω_t is the rotational speed (rad/s) of the WT. C_p can be calculated either by using look-up tables or analytic formulations [113]. In this study, the analytic expression was used:

$$C_p = c_1 \left(c_2 \frac{1}{\Lambda} - c_3 \beta - c_4 \beta^{c_5} - c_6 \right) e^{-c_7 \frac{1}{\Lambda}} \quad (3.4)$$

where Λ is a function of β and λ given by.

$$\frac{1}{\Lambda} = \frac{1}{\lambda + c_8 \beta} - \frac{c_9}{1 + \beta^3} \quad (3.5)$$

and c_1, c_2, \dots, c_9 are real WT characteristics which are obtained by statistically analysing measured data of a real WT [113]. The tip speed ratio (TSR) of the WT is defined as:

$$\lambda = \frac{\omega_t R}{V_w} \quad (3.6)$$

where R is radius of the WT (m). The optimum wind power extraction control scheme uses the TSR to regulate the rotational speed of the turbine so that the maximum power can be extracted from the turbine depending on the wind speed [114]. This is described by

$$P_{opt} = K_{opt} \omega_t^3 \quad (3.7)$$

where K_{opt} is a constant or controller gain for tracking the maximum power [92]. It can be provided from the manufacturer [74] or calculated with the optimum power coefficient, $C_{p_{opt}}$ parameters [92].

3.2.2 Drive Train Model

The torque from the aerodynamic model is transferred to the PMSG through the drive train [74]. The drive train comprises the turbine, its shaft, the gearbox and the generator's rotor shaft. The drive train model in the PMSG studied here consists of a single mass with the rotors of the WT and generator directly coupled together by:

$$J_t \frac{d\omega_t}{dt} = T_m - T_e \quad (3.8)$$

T_e is the electro-magnetic torque and J_t is the inertia of the WT shaft.

3.2.3 Electrical Model of the PMSG

The PMSG equations are described by [93], [115], [116]:

$$\begin{aligned} u_{ds} &= -R_s i_{ds} + \omega_e L_s i_{qs} - L_s \frac{di_{ds}}{dt} \\ u_{qs} &= -R_s i_{qs} - \omega_e L_s i_{ds} - L_s \frac{di_{qs}}{dt} + \omega_e \psi_{pm} \\ T_m &= \frac{3}{2} n_p \omega_e i_{qs} \\ \omega_e &= n_p \omega_t \end{aligned} \quad (3.9)$$

where R_s is the stator winding resistance (Ω), L_s is the self-inductance (H) of the stator windings, ψ_{pm} is the flux linkage of the PMSG (Vs), u_{ds} , u_{qs} and i_{ds} , i_{qs} are the d and q axis stator voltages (V) and currents (A) respectively, ω_e is the electrical rotor speed (rad/s) and n_p is the number of pole pairs.

3.2.4 Back-to-Back Converters Controls

The generator-side converter (GSC) is used to control the torque or power from the WT. Figure 3.2 shows the control strategy for the GSC. The reference input is the torque from the PMSG. The q -axis current is used to control the torque from the

generator and the d -axis current can be used to control the reactive power [74]. Here, it is set to zero as unity power factor is desired, allowing the full VA rating of the converter for active power transfer. PI controllers control the currents and compute the output d -axis and q -axis voltages, which are used to generate PWM signals for the GSC. The reference q -axis current is calculated using:

$$i_{sq}^* = \frac{2}{3n_p} \frac{T_e^*}{\psi_{pm}}$$

$$i_{sd}^* = 0$$
(3.10)

where $T_e^* = K_{opt} \omega_t^2$ is the generator torque reference value [113].

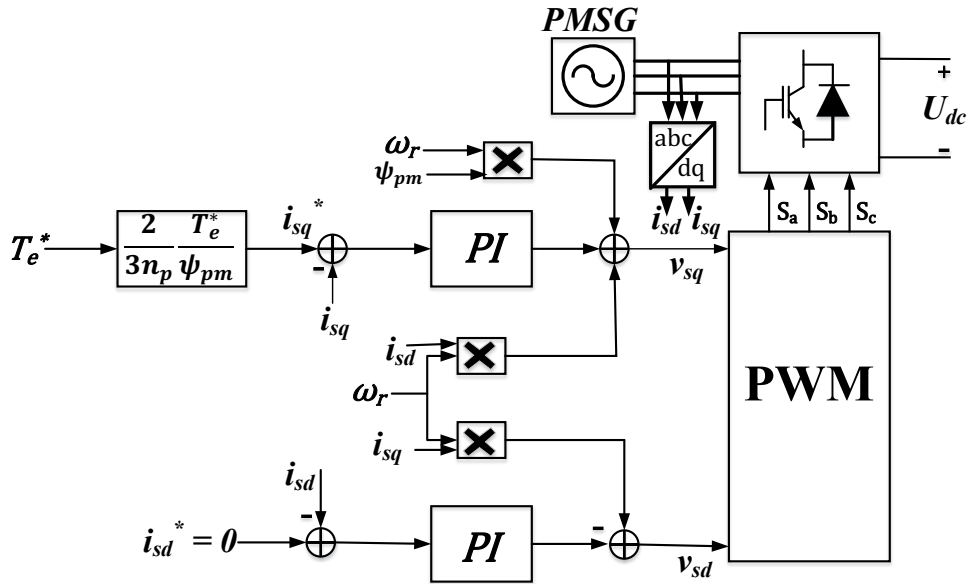


Figure 3.2: GSC control scheme for PMSG-WTs.

The network-side converter (NSC) shown in Figure 3.3 controls the dc voltage and regulates reactive power. The d -axis current is used to control the dc voltage while the q -axis current controls reactive power. The dc voltage reference is compared to measured dc voltage and its value is regulated using the PI controller of the outer control loop. The inner control loops of the current controllers produce the d -axis and q -axis voltages which will generate PWM signals for the NSC [93]. The dc link connecting the NSC and GSC is described by [116], [117]:

$$CU_{dc} \frac{dU_{dc}}{dt} = \frac{3}{2} (u_{ds}i_{ds} + u_{qs}i_{qs}) + \frac{3}{2} u_{Qg}i_{Qg} \quad (3.11)$$

where C and U_{dc} are the dc link capacitance and the dc link voltage respectively.

Figure 3.4 summarises entire PMSG-WT control scheme. Pitch control is used to control and operate the angle of the WT blades. When the wind speed is higher than the rated value, the pitch control takes over from the torque/speed control in order to limit input aerodynamic power. This is done by adjusting the pitch angle of the WT blades so that the rated output power can be maintained [43], [118]. Pitch angle control has also been used to provide primary frequency response from de-loaded WTs [43], [112]. The detailed WT parameters are given in Appendix II.

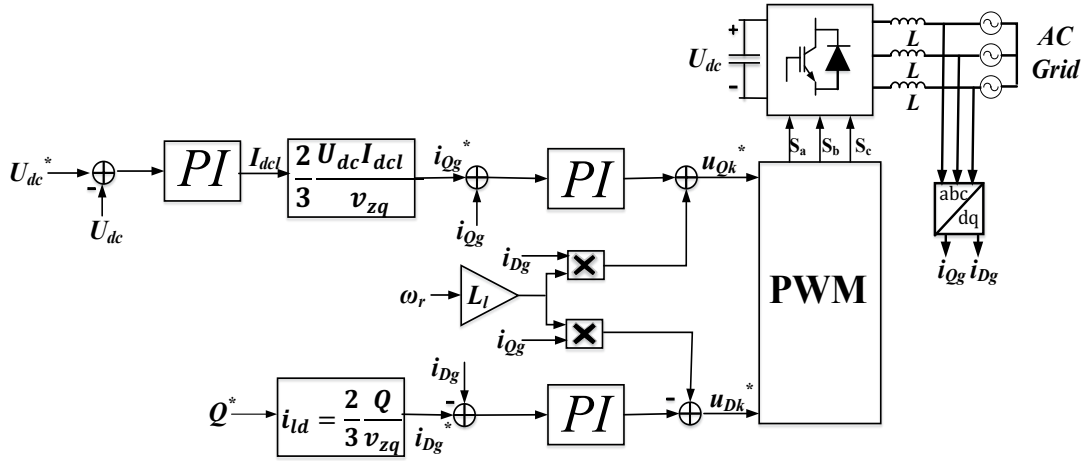


Figure 3.3: NSC control scheme for PMSG-WTs.

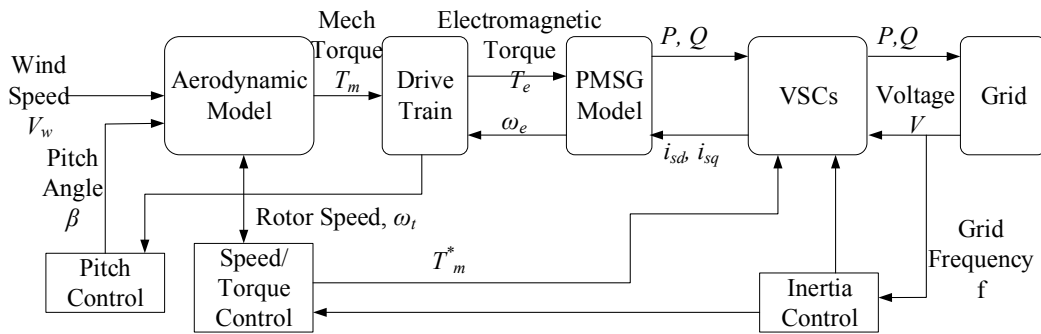


Figure 3.4: Summary of VSWT control scheme.

3.3 Inertial Contribution from WTs

To have variable speed operation, PMSG-based WTs are connected through power electronic converters [43]. They therefore do not naturally provide frequency support or inertia response because the ac grid frequency is decoupled from the PMSG frequency. However, with the addition of supplementary controls, during a power imbalance, the ac grid frequency can be detected by the PMSG-based WTs and can release their stored kinetic energy. The supplementary controller is usually fitted to the GSCs to regulate the torque or power reference depending on the system frequency deviation.

Several transmission system operators have now put into their grid codes the requirement for WPPs to provide inertial support such as Canadian Hydro-Quebec TransEnergie (HQT) [25], [119], ONS Brazil [120], IESO Ontario [121] and Irish TSO EirGrid. Wind manufacturer ENERCON has modelled a supplementary controller for provision of inertia response which also has an improved recovery behaviour, they have also performed field tests on their proposed solutions [25]. This shows that inertial contribution from VSWTs is important for the operation and control of a wind integrated future power system. Inertia response from WTs is discussed in section 2.8 of the literature review.

In this study, the TO scheme is selected for inertial support from the WTs. This is because the TO scheme is faster and stronger than the SI scheme as the additional power is not dependent on the real-time frequency deviation. Figure 3.5 shows a detailed representation of the temporary overproduction scheme as implemented in the computer simulations. A step increase in torque is applied for a predefined amount of time when a frequency deviation occurs. Filters are included to smoothen the step input to a first order response so that a sharp injection of energy is avoided. When a generation/load mismatch is detected, Δf is measured, and its output is passed through a comparator. If Δf is greater than the threshold deviation Δf_{th} defined in the comparator, the comparator produces an output of 1. The delay function is enabled as well. This holds the output for a period of time so that a step increase in torque is produced. This time can be selected based on the amount of time it takes to reach minimum rotor speed or can be defined by the system operator

[98]. A time duration of 7 s is selected here to reach the minimum rotor speed before allowing the turbine to begin accelerating again.

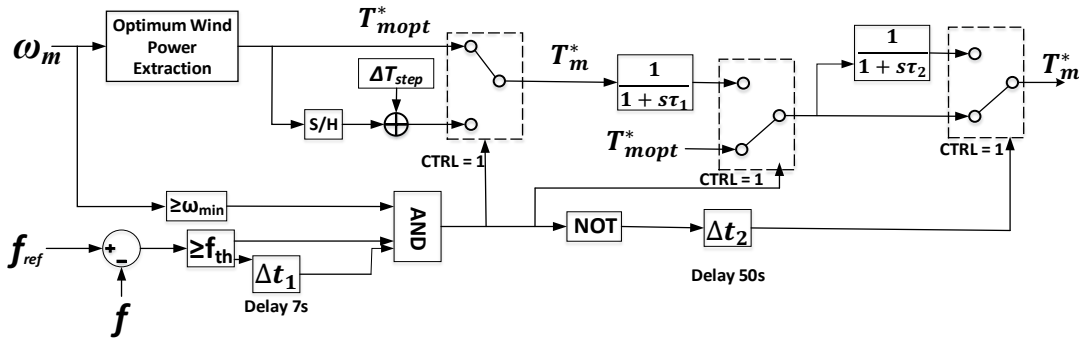


Figure 3.5: Temporary overproduction scheme for frequency support as implemented in PSCAD.

After the selected time elapses, the delay output becomes 0, and thus, the AND gate produces a low output. This output is then inverted by the NOT gate, which begins the reduction of the step torque back to the original value from the optimum wind power extraction control T_{mopt}^* before the generation/load mismatch occurred. The filter (with a time constant τ_2) allows for a first order behaviour in returning to the original torque value. The second delay Δt_2 of 50 s ensures that the control scheme does not immediately begin to operate again if there is another decline in frequency. This reduces the stress on the turbine shaft during the recovery period.

3.4 Test System Modelling

The effectiveness of the TO control to provide inertia support as an ancillary service is tested. The three-machine model shown in Figure 3.6 was adopted for this work. The synchronous machines represent the generating capacities of the GB system [122]. Each includes an exciter and governor control to fully characterise the inertial response. This system was initially designed to demonstrate the influence of wind generation on the dynamic behaviour and transient performance of the GB system [43]. The generators represent three generation areas Northern Scotland (owned by Scottish Hydro Electric Transmission plc), Southern Scotland (owned by Scottish Power Transmission Ltd SPT), and England & Wales network

(owned by National Grid Electricity Transmission plc NG). The model has been further modified to make it suitable for frequency response studies and built in PSCAD/EMTDC.

The system in Figure 3.6 is used as the reference case (i.e. 0% wind penetration) against which frequency support with an increase in wind penetration is compared. The three-machine model has been modified and upgraded to reflect a future GB energy mix which considers a large-scale connection of offshore WTs and synchronous generation. This is shown in Figure 3.7. With this proposed model, the impact of the inertial contribution from large-scale wind farms is studied. The system parameters of the three-machine model and WTs and the generators' electrical parameters are stated in the Appendix I.

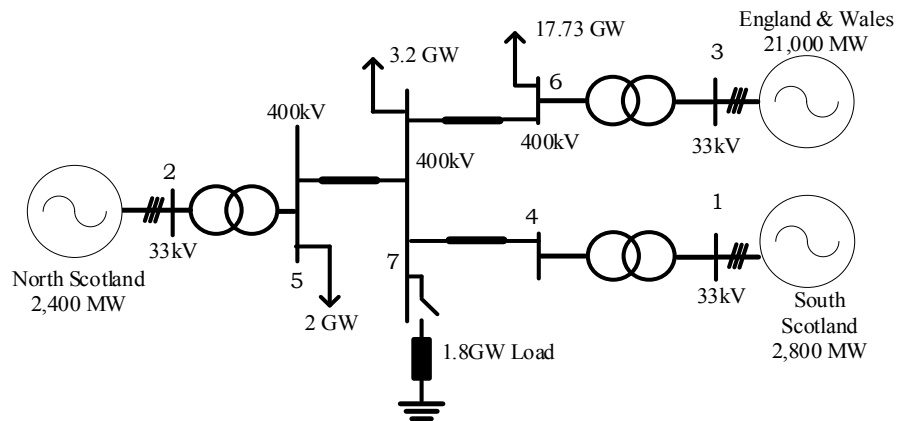


Figure 3.6: Three-machine model

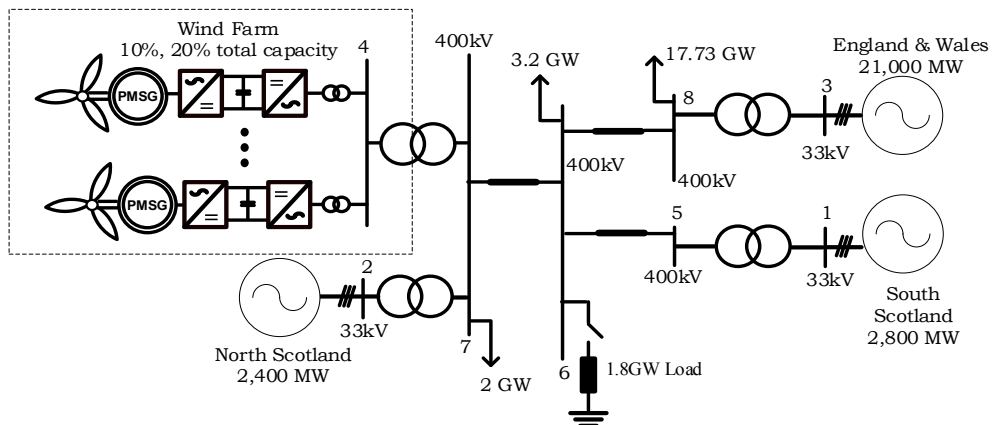


Figure 3.7: Modified three-machine model

3.5 Frequency Support at Different Penetration Levels

In this section, the frequency support capability of the three-machine GB power system at different wind penetration levels is analysed. The synchronous machines consider an aggregation of different fuel types. The total generation capacity in the system is 26.2 GW. If 10% of the total capacity is provided by offshore wind (i.e. 2.62 GW), then conventional generation would be reduced to 23.58 GW. As PMSG-WTs do not naturally contribute to the total power system inertia, Equation (3. 12) shows that when there is an $x\%$ penetration from WTs, the new power system inertia (unit:GVA.s) reduces by the same percentage.

$$H_{system,new} = (1 - x)H_{system} \quad (3. 12)$$

Figure 3.8 shows the frequency response of the test system due to varying levels of installed wind capacity at 10% and 20% penetration levels. A constant wind speed of 10.2 m/s has been assumed and the WTs are not equipped with the supplementary inertia controls. It can be observed that with a generation loss of 1800 MW occurring at 3s, which is the maximum infeed loss in the GB power system, the frequency deviation and *RoCoF* increase as the penetration of wind farm increases. However, there is a deeper drop in frequency at 20% penetration which goes below 0.8 Hz, which is the maximum allowable frequency deviation in the National Grid requirements upon loss of the largest infeed unit [123]. At higher penetrations of wind in the power system, there may be deeper frequency nadirs if no corrective action is taken. The sudden step and recovery in the frequency during the moment of disturbance is caused by a sudden angle change due to the sudden change in the power in the generators [31].

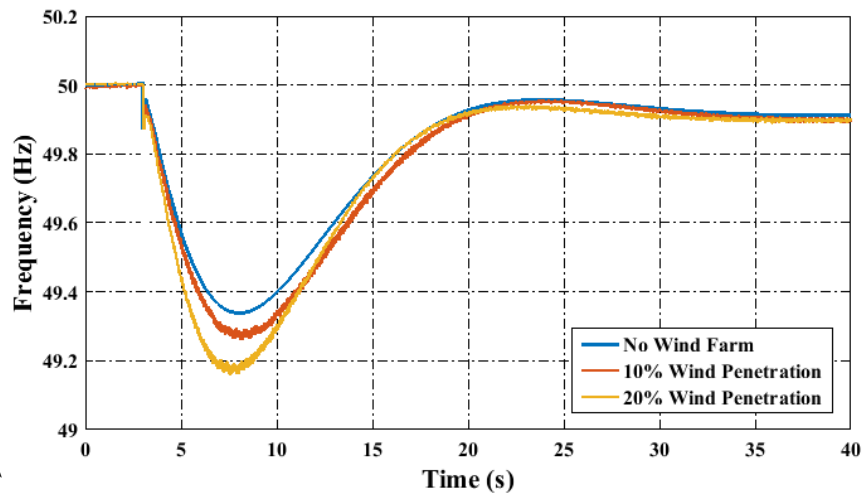


Figure 3.8: Impact of increasing wind penetration without supplementary controllers for frequency response. System frequency response after 1800 MW generation loss.

3.6 Inertial Contribution from PMSG-WTs - Case Study

The WT synthetic inertial contribution study is carried out on the system shown in Figure 3.7. Studies are made based on the following assumptions:

- Wind speed is the same for all WTs. This may not be the case in reality as they are dispersed geographically in the wind farm and may rotate at different speeds. However, this gives a good understanding of the frequency support capabilities at an averaged wind speed in the wind farm.
- As WT penetration increases, synchronous generation is reduced by the same percentage and the inertia constant also decreases.

The wind farm is made of aggregated 5 MVA PMSG-based WTs. The studies carried out in this work are discussed below:

- The performance of the frequency support scheme was tested at different wind speeds for a 10% wind penetration level.
- The impact of the different wind speeds on frequency support was assessed.
- The impact of the WT inertia controllers (i.e. filters and value of step torque) on frequency support was assessed.

Through the various studies, a load of 1800 MW is connected to the system at 3 s to simulate a sudden imbalance. The step increase in torque is applied for a period of 7 s.

3.6.1 Impact of Wind Speed on Frequency Support

The impact of the step response scheme at different wind speeds is studied. The step increase in torque was selected to be $\Delta T = 0.6$ p.u. This is applied from the wind farm when the frequency event occurs. Figure 3.9 shows the frequency and power curves. It can be observed that the WTs can provide more frequency support to the power system at a higher wind speed. It would be expected that frequency rises back to 50 Hz after the torque is removed. However, because of the recovery phase it instead drops to $\Delta f \approx 0.75$ Hz at a wind speed $V_w = 10.2$ m/s. It can be noticed that for a large value, $V_w = 12$ m/s the frequency reduces even further.

Figure 3.9(b) shows the additional active power transferred from the WTs to the ac grid. In the recovery phase, the rotor speed increases to its original value to get the WTs back to their point of optimum operation as before the imbalance. It can be observed that the recovery power is greater at higher wind speeds. At rated wind speed, the recovery power results in a further frequency drop on disturbed AC grids as shown. Therefore, the effect of the wind speeds on recovery power is recommended to be considered by manufacturers and TSOs in selecting control parameters and step torque values for planning inertial support from WTs.

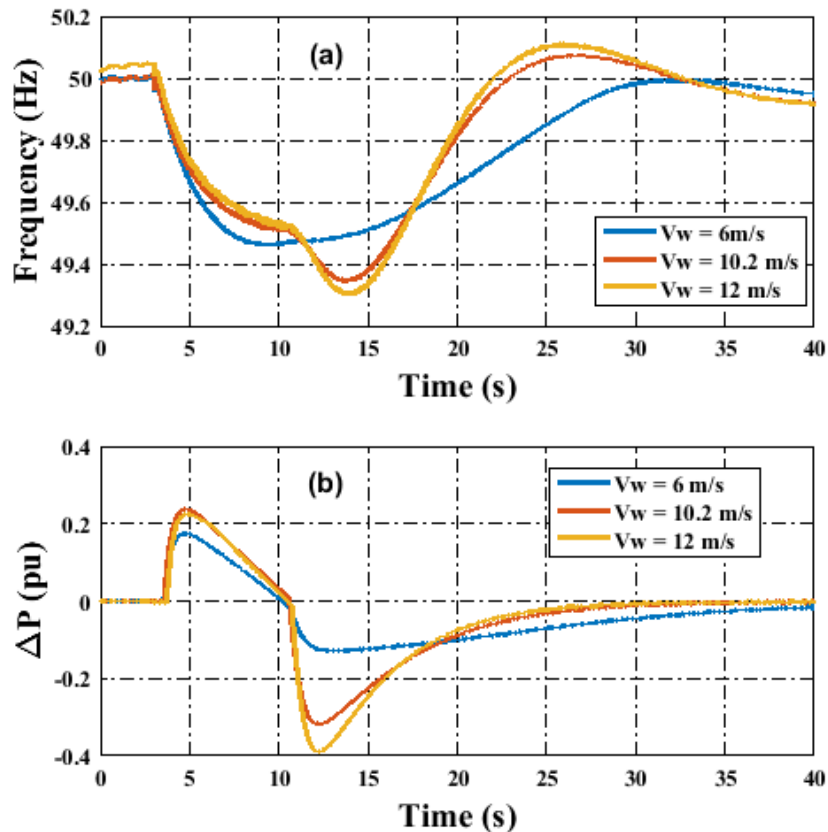


Figure 3.9: Effect of changing wind speed: System response after 1800 MW generation loss (a) System frequency response (b) Power supply from wind farm after imbalance.

3.6.2 Impact of Filters on WT Recovery Power

Section 3.6.1 showed that WTs have the capability to provide frequency response at various wind speeds. However, the recovery phase is an issue as it can cause a further dip in frequency. In this section, the filters that were included to smoothen the step input are further examined to analyse their impact on frequency support and during the recovery phase. To do this, the time constants of the filters shown in Figure 3.5 were changed incrementally so that an adequate system response can be achieved with as little recovery power as possible. The analysis is carried out for a 10% penetration level and 10.2 m/s wind speed. The step increase in torque is applied for a period of 7 s. The results are shown in Figure 3.10.

As it can be observed in Figure 3.10, when recovery begins, the system frequency drops further when filter time constants $\tau_1 = 0.5$ s and $\tau_2 = 0.5$ s (see Figure 3.5) are

used than when there is no frequency control. However, the situation improves if $\tau_1 = 0.08$ s and $\tau_2 = 7$ s are used. This extra decline in frequency occurs because the rotor speed rises faster, thus leading to a higher drop in power supply from the WTs. Additionally, the TO scheme reduces the frequency deviation from 0.72 Hz (no frequency control) to 0.69 Hz (TO method with $\tau_1 = 0.08$ s and $\tau_2 = 7$ s). The impact of changing the value of the step torque is studied next.

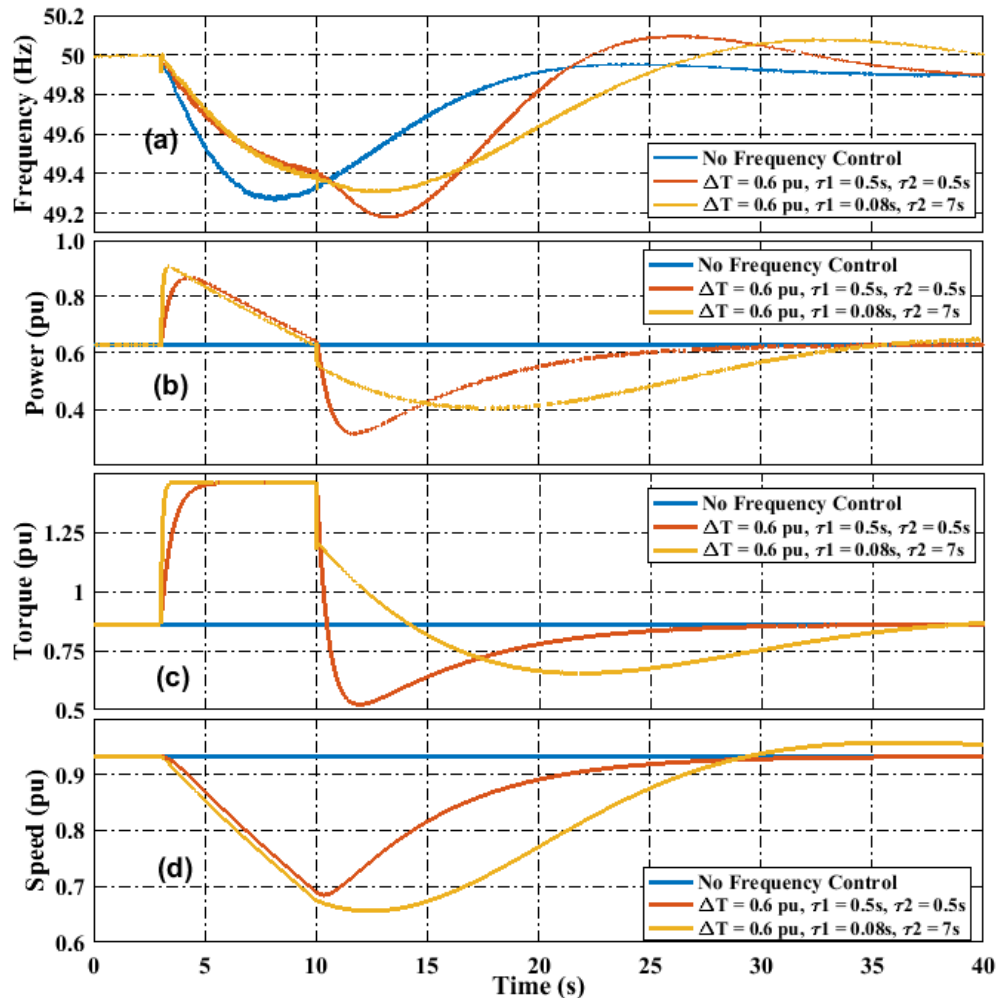


Figure 3.10: Impact of step torque controls - System response after 1800 MW generation loss (a) System frequency response (b) Power supply from wind farm after imbalance (c) Change in WT torque (d) Change in WT rotor speed.

3.6.3 Energy Capability of WTs due to Increased Torque

Further simulations are carried out to assess the effect of the step change in torque on frequency control. This is varied between 0.1 to 0.6 p.u. Time constants $\tau_1 = 0.08$

s and $\tau_2 = 0.7$ s are selected to reduce the recovery phase problem. Figure 3.11 shows the power and frequency curves. It can be observed in Figure 3.11(a) that the optimum step increase in torque is of 0.4 p.u., which renders the least frequency deviation; it provides an improvement over $\Delta T = 0.6$ p.u. which provides the lowest *RoCoF* but a higher frequency deviation than even the smallest step increase in torque of 0.1 p.u. A higher step in torque provides a quick burst of power but due to the higher recovery power that comes with it, it is least efficient. The frequency deviation, Δf and *RoCoF* are summarised in Table 3.1. To calculate the *RoCoF*, the frequency measurement is taken every 500 ms for the first 2 s of the event and for each measurement, the df/dt is calculated. Finally, the *RoCoF* is calculated as the average df/dt of the 4 values. The result shows that at $\Delta T = 0.4$ p.u, a low *RoCoF* and the lowest Δf are obtained.

Table 3.1: *RoCoF* and frequency deviation of case study while varyong step torque.

ΔT (pu)	Δf (Hz)	<i>RoCoF</i> (Hz/s)
0.1	0.67	0.2145
0.2	0.64	0.1941
0.4	0.59	0.1621
0.6	0.69	0.1405
No control	0.72	0.2288

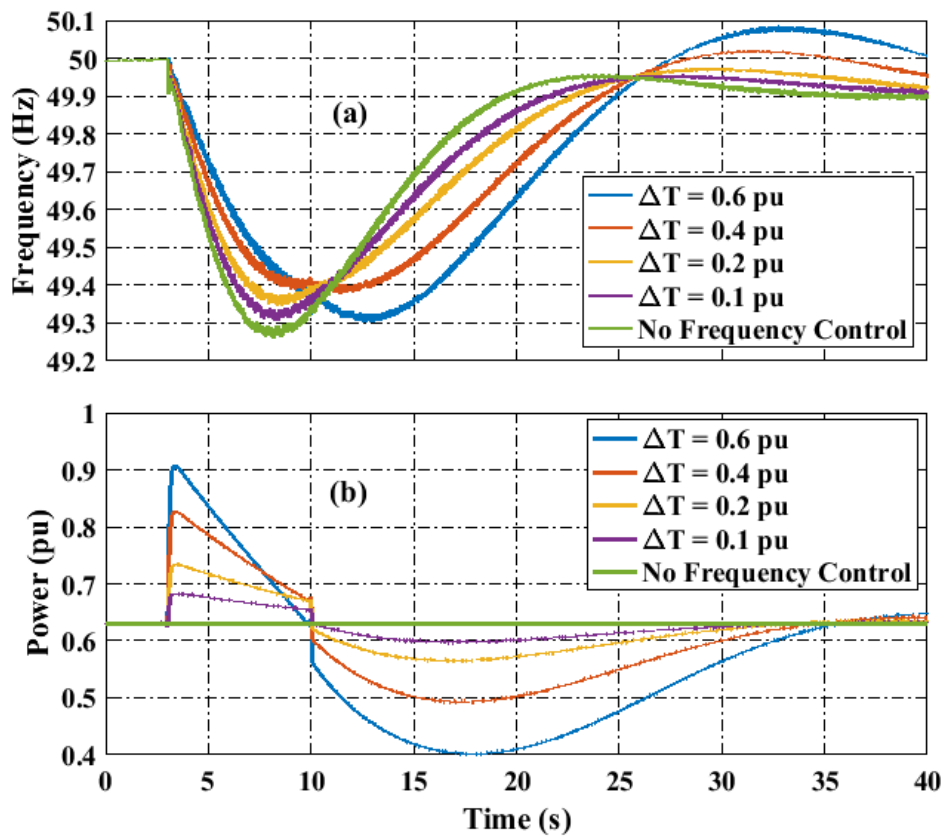


Figure 3.11: Effect of changing the step torque - System response after 1800 MW generation loss: (a) System frequency response, (b) Power supply from wind farm after imbalance.

3.7 Summary

The impact of the large-scale connection of FPC-based PMSG-WTs on the frequency response of the GB power system has been analysed. A modified three-machine model was developed to connect large amounts of wind farms to the GB power system.

The strategies for synthetic inertial response from VSWTs were discussed. The TO methodology for provision of synthetic inertial response was implemented in the WTs to demonstrate their frequency response capability. With this methodology, an additional power is provided for a short-predefined time through a step increase in the torque from the WTs.

The impact of the step increase in torque at generation/load imbalance periods has been examined. It was observed that a higher increase in torque may have a

negative impact on the system frequency stability due to the higher recovery energy especially when the wind speeds are average and high. There is less impact on the recovery energy at lower wind speeds like 6 m/s, however less power is produced at this period and this does not reduce the frequency nadir Δf and $RoCoF$ as much. It has been also shown that if the torque step increase value is correctly selected, it effectively reduces frequency deviations and the $RoCoF$ and that having a very high step torque increase does not necessarily mean more frequency support. The impact of different wind speeds on frequency response was also studied. It has been shown that the frequency deviation and $RoCoF$ are lower at higher speeds.

Chapter 4

Coordination of Fast Frequency Support from Multi-Terminal HVDC Grids and Offshore Wind Farms

4.1 Introduction

Given the projected change in the power generation mix and increase in power transfers via HVDC transmission, it is important to ensure the stability and security of the power system. Future MTDC grids such as the North-Sea grid will enable cross-border power trading and transfer of offshore wind energy between countries [124]. They must be able to participate in the provision of fast frequency support to connected ac grids. As previously discussed, HVDC-connected OWFs do not automatically respond to system imbalances like the HVAC-connected conventional synchronous generators. Several supplementary control schemes for the coordination of fast frequency support from VSC-MTDC have been proposed in the open literature [27]–[29], [103]–[105]. They have however assumed that not every ac system connected to the MTDC grid may require frequency support. Thus, previous research has fitted the auxiliary loops to a selected VSC which is connected to an ac grid that is assumed will require fast frequency support [26]–[28].

In this chapter, the behaviour of the MTDC system when all the onshore VSCs are upgraded with supplementary controllers is analysed. Undesirable power flows and reduced power transfers were found to occur. An auxiliary dead-band controller (ADC) is proposed to overcome these issues. A four-terminal HVDC integrated with an offshore wind farm is modelled in MATLAB/Simulink to analyse and study the effectiveness of three different supplementary fast frequency control algorithms. A small-signal stability analysis is also carried out to confirm that a stable system operation is maintained.

4.2 Modelling and Control of DC Grid Converters

In this section, the modelling and control of a dc grid is discussed. In a dc grid, maintaining the system voltage is crucial as it is an indicator of a stable operation [12]. This is because changes in the grid dc voltage will directly affect the grid power flows. Also, system disturbances such as faults and converter outage are automatically reflected in the grid's dc voltage. The dc voltage in an MTDC grid is

similar to the frequency in ac grids. When there is a loss/increase in demand in an ac grid, the system frequency rises/drops in response. Similarly, the dc voltage rises/falls when there is a deficit/surplus in the current (or power) flow in the dc grid [12]. Therefore, with the dc voltage being a crucial and global variable in the dc grid, controllers for ancillary services can be implemented using the dc voltage as the central variable. This removes the need for telecommunication between the dc grid terminals [106]. With the aid of supplementary frequency controllers for fast frequency support, the change in the ac grid frequency can be reflected directly on the dc voltage of the MTDC grid.

Onshore converter control in an MTDC grid ensures a correct power balance among converters. The architecture consists of a cascaded control loop structure based on dq transformations to achieve an independent control of active and reactive power. A fast-inner control loop regulates the d and q -axis currents. DC voltage, power, ac voltage and reactive power are controlled with outer loops [125], [126]. To this end, constant power, constant dc voltage or dc voltage-active power droop control can be used.

4.2.1 Droop Control

With droop control, a proportional relationship between the dc voltage and power is created [12]. As previously mentioned, the dc voltage control in a dc grid is analogous to frequency control in ac grids, therefore, the dc voltage will change in response to variations in dc current. This change in dc voltage can be used as an indicator for converters to share the power imbalance. Droop control also allows for redundancy in comparison to master-slave control [127]. It is depicted in Figure 4.1. The VSC-HVDC allows a degree of freedom in allowing independent control of reactive and active power. The reactive power can be controlled either by regulating the ac voltage at the PCC or by directly setting a reactive power setpoint. Also, the power flow in the grid can be controlled by creating a power setpoint or indirectly by controlling the dc voltage [128].

Droop control is employed in this study for dc voltage (V_{dc}) and power (P) control. The onshore GSCs employ V_{dc} - P control on the d -axis and reactive power (Q) or ac voltage (V) control on the q -axis.

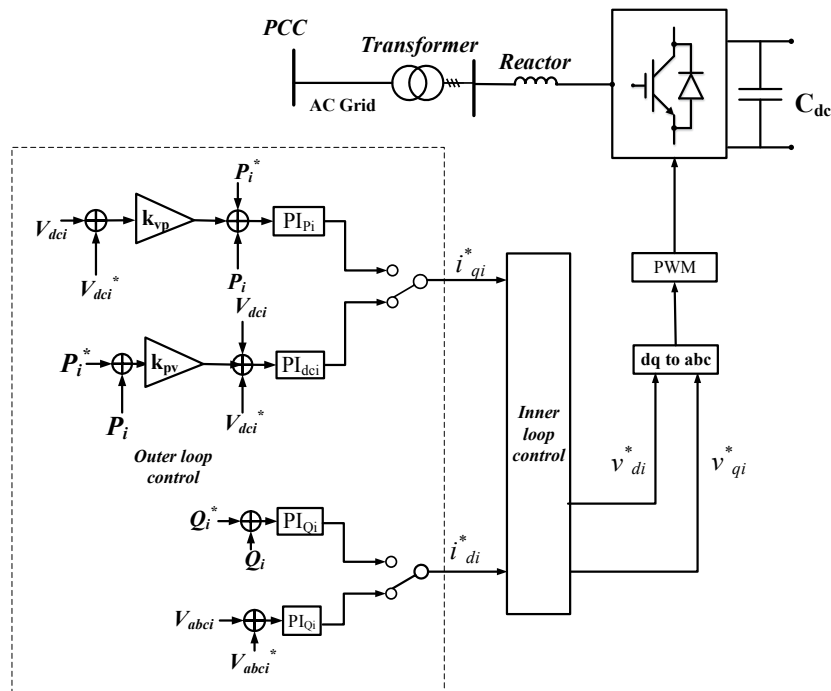


Figure 4.1: Droop control (inner loop not shown as its same as master-slave control).

4.3 VSC Modelling

The modelling of VSC and their controllers is described below [129]–[131]. A three-phase representation of the VSC showing the ac and dc sides is depicted in Figure 4.2.

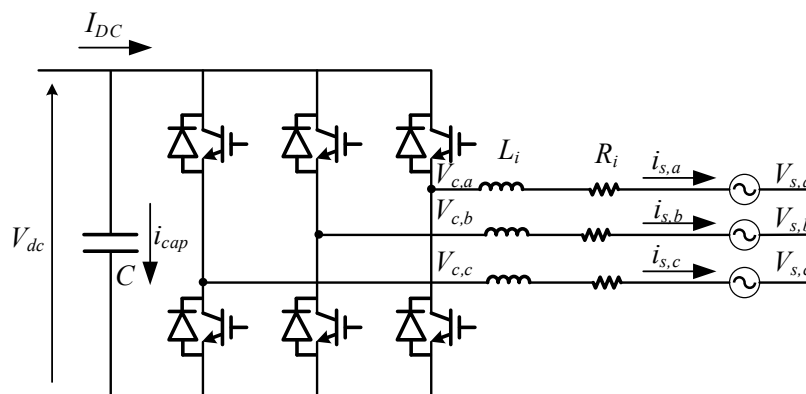


Figure 4.2: Three-phase representation of a VSC.

The ac side equation is represented as:

$$V_{c,abc} - V_{s,abc} = L_i \frac{di_{s,abc}}{dt} + R_i i_{s,abc} \quad (4.1)$$

where $V_{c,abc}$ and $V_{s,abc}$ are the ac voltages at the converter side and PCC and $i_{s,abc}$ is the ac current. L_i and R_i are total inductance and resistance respectively of the phase reactor and transformer at the VSC converter station.

This ac side dynamic of the converter station can be represented in the d - q reference frame as [128], [130], [132]:

$$\begin{aligned} L_i \frac{di_{sdi}}{dt} &= V_{cdi} - V_{sdi} + \omega_{si} L_i i_{sqi} - R_i i_{sdi} \\ L_i \frac{di_{sqi}}{dt} &= V_{cqi} - V_{sqi} - \omega_{si} L_i i_{sdi} - R_i i_{sqi} \end{aligned} \quad (4.2)$$

where V_{sdi} and V_{sqi} are the d and q axis voltages at the PCC. V_{cdi} and V_{cqi} are the d and q axis voltages at the converter terminal. i_{sqi} and i_{sdi} are the d and q current vectors.

4.3.1 Inner-loop Controllers

The inner current control loop of the VSC is shown in Figure 4.3. This is expressed mathematically as:

$$\begin{aligned} V_{cqi}^* &= k_{pi}(i_{sqi}^* - i_{sqi}) + k_{ii} \int (i_{sqi}^* - i_{sqi}) dt + \omega L_i i_{sdi} \\ V_{cdi}^* &= k_{pi}(i_{sdi}^* - i_{sdi}) + k_{ii} \int (i_{sdi}^* - i_{sdi}) dt - \omega L_i i_{sqi} + V_{sdi} \end{aligned} \quad (4.3)$$

V_{cqi}^* and V_{cdi}^* are the voltage references generated in the inner-loop control. They are transformed back into V_{abci}^* by Park transformation and this voltage reference is sent to generate PWM signals for the converter. k_{pi} and k_{ii} are the proportional and integral gains of the PI controller; i_{sdi}^* and i_{sqi}^* are the reference d and q axis currents from the outer loop controller (described in the next section). To simplify the expressions in (4.3), let:

$$z_{iq} = k_{ii} \int (i_{sqi}^* - i_{sqi}) dt$$

$$z_{id} = k_{ii} \int (i_{sdi}^* - i_{sdi}) dt \quad (4.4)$$

Therefore, the inner loop equations (4.3) $V_{cqi}^* = k_{pi}(i_{sqi}^* - i_{sqi}) + k_{ii} \int (i_{sqi}^* - i_{sqi}) dt + \omega L_i i_{sdi}$ can be simplified as:

$$\begin{aligned} V_{cqi}^* &= k_{pi}(i_{sqi}^* - i_{sqi}) + z_{iq} + \omega L_i i_{sdi} \\ V_{cdi}^* &= k_{pi}(i_{sdi}^* - i_{sdi}) + z_{id} - \omega L_i i_{sqi} + V_{sdi} \end{aligned} \quad (4.5)$$

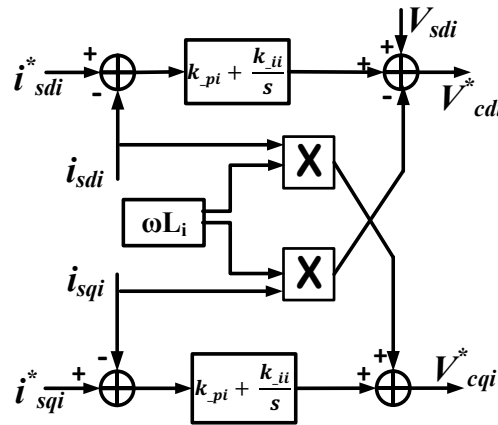


Figure 4.3: Inner loop control of a VSC.

The VSC output reactive and active power are expressed in (4.6). This shows that the active power and reactive power are proportional to the d and q axis current respectively; thus, indicating decoupled control in VSCs.

$$\begin{aligned} P &= \frac{3}{2}(V_{cqi}i_{sqi} + V_{cdi}i_{sdi}) = \frac{3}{2}V_{cdi}i_{sdi} \\ Q &= \frac{3}{2}(V_{cqi}i_{sdi} - V_{cdi}i_{sqi}) = -\frac{3}{2}V_{cdi}i_{sqi} \end{aligned} \quad (4.6)$$

4.3.2 Outer-loop Controllers

The outer loop controllers are shown in Figure 4.4. They are designed to be slower than the inner loop current controller to ensure stability [128]. They also use PI controllers to compute the current references i_{sqi}^* and i_{sdi}^* , which are input to the inner loop controllers described in the previous section. Droop control is used in this study for the power and dc voltage control, while constant reactive power

control is used. The equations of the P - V_{dc} controller and Q control are expressed as:

$$\begin{aligned} i_{sqi}^* &= k_{pdci} [k_{pvi}(P_i^* - P_i) + V_{dci}^* - V_{dci}] \\ &\quad + k_{idci} \int [k_{pvi}(P_i^* - P_i) + V_{dci}^* - V_{dci}] dt \\ i_{sdi}^* &= k_{pQi}(Q_i^* - Q_i) + k_{iQ} \int (Q_i^* - Q_i) dt \end{aligned} \quad (4.7)$$

To simplify the expressions in (4.7), let:

$$\begin{aligned} z_{Pi} &= k_{idci} \int [k_{pvi}(P_i^* - P_i) + V_{dci}^* - V_{dci}] dt \\ z_{Qi} &= k_{iQ} \int (Q_i^* - Q_i) dt \end{aligned} \quad (4.8)$$

Therefore, the outer loop equations (4.7) can also be simplified as:

$$\begin{aligned} i_{sqi}^* &= k_{pdci} [k_{pvi}(P_i^* - P_i) + V_{dci}^* - V_{dci}] + z_{Pi} \\ i_{sdi}^* &= k_{pQi}(Q_i^* - Q_i) + z_{Qi} \end{aligned} \quad (4.9)$$

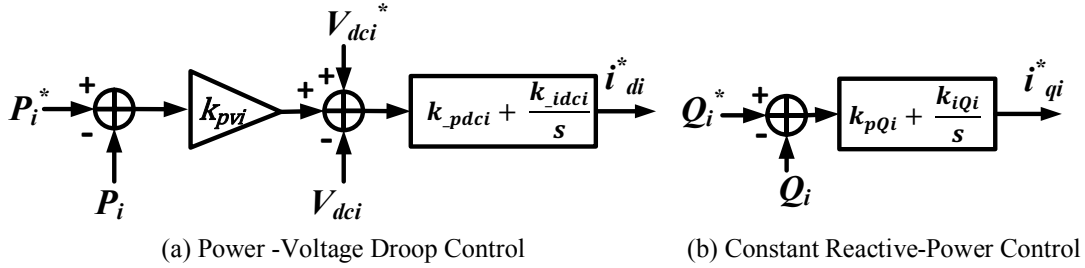


Figure 4.4: Droop control of VSC in study.

4.3.3 DC Link

The dc line is represented as inductances and resistances [130], [133]. The dc link voltage is calculated as:

$$\frac{dV_{dc}}{dt} = -\frac{(V_{cdi}i_{sdi} + V_{cqi}i_{sqi})}{CV_{dc}} + \frac{I_{dc}}{C} \quad (4.10)$$

where V_{dc} is the dc link voltage, I_{dc} is the dc current and C is dc link capacitance. The values of R and L are not used in this calculation as they are only needed in defining the current along the dc line. This level of detail is not needed in this study.

4.4 Wind Farm Converter Control

The OWF is an ac grid. Its wind farm side VSC or wind farm converter (WFC) creates a fixed magnitude ac voltage (V_{ac}) at a given frequency and phase angle [134]. The WFC ensures that all power produced in the OWF is transferred to the dc grid [99]. A variable operation of the offshore grid frequency (f_{off}) is possible without affecting the OWF operation since there are no likely loads in the offshore ac grid. This variable frequency operation allows power flow regulation for fault-ride through control, inertial and fast frequency support to the dc grid and onshore ac grids [12], [134]. The control of the WFC is depicted in Figure 4.5.

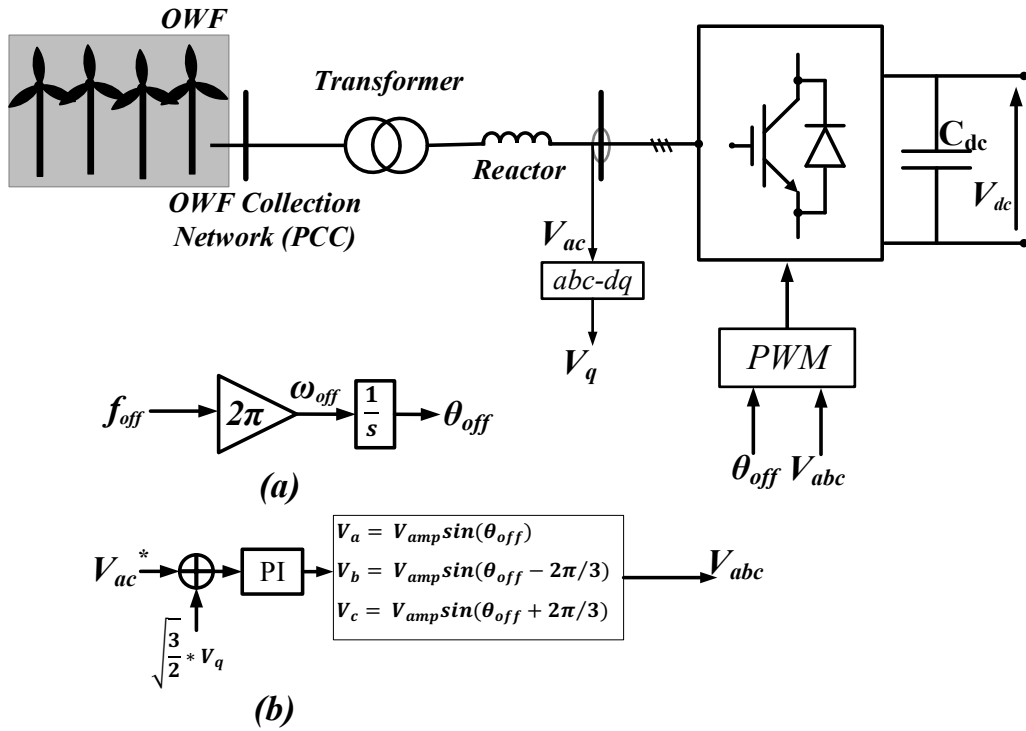


Figure 4.5: Wind farm converter control.

4.4.1 WTs Temporary Overproduction

The OWF is made of 150 aggregated FRC WT units of 5 MVA each based on PMSGs. The OWF has a total rated capacity of 750 MVA. It is assumed that the OWF operates at wind speed of 10.5 m/s and MPP tracking is used to regulate the rotational speed of the generator to obtain the maximum power. The PMSG-WT control scheme and TO strategy for inertia emulation have been discussed in

Chapters 2 and 3. For frequency support provision for OWFs connected via HVDC transmission, the WFC must be fitted with a supplementary $V_{dc} - f$ droop controller [28], [29]. This varies the frequency of the offshore ac system of the wind farm based on changes to the dc voltage according to:

$$f_{off} = f_{off,0} - k_{off}(V_{dc,0} - V_{dc}) \quad (4.11)$$

where k_{off} is the dc voltage-frequency droop gain, f_{off} is the offshore ac grid frequency, and $f_{off,0}$ is the reference frequency. The $V_{dc}-f$ droop scheme is depicted in Figure 4.6. The WT parameters are provided in Table 4.1.

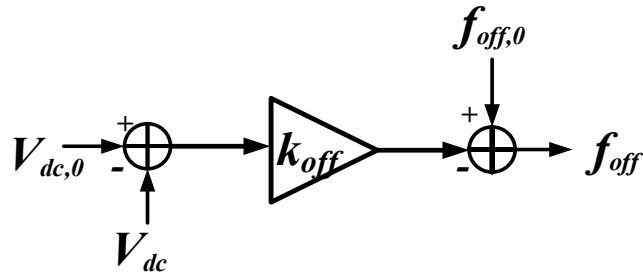


Figure 4.6: DC voltage - frequency droop for frequency support from wind farms.

Table 4.1: WT parameters.

Parameters	Rating
Pole Pairs	125
Wind Speed	10.5 m/s
Rotor Speed	1.4 rpm
Coherent machines	150
Inertia	$30 \cdot 10^6 \text{ kg} \cdot \text{m}^2$
Operated Power	5 MVA
AC Voltage	690 V
DC Voltage	$\pm 600 \text{ V}$

4.5 Simplified power system model

The ac systems in this study are modelled as simplified power systems. These represent synchronous power plants such as coal, gas, nuclear and hydro. Their frequency response to a power imbalance, such as increase or decrease in demand, where they increase or decrease their power output respectively is also represented.

These machines are represented by control blocks having a governor droop, governor actuator and a turbine. The simplified power system model is based on the swing equation, where the relationship between inertia (H_{eq}) and load variation is given [135]. The simplified model is depicted in Figure 4.7 [31], [136] and it is used in this chapter to represent the onshore ac power systems. The system parameters are stated in Appendix III.

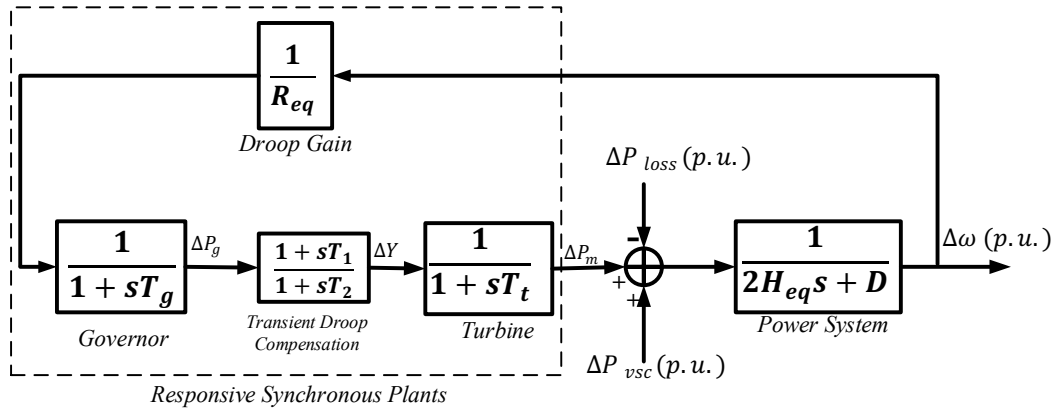


Figure 4.7: Simplified power system model.

As shown in Figure 4.7, R_{eq} , is the governor droop which controls the speed of the turbines. It is the combined effect of the droops of the speed governors of all the generators which the simplified model represents. T_g and T_t are the governor and turbine time constants. The lead/lag function with time constants T_1 and T_2 represents the transient droop compensation to ensure a stable performance of the speed control [73], [136]. A governor dead-band is also included which reduces the system's sensitivity to smaller changes in frequency and to only respond above 0.02 Hz change in system frequency. The equations describing the simplified power system are:

$$\Delta\omega = \frac{1}{2H_{eq}s + D} (\Delta P_m - \Delta P_{loss} + \Delta P_{vsc}) \quad (4.12)$$

$$\Delta P_g = \frac{1}{R_{eq}} \left(\frac{1}{1 + sT_g} \right) \Delta\omega \quad (4.13)$$

$$\Delta Y = \Delta P_g \left(\frac{1 + sT_1}{1 + sT_2} \right) \quad (4.14)$$

$$\Delta P_m = \left(\frac{1}{1 + sT_t} \right) \Delta Y \quad (4.15)$$

where $\Delta\omega$ is the deviation in the grid frequency in per unit, ΔP_g is the input signal to the governor from the power system, ΔP_{vsc} is the change in power to or from the VSC converter connected to the ac grid, ΔP_m is the generated power deviation obtained when the synchronous plants respond to a generation loss or increase in demand, ΔP_{loss} and ΔY is the output from the lead-lag function and is the input to the turbine.

4.6 MTDC Fast Frequency Support Schemes

The fast frequency control schemes aim to provide quick power transfer from OWFs or from other ac systems connected to the dc grid. They are briefly described next.

4.6.1 Coordinated Control Scheme

Shown in Figure 4.8, the coordinated control (CC) scheme [26] uses a P - V_{dc} droop during normal operation ($f_{on,0} - f_{on} < \Delta f_{db}$) but then switches to a supplementary f - V_{dc} droop following a frequency disturbance ($f_{on,0} - f_{on} \geq \Delta f_{db}$). This can be expressed as follows:

$$\begin{cases} V_{dc}^* = V_{dc,0} - k_{pv}(P_{dc,0} - P_{dc}), & \text{if } (f_{on,0} - f_{on}) < \Delta f_{db} \\ V_{dc}^* = V_{dc,0} + k_{fv}(f_{on,0} - f_{on}), & \text{if } (f_{on,0} - f_{on}) \geq \Delta f_{db} \end{cases} \quad (4.16)$$

where k_{pv} is the active power-dc voltage droop gain and k_{fv} is the frequency-dc voltage droop gain. The f - V_{dc} droop transforms the ac frequency deviation into a proportional dc voltage signal which, in turn, modifies the reference value of the dc voltage at the VSC terminal. After recovery from the disturbance, the system will dead-band set-point of the frequency support loop [26]. A sample-and-hold block is used to hold the pre-disturbance value of the dc voltage when switching to f - V_{dc} droop occurs. This prevents adverse transients from occurring during the switching [26].

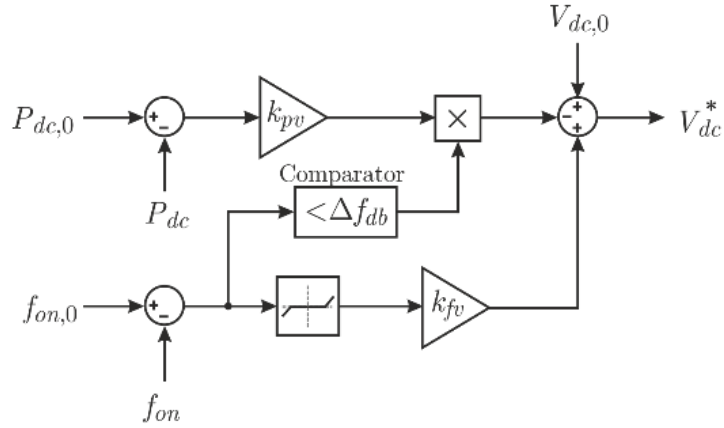


Figure 4.8: CC scheme.

4.6.2 Alternative Coordinated Control Scheme

Shown in Figure 4.9, the alternative coordinated control (ACC) [28] scheme uses a V_{dc} - P droop during normal operation and switches to a f - P droop during a disturbance. It is expressed as:

$$\begin{cases} P_{dc}^* = P_{dc,0} - k_{vp}(V_{dc,0} - V_{dc}), & \text{if } (f_{on,0} - f_{on}) < \Delta f_{db} \\ P_{dc}^* = P_{dc,0} + k_{fp}(f_{on,0} - f_{on}), & \text{if } (f_{on,0} - f_{on}) \geq \Delta f_{db} \end{cases} \quad (4.17)$$

with

$$k_{fp} = \frac{k_{fv}}{k_{pv}}, \quad k_{vp} = \frac{1}{k_{pv}},$$

where k_{vp} is the dc voltage-active power droop gain (defined as the inverse of k_{pv} for an active power-dc droop gain, see Section 4.6.1) and k_{fp} is the frequency-power droop gain (defined in terms of the droop gains of the CC scheme). After the disturbance event is over, the system will return to the original V_{dc} - P droop when $(f_{on,0} - f_{on}) < \Delta f_{db}$. Similarly, a sample and hold block is also used here during the switch process to hold the pre-disturbance active power value.

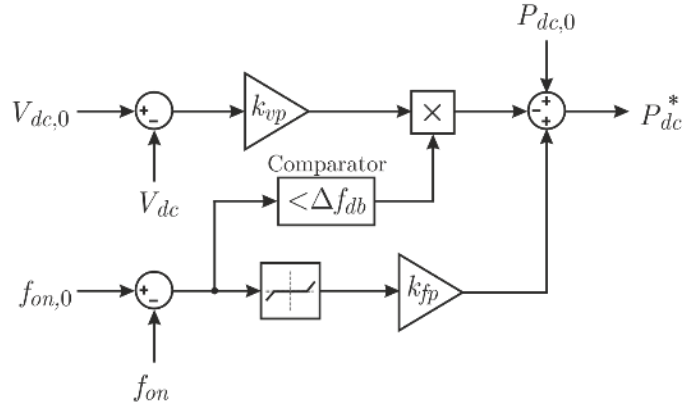


Figure 4.9: ACC scheme.

4.6.3 Dual-Loop Control Scheme

The dual-loop control (DLC) scheme [27] is similar to the CC scheme. However, it combines the frequency and voltage droop control techniques unlike the CC scheme, where the active power-voltage droop is deactivated when the frequency-voltage droop is in use. It is shown in Figure 4.10. The DLC scheme is mathematically expressed below:

$$\begin{cases} V_{dc}^* = V_{dc,0} - k_{pv}(P_{dc,0} - P_{dc}), & \text{if } (f_{on,0} - f_{on}) < \Delta f_{db} \\ V_{dc}^* = V_{dc,0} - k_{pv}(P_{dc,0} - P_{dc}) + k_{fv}(f_{on,0} - f_{on}), & \text{if } (f_{on,0} - f_{on}) \geq \Delta f_{db} \end{cases} \quad (4.18)$$

During normal operation, the P - V_{dc} droop is in operation and when a frequency disturbance is detected (i.e. $f_{on,0} - f_{on} < \Delta f_{db}$) the f - V_{dc} droop is activated and works simultaneously with the P - V_{dc} droop [27]. It is a non-switching frequency control scheme.

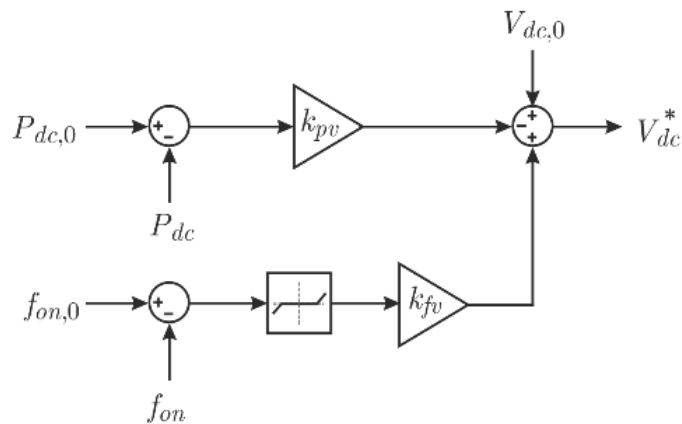


Figure 4.10: DLC Scheme.

4.6.4 Drawbacks of Fast Frequency Control Schemes

When an ac system connected to an MTDC grid experiences a power disturbance, other ac grids connected to the dc grid will respond to provide support to the disturbed grid if droop control is used. While providing support, the responding ac grids will also experience a decline in their own frequencies. These frequency variations could exceed the dead-band set on their VSC terminal and, in turn, activate the fast frequency support schemes of the VSCs connected to them (if fitted with supplementary controllers). As a result, their voltage-power droop would be automatically disabled. Under this circumstance, no VSC in the MTDC grid will regulate the dc voltage and instability may arise. Thus, it is important to coordinate the dead-band set-point of the frequency control algorithms fitted to the different converters so that stable power flows and power transfer capability can be restored during multiple ac frequency variations.

It should be borne in mind that a future MTDC grid may encompass different control methodologies –including those presented here. It would be possible that the described drawback is not applicable if a converter within the dc grid is always controlling dc voltage. However, the presence of a dc voltage controlling converter on its own would undermine the distributed control principle of droop control [102].

4.7 Auxiliary Dead-band Controller

An auxiliary dead-band controller (ADC) is proposed to coordinate the provision of fast frequency support in an MTDC grid and eliminate the drawbacks mentioned in Section 4.6.4. Figure 4.11 shows the ADC scheme. It discriminates between the VSCs connected to disturbed ac grids from those connected to responding ac grids during fast frequency support.

The ADC is connected at each converter station and is used in conjunction with the converter’s supplementary frequency controller discussed in Section 4.6. The ADC operates as follows: it uses the local frequency measurement of the ac grid it is connected to and uses this measurement to calculate frequency deviation Δf and the $RoCoF$. The value of Δf is passed through a comparator block and if it is greater than a threshold value of 0.02 Hz, an output of 1 is produced (otherwise the output is 0). The frequency deviation threshold of 0.02 Hz is selected as established by ENTSO-E [12], [86]. Similarly, the $RoCoF$ measurement is compared to a threshold of 0.1 Hz/s. If its value is greater than the threshold, an output of 1 is produced (otherwise an output of 0 is obtained). It should be highlighted that the $RoCoF$ threshold value of 0.1 Hz/s is less than the current set-point of 0.25 Hz/s, which is employed to trigger protection devices [80], [138]. In the simulation, the frequency measurements do not have much noise and thus does not need to be filtered before being input to the derivative block. In reality, this will not be the same and the frequency measurement will need to be passed through a filter as will be shown in Chapter 5.

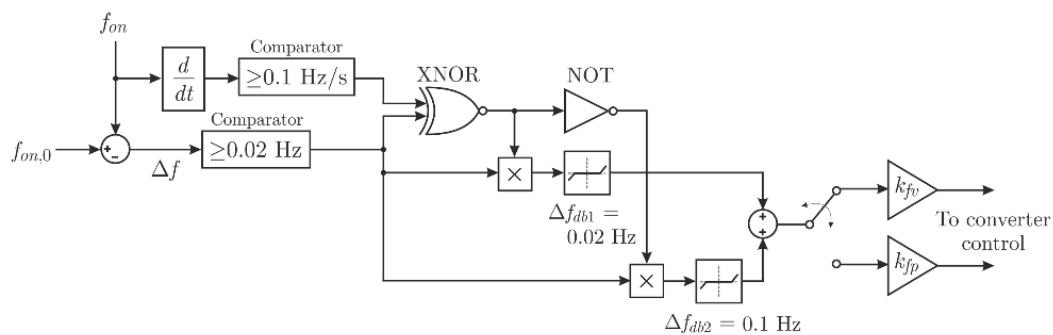


Figure 4.11: Proposed auxiliary dead-band controller.

The outputs from the Δf and $RoCoF$ comparators are then sent to an XNOR gate, which produces a true (1) output when all its inputs are either false (0) or true (1). Its logic is shown in Table 4.2. This way, the XNOR gate can produce an output which enables the modification of the dead-band set-point of the supplementary frequency controllers. For instance, when the XNOR output is 0, the dead-band set-point will be 0.1 Hz; conversely, when it is 1, the dead-band will be set to 0.02 Hz.

Table 4.2: ADC XNOR logic.

$RoCoF$ (Hz/s)	Δf (Hz)	XNOR gate	Dead-band value
≥ 0.1	≥ 0.02	1	0.02
≥ 0.1	≤ 0.02	0	0.1
≤ 0.1	≥ 0.02	0	0.1
≤ 0.1	≤ 0.02	1	0.02

With the ADC logic, the ac systems which are troubled (i.e. experiencing a frequency disturbance) can be distinguished from the ac systems which are responding (to a frequency event in another ac system). During normal ac grid operation, the ADC logic allows all the supplementary controllers dead-band set-points to be 0.02 Hz. This is the normal mode where their Δf and $RoCoF$ are all less than 0.02 Hz and 0.1 Hz/s; thus, the XNOR gate produces a true (1) output in all controllers which corresponds to a dead-band value of 0.02 Hz. During a frequency disturbance, the $RoCoF$ and Δf begin to change. In the troubled grid, its Δf and $RoCoF$ values will exceed 0.02 Hz and 0.1 Hz/s, respectively and a true output (1) is still produced on both Δf and $RoCoF$ comparators (see Figure 4.11) which leads to a true (1) output from the XNOR gate (see Table 4.2). This implies that the dead-band value of $\Delta f_{ab1} = 0.02$ Hz is kept. In converters connected to the responding ac grids, the ADC logic will produce a dead-band value of 0.1 Hz. This is because although Δf may become higher than 0.02 Hz due to the active power they are transferring to the disturbed grid for frequency support; however, their measured $RoCoF$ may be less than 0.1 Hz/s. Under these circumstances, an XNOR output of 0 is produced, which the NOT gate inverts to 1. This in turn changes the dead-band from $\Delta f_{ab1} = 0.02$ Hz to $\Delta f_{ab2} = 0.1$ Hz in the responding converters. This ability to manipulate the dead-band with the ADC logic, allows the controllers in the

responding grids to be less sensitive when they are providing frequency support and prevents them from entering the frequency sensitive mode. When they are done providing the support, their dead-band values will return to 0.02 Hz (because their frequency deviation would have returned to being less than 0.02 Hz).

It is important to note that the ADC only uses the local frequency measurement of its own grid. The ADC will allow for stable operation of the dc grid during fast frequency support and prevents the need for communications in determining which ac grid requires frequency support.

4.8 Test System

The four-terminal VSC-HVDC test system shown in Figure 4.12 is used to compare the effectiveness of the fast frequency control schemes presented in Section 4.6. The converters of the test system are modelled as averaged VSCs and have been implemented in MATLAB/Simulink. The MTDC system interconnects three separate ac grids to an OWF. The OWF and ac grid 3 (i.e. GSC3) export power into the dc grid. The OWF will also contribute to the fast frequency support via TO (as discussed in Section 4.4.1). The parameters of the four-terminal system, the ac systems and the control gains of the frequency support schemes are summarised in Appendix III. The ac grids are represented using simplified models with a base load capacity of 40 GW [31], [76]. Simplified models are used, and large sized systems do not need to be modelled because the focus is on the MTDC's ability to provide frequency support and not on the ac system's frequency support capability.

Averaged models are employed instead of switching models since the studies performed do not require a detailed representation of the fast switching dynamics of power electronic converters. The adoption of averaged models also reduces the computational requirements [12].

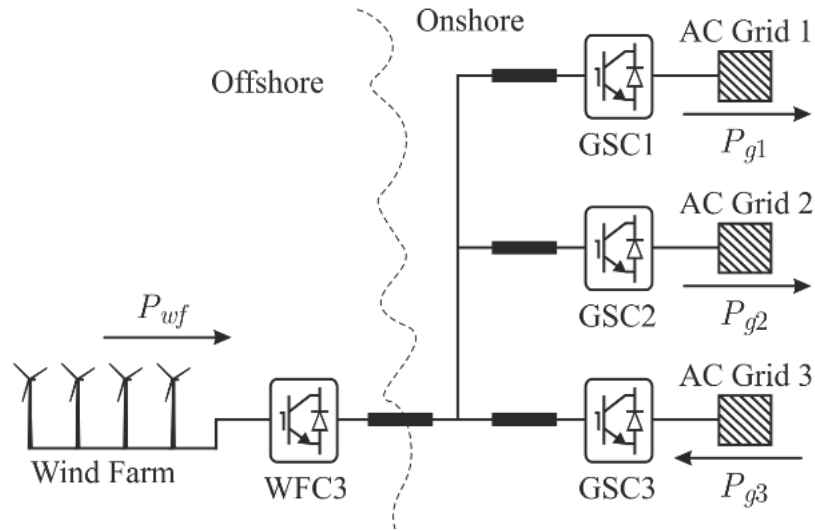


Figure 4.12: Four terminal VSC-HVDC test system.

4.9 Small-Signal Stability Study

To ensure that the supplementary frequency controls do not negatively affect the stability of the system, the small-signal model of the MTDC grid combined with the CC scheme for fast frequency support is derived. The small-signal analysis shows the effect of the fast frequency control on the system modes and damping. In this section, the mathematical modelling of the test system is described to perform small signal stability studies.

The system signal model includes the dynamic equations of the four VSCs, the wind farm controls and the three ac grids. These equations have been described in sections 4.3, 4.4 and 4.5. The combined MTDC grid and fast frequency controllers can be described by the following state equation:

$$\Delta \dot{X} = A \Delta X$$

$$\Delta X = [X_{ACgrid1} \ X_{ACgrid2} \ X_{ACgrid3} \ X_{GSC1} \ X_{GSC2} \ X_{GSC3} \ X_{WFC3} \ X_{WF}]^T \quad (4.19)$$

where $X_{ACgrid1}$, $X_{ACgrid2}$ and $X_{ACgrid3}$ are the state variables of the AC grids 1, 2 and 3 respectively. X_{GSC1} , X_{GSC2} and X_{GSC3} are the states variables of the grid side converters, X_{WFC3} represents WFC3 state variables and X_{WF} represents the wind farm state variables. The system is of the 39th order. The components of the state variables are given as:

$$\begin{aligned}
 X_{ACgridi} &= [\Delta\omega_i \ \Delta P_{gi} \ \Delta Y_i \ \Delta P_{mi}] \\
 X_{GSCi} &= [\Delta i_{sdi} \ \Delta i_{sqi} \ \Delta z_{iq} \ \Delta z_{id} \ \Delta z_{pi} \ \Delta z_{qi} \ \Delta V_{dci}] \\
 X_{WFci} &= [\Delta i_{di} \ \Delta i_{qi} \ \Delta V_{dcri} \ \Delta \theta_{off} \ \Delta z_V] \\
 X_{WF} &= [\Delta \omega_t]
 \end{aligned} \tag{4.20}$$

Simulink is implemented to assess the validity of the small-signal model described by (4.19). Results from the small-signal model are compared with those from the averaged model described in Section 4.8. The system stability is assessed by calculation of the eigenvalues of system (4.19).

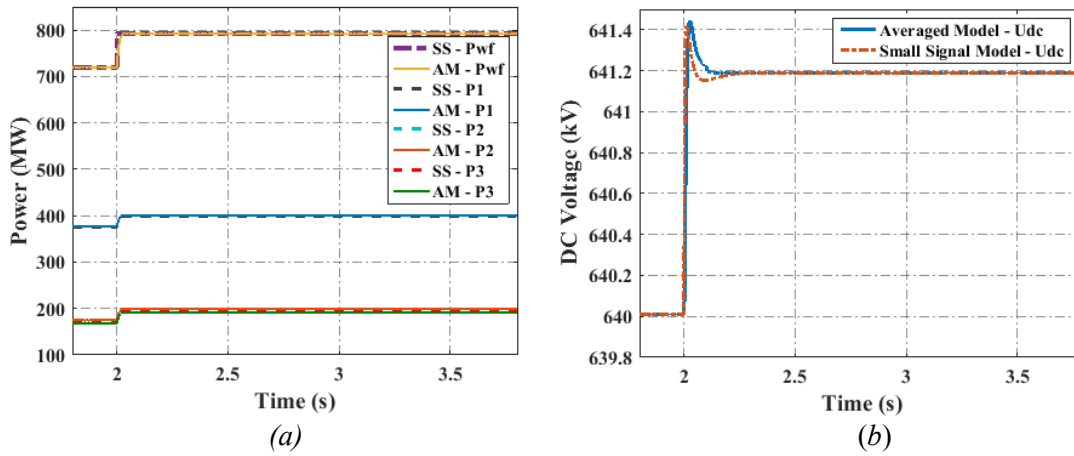


Figure 4.13: Response to 10% step increase in wind farm power output. Comparison of small signal model (SS) to averaged model (AM). (a) Power variation in OWF and Grids 1, 2 and 3. (b) DC voltage variation.

Figure 4.13 (a and b) shows the comparison of the small-signal and averaged models for a 10% step increase in power from the OWF. As it can be observed, the power variations in the different ac grids are similar for both models. With regards to dc voltage, it can be observed that the averaged model presents a faster response than its small-signal counterpart. The reason for this behaviour is due to the converters' inner control loops being modelled only in the small-signal model. However, it can be concluded that the overall dynamic performance agrees on well.

Figure 4.14 shows the system eigenvalues for parametric variations in droop gains k_{fv} and k_{pv} . As it can be observed in Figure 4.14(a), variations of k_{fv} from 30 to 65 kV/Hz do not affect the system eigenvalues (a close-up to the dominant eigenvalues is provided with the right-hand side plot); in other words, a variation in the frequency dead-band does not have an adverse effect in small-signal stability.

Conversely, Figure 4.14(b) shows the location of the eigenvalues as a function of droop constant k_{pv} in Grid 3, which has been modified from 0.005 to 0.15 MW/kV (i.e. from 10 to 300% of the original value). As it can be seen, the eigenvalues tend to exhibit a higher damping as k_{pv} increases. These results confirm that the system remains stable for a range of droop constants and, moreover, the frequency support schemes do not affect the normal operation of the system with proportional droop control.

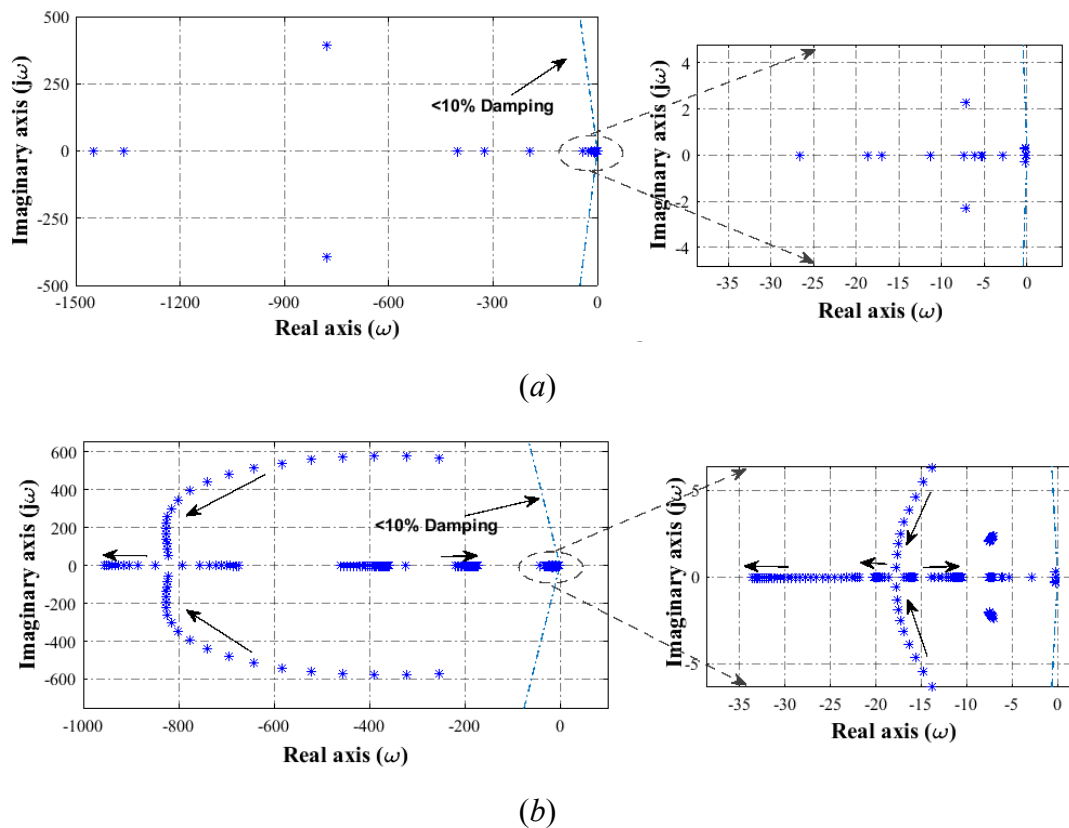


Figure 4.14: Small-signal stability study of the system. (a) Root locus of the system for variations in droop gain k_{fv} . (b) Root locus of the system for variations in droop gain k_{pv} . In both cases, a zoomed view of the dominant eigenvalues is given by the right-hand side plots.

4.10 Simulations and Analysis

In this section, the performance of the proposed ADC scheme is demonstrated. Two case studies are carried out. The fast frequency controllers are fitted with the proposed ADC scheme and with simulation results the effectiveness of the controls

are compared with the ADC, without the ADC scheme and when no frequency control (NC) is considered.

4.10.1 Case 1 – Single Imbalance

Figure 4.15 shows the results due to a generation loss of 1800 MW in Grid 2 at $t = 5$ s. With NC, there is no frequency support from the MTDC grid and the frequency in Grid 2 falls to 49.49 Hz (*i.e.* the frequency deviation is 0.51 Hz). When the ACC is in operation only, the responding ac systems (Grids 1 and 3) transferring additional power to the disturbed Grid 2 experience a drop of frequency (see Figure 4.15). When the frequency drop exceeds $\Delta f_{ab1} = 0.02$ Hz, the VSCs connected to Grids 1 and 3 enter the frequency sensitive mode. The dc voltage droop on all onshore converters is disabled and the dc grid voltage becomes unstable at $t = 8$ s (see solid red line in Figure 4.15). This loss in control of dc voltage impacts the OWF active power as well because of the presence of the V_{dc} - f droop. It should be noted that the issues here highlighted are still present without an OWF providing fast frequency support. The presence of a dc voltage limiter does not allow the dc voltage to exceed $V_{dc} \pm 10\%$.

With the proposed ADC present (denoted ACC+ADC), the converters connected to Grids 1 and 3 discriminate the frequency drop due to the provision of fast frequency support and change the set point from $\Delta f_{ab1} = 0.02$ Hz to $\Delta f_{ab2} = 0.1$ Hz. This operation prevents the VSCs connected to responding Grids 1 and 3 from entering the frequency sensitive mode. With the ADC fitted, the dc voltage becomes stable while fast frequency support is provided (see solid blue line in dc voltage graph in Figure 4.15). As it can be observed, the frequency drop has been reduced to 0.39 Hz when the ACC is used.

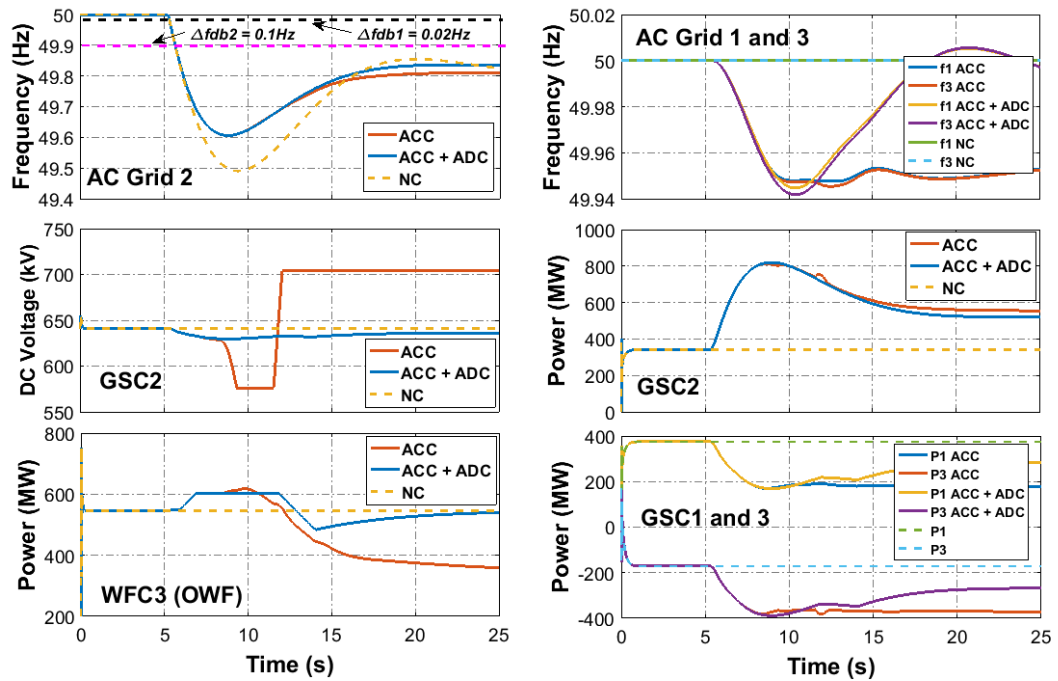


Figure 4.15: Case 1, ACC scheme. System response after a generation loss of 1800 MW in Grid 2.

Figure 4.16 shows the simulation results when the CC is employed, when the CC is upgraded with the ADC (denoted CC+ADC) and when no corrective actions are taken (NC). When the CC is employed only, the VSCs connected to responding Grids 1 and 3 activate their frequency support mode and disable the active power-dc voltage droop. This results in a rapid drop of power injected into Grid 2 (see solid red line in GSC2 power in Figure 4.16) and a further frequency drop on the disturbed grid at $t = 10$ s (see solid red line). With CC operating alone, there are unexpected power flows because of a maloperation or lack of coordination between the converters. For the case of CC+ADC, the sudden drop of power transferred to the disturbed Grid 2 is avoided by modifying the set-point of Δf_{ab} on GSCs 1 and 3 from $\Delta f_{ab1} = 0.02$ Hz to $\Delta f_{ab2} = 0.1$ Hz. As it can be observed, there is an additional frequency drop at $t = 14$ s but this is due to the recovery period of the WT.

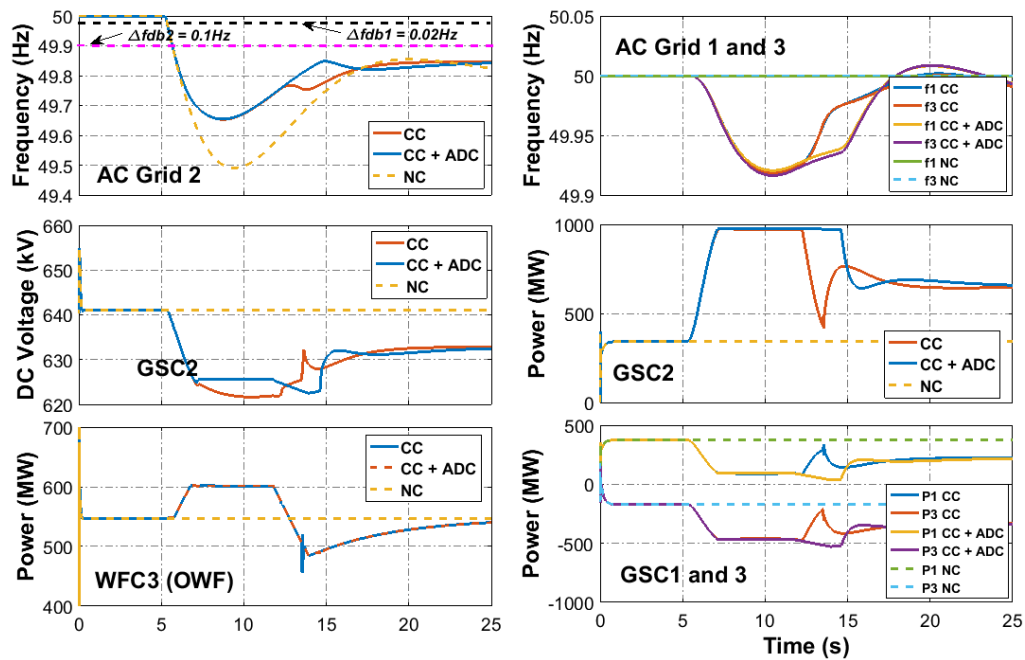


Figure 4.16: Case 1, CC scheme. System response after a generation loss of 1800 MW in Grid 2.

A comparison is also made when all converters use the DLC scheme only, when DLC is used with the proposed ADC (denoted DLC+ADC) and without a supplementary frequency control (NC). Figure 4.17 shows the simulation results. It can be observed that the DLC scheme employed on its own still maintains system stability and steady power flows. This occurs as the system has both power-voltage and frequency-voltage droops active in the disturbed operation. Given that the ADC delays the converters from switching to their frequency sensitive mode where the voltage droop is disabled, the ADC-upgraded DLC gives the same results as when the DLC is employed only. In other words, the ADC does not provide any benefits as with the DLC a voltage droop is always active both in normal and disturbed operation. Table 4.3 provides a comparison of the performance of the different frequency control schemes upon the opposing frequency events. The *RoCoFs* are also compared. As discussed in Chapter 3, the *RoCoF* is calculated as the average df/dt calculated for every 500ms sampling window in the first two seconds following the event.

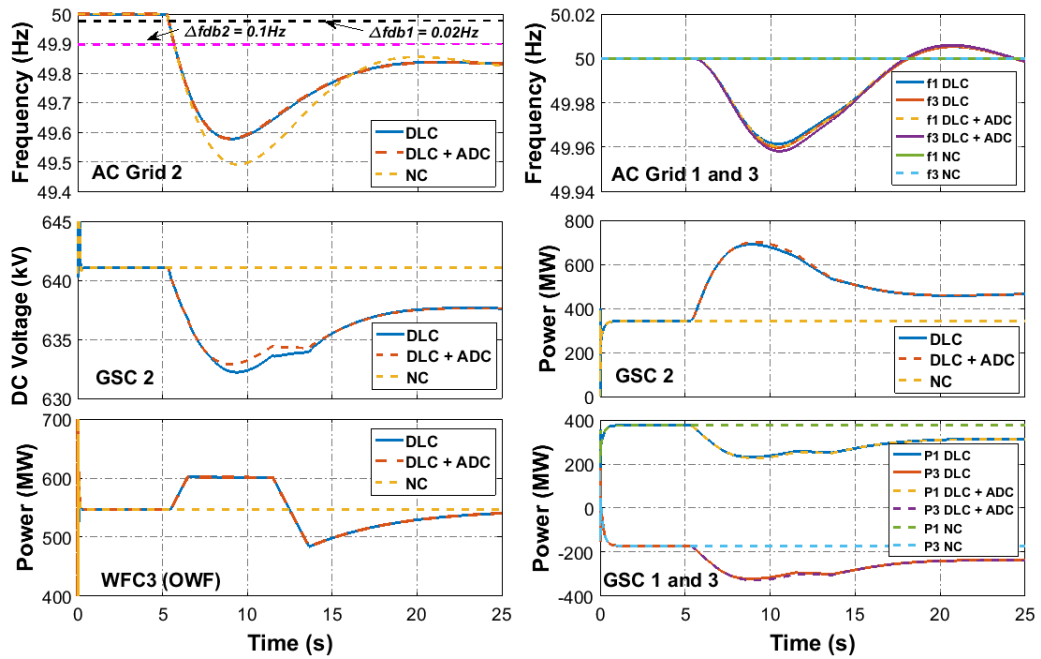


Figure 4.17: Case 1, DLC scheme. System response after a generation loss of 1800 MW in Grid 2.

Table 4.3: Frequency control schemes during single imbalance.

	NC	ACC	CC	DLC	ACC+ ADC	CC+ ADC	DLC+ ADC
Δf (Hz)	0.51	0.39	0.33	0.41	0.39	0.33	0.41
$RoCoF$ (Hz/s)	0.18	0.156	0.15	0.159	0.156	0.15	0.159
Stable?	Yes	No	Yes	Yes	Yes	Yes	Yes

4.10.2 Case 2 – Opposing Frequency Trends

The performance of the control schemes is demonstrated in this section for opposing frequency events (i.e. simultaneous loss of demand and generation). Simulations are performed when a generation loss of 1800 MW occurs in Grid 2 while a simultaneous demand loss of 900 MW occurs in Grid 3 at $t = 5$ s. The probability of these events occurring simultaneously in reality is low and, in any case, they may occur a few seconds after each other. However, having them occur simultaneously in simulations helps to stress the system and, this way, assess the capabilities of the proposed ADC scheme.

A comparison is made when all onshore converters use the ACC scheme only, when the ACC is upgraded with an ADC (ACC+ADC) and when no action is taken (NC), with results shown in Figure 4.18. When the ACC is used on its own, the dc voltage droop on the onshore converters is disabled when the frequency deviation exceeds $\Delta f_{ab1} = 0.02$ Hz. A sudden drop of dc voltage occurs around $t = 10$ s (see blue line on Figure 4.18) due to only the f - P droop operating on GSCs 1, 2 and 3 and no converter controlling the dc voltage. This is also seen to affect the power from the OWF. When the ADC scheme is included, GSC1 modifies its set-point from $\Delta f_{ab1} = 0.02$ Hz to $\Delta f_{ab2} = 0.1$ Hz. Therefore, GSC1 retains control of the dc voltage using a V_{dc} - P droop and restores the dc grid operation during the provision of fast frequency support (see red line on Figure 4.18).

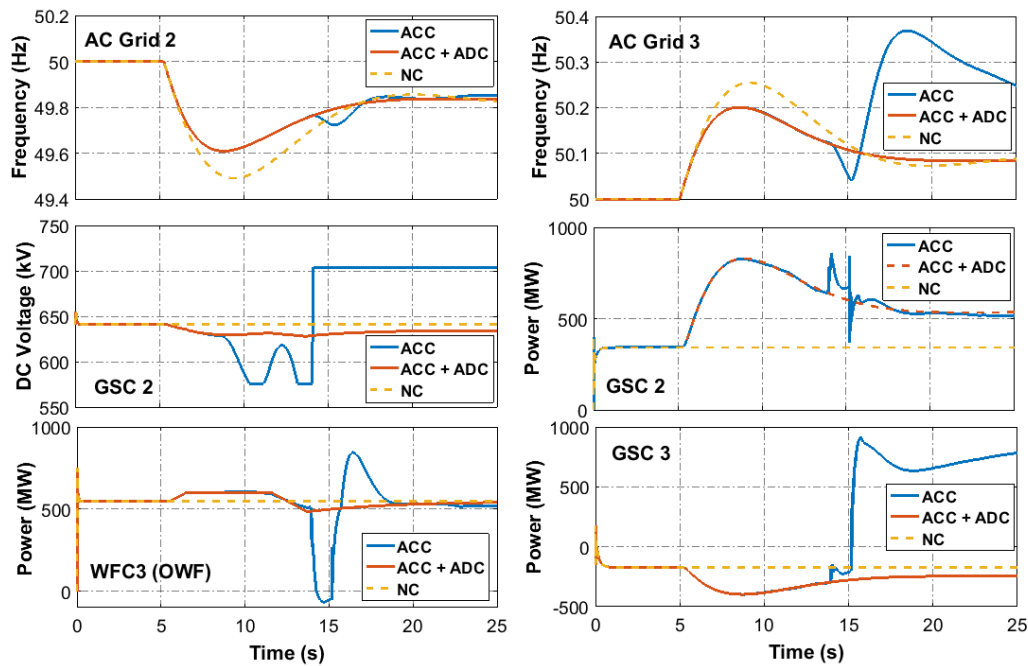


Figure 4.18: Case 2, ACC scheme. System response after a generation loss of 1800 MW in Grid 2 and 900 MW demand loss at Grid 3.

Figure 4.19 shows simulation results when the CC is used on its own, when the CC is upgraded with an ADC (CC+ADC) and with no frequency control (NC). When CC is used only, all VSCs initiate the fast frequency controls, disable their active power-voltage droop and enable their f - V_{dc} droops. Therefore, no converter

regulates active power in the MTDC grid. There are frequency oscillations in the ac grids as a result of power oscillations from the GSCs (see blue lines in Figure 4.19). Also, as a result of these frequency oscillations, the OWF temporary overproduction translates the dc voltage change at $t \approx 12.5$ s as a command to provide extra power again. For the case of CC+ADC, the ADC scheme allows the GSC1 to modify its set-point from $\Delta f_{ab1} = 0.02$ Hz to $\Delta f_{ab2} = 0.1$ Hz. As a result, operation of the power-voltage droop in GSC1 is maintained. This enables continuous stable dc voltage control, active power flow and frequency stability to the MTDC system (see solid red line in Figure 4.19).

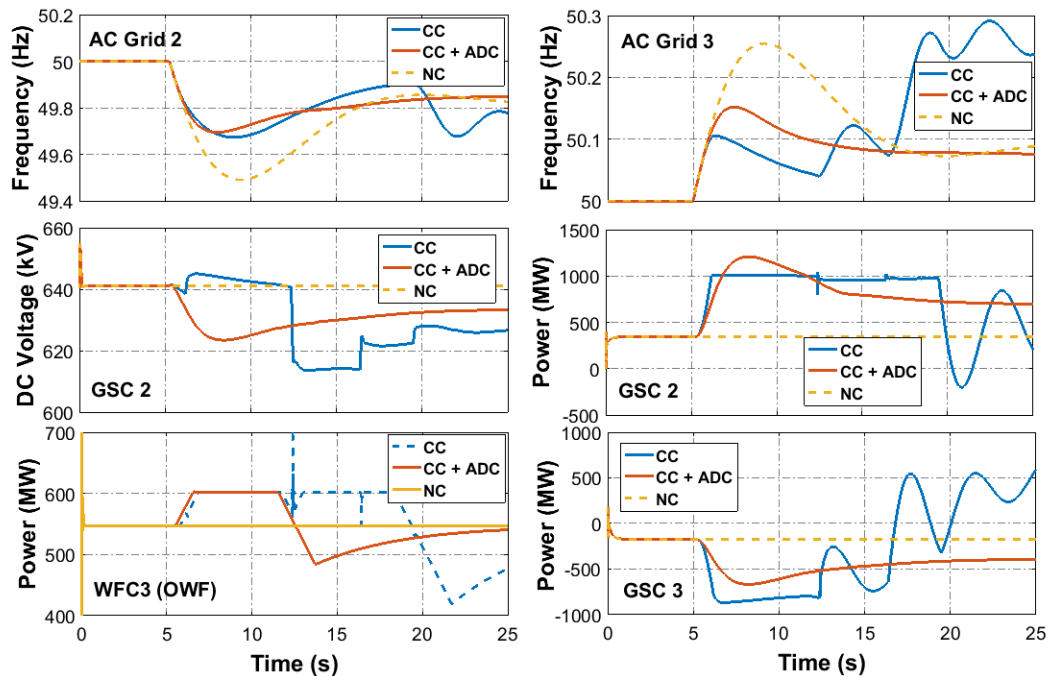


Figure 4.19: Case 2, CC Scheme. System response after a generation loss of 1800 MW in Grid 2 and 900 MW demand loss in Grid 3.

Figure 4.20 shows the simulation results when DLC is used on its own, when used with the ADC (DLC+ADC) and with no frequency control (NC). As in Case 1, the DLC gives the same frequency response with and without the ADC, with power flow and dc voltage remaining stable. A comparison of the performance of the different frequency control schemes upon the opposing frequency events is provided in Table 4.4.

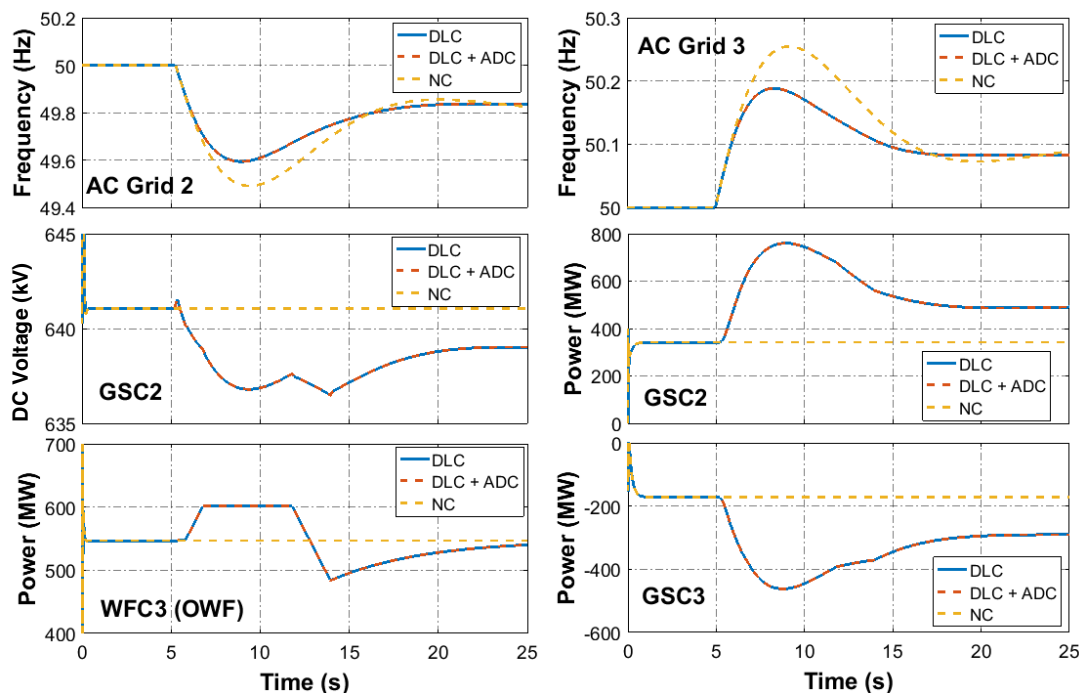


Figure 4.20: Case 2. DLC scheme. System response after a generation loss of 1800 MW in Grid 2 and 900 MW demand loss at Grid 3.

Table 4.4: Comparison of support schemes during multiple imbalances.

	ACC	CC	DLC	NC	ACC+ ADC	CC+ ADC	DLC +ADC
Multiple Imbalance (Opposing Frequency Trend)							
Δf (Hz)	0.39	0.35	0.41	0.51	0.39	0.33	0.41
$RoCoF$ (Hz/s)	0.156	0.143	0.159	0.18	0.156	0.141	0.159
Stable?	No	No	Yes	Yes	Yes	Yes	Yes

4.11 Fast Frequency Controllers with Proposed ADC Scheme

In this section, all schemes (CC, ACC and DLC) are upgraded with the proposed ADC and their effectiveness is compared when multiple grid disturbances occur (a generation loss of 1800 MW in Grid 2 and a demand loss of 900 MW in Grid 3 at $t = 2$ s). Simulation results are shown in Figure 4.21 for the case of DLC only, DLC+ADC, CC+ADC, ACC+ADC and when no corrective action is taken (NC).

An improved ac grid frequency deviation and $RoCoF$ are achieved in all three schemes. The CC+ADC scheme (solid blue line) provides the most frequency support followed by the ACC+ADC scheme (solid red line). The DLC+ADC

scheme provides the least frequency support because its $P-V_{dc}$ and $f-V_{dc}$ droops operate simultaneously. However, this combined voltage and frequency droop operation in the DLC scheme allows for the continuous control of dc voltage during the provision of frequency support, therefore the DLC does not need the ADC to ensure continuous stable operation. A droop correction factor has been suggested to overcome the limited support capability of the DLC, but this requires fast communications [27].

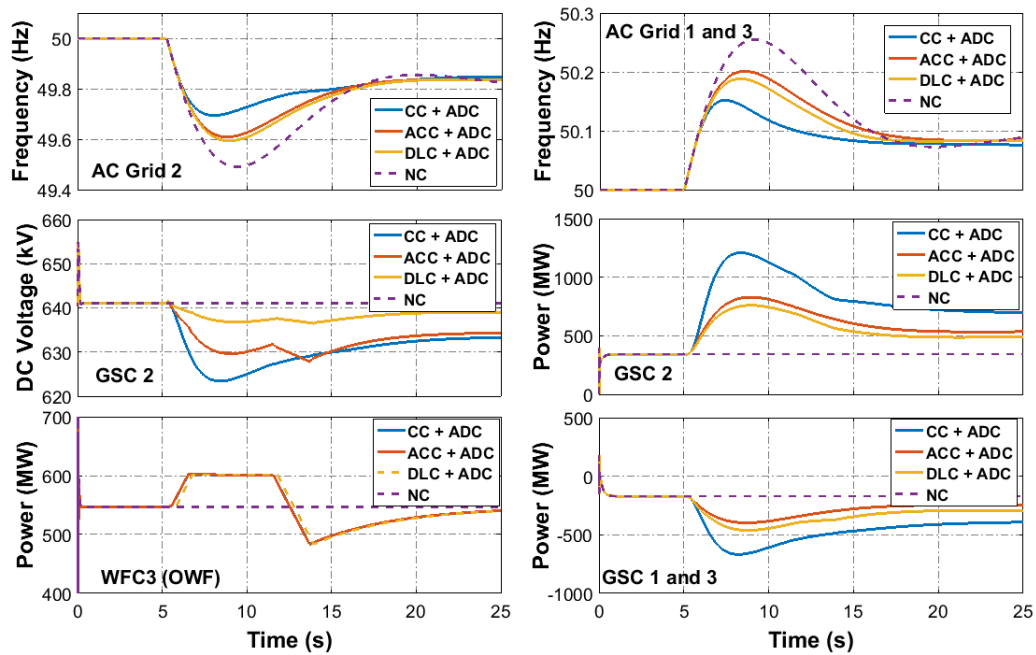


Figure 4.21: Comparison of all schemes. System response after a generation loss of 1800 MW in Grid 2 and 900 MW demand loss at Grid 3.

4.12 DC Grids with Different Frequency Control Modes

An additional study was carried out to investigate MTDC frequency support when each onshore VSC operates with a different frequency control scheme. Table 4.6 shows the supplementary control strategy used for each converter.

Table 4.5: Control modes of the converters.

Converter	Supplementary Frequency Control
GSC1	CC +ADC
GSC2	ACC +ADC
GSC3	ACC+ADC
WFC3	$V_{dc}-f$

Figure 4.22 shows simulation results due to a generation loss of 1800 MW in Grid 2 at $t = 5$ s. To show the benefits of the proposed ADC scheme, the performance is compared to the case when CC is employed only in GSC1 and ACC only in GSC2 and GSC3 (without ADC support). When the ADC is included, a stable dc voltage can be observed (see red line on Figure 4.22(c)) as opposed to the case when CC and ACC are used on their own (see blue line on Figure 4.22(c)). The proposed ADC scheme avoids a sudden drop of power transferred through GSC1 and GSC3 (see Figure 4.22(e)-(f)).

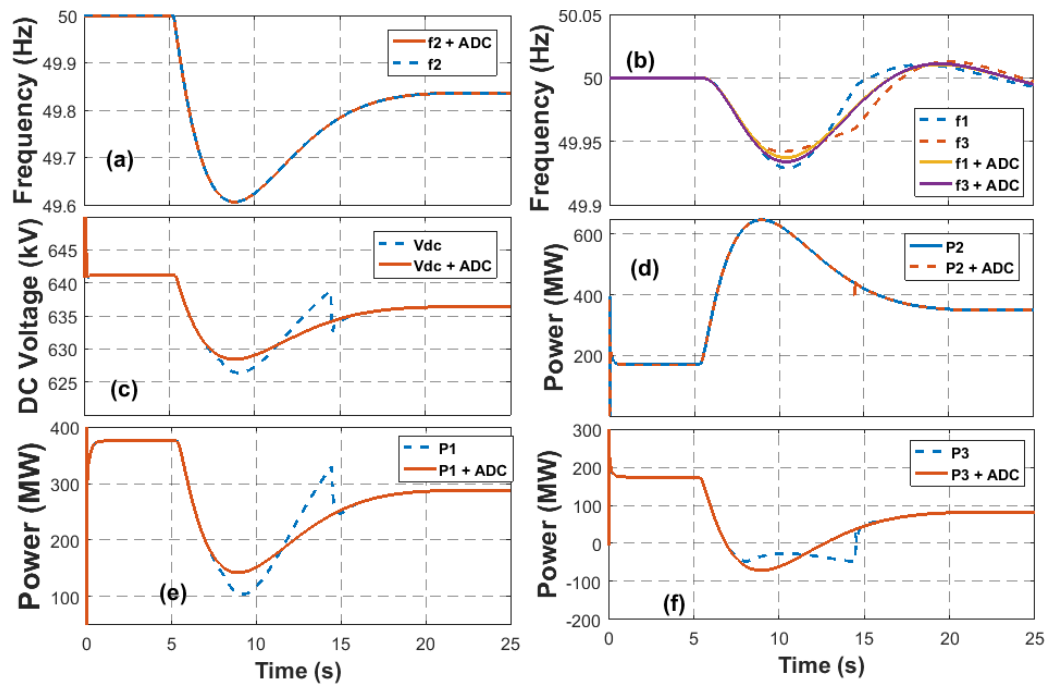


Figure 4.22: Effect of the ADC scheme on different control modes in an MTDC system. Frequency variations in: (a) Grid 2; (b) Grids 1 and 3. (c) DC voltage variation. Power injections in (d) VSC2; (e) Grid 1; (f) Grid 3

4.13 Summary

In this chapter, a 4-terminal dc grid was introduced and modelled. Its small signal stability study was also carried out and compared against time domain simulations for validation. It is shown that the frequency droop and dead-band do not affect the small-signal stability of the studied system. Results show that the ADC improves the coordination of frequency support of the MTDC system and the OWF.

The effectiveness of three main frequency support schemes which can be embedded into the MTDC grid controls has been assessed. As examined in this work, an unstable dc grid operation and reduced power transfer may result from frequency variations on the different ac systems connected to the dc grid during the provision of frequency support. This also affects the capability of the connected OWF in providing synthetic inertia support.

To address these issues, an ADC has been proposed and fitted to the frequency support schemes. With dead-bands, how much the VSC controls should interact with the frequency changes can be determined. It has been shown through simulations which were performed in MATLAB/Simulink that the inclusion of the ADC helps to restore a stable operation and to improve active power transfer during multiple frequency oscillations on the interconnected ac grids. The ADC scheme allows a VSC to discriminate the location of the frequency disturbance and to modify the dead-band set-point of its own frequency control algorithm. Among the studied strategies, the CC scheme when upgraded with the ADC achieved the best performance, followed by the ACC scheme fitted with the ADC and then by the DLC scheme. It should be emphasised that the DLC may not need the ADC as its voltage droop is always active.

Chapter 5

Experimental Validation of Fast Frequency Support from MTDC Grids

5.1 Introduction

In this chapter, an experimental platform is introduced and used to validate the fast frequency controls introduced in Chapter 4. The three-machine GB system introduced in Chapter 3 is used in the studies in this chapter.

The experimental platform consists of an RTDS, a dc network cabinet, a three-terminal VSC test rig, a dSPACE controller and a grid simulator (GS). The three-machine GB system is modelled in the RTDS using RSCAD, its simulation interface. A meshed MTDC grid is represented by the three-terminal VSC-HVDC test rig which is controlled via the dSPACE computer. The dSPACE and RTDS models are then interconnected by the GS, forming a HiL experimental setup. Similarly, in PSCAD, the three-machine GB system connected to a three-terminal VSC-HVDC grid is also modelled.

The experiments consider fast frequency support coordination between different onshore ac grids interconnected by an MTDC grid. The fast frequency controls and the ADC are modelled and experiments on frequency support from the MTDC grid to the three-machine ac system are carried out, with and without the supplementary controls introduced in Chapter 4. The aim of this chapter is to show experimentally that the fast frequency controls work in a more realistic setting. Also, it aims to show the system behaviour with and without the ADC fitted to the converters. With the experiment, it can be shown that the ADC can discriminate between a troubled and responding ac grid. It also enables frequency support to be possible when multiple converters are installed with fast frequency controllers. Finally, a comparison between the experimental and simulation results is made.

5.2 Description of Experimental Platform

The experimental platform enables a real-time demonstration and validation of different ancillary services that can be implemented in an MTDC scheme be it for frequency support, fault-ride through or fault protection. To understand the experimental platform and its operation, its individual units are first described in this section. Figure 5.1 shows an illustration of the experimental setup. It consists

of three VSCs, one dSPACE computer, one dc network cabinet, one GS and one RTDS.

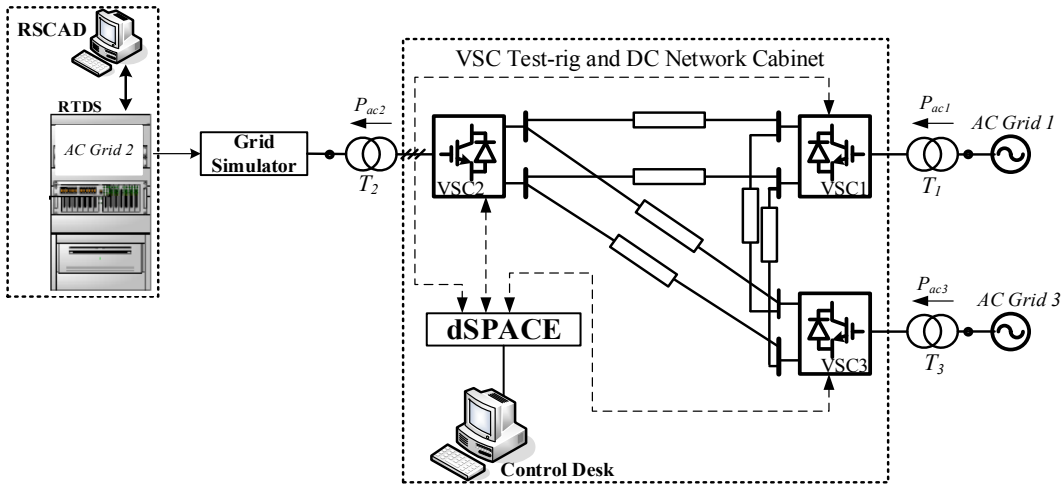


Figure 5.1: Illustrative diagram of experimental test rig

5.2.1 VSC-HVDC Test Rig

This test rig consists of three two-level VSCs with a rated capacity of 2 kW each, an embedded computer (dSPACE), three transformers and ac and dc inductors. The rated voltage of the VSCs is 140 V_{L-L} rms ac and 250 V dc. VSCs 1 and 3 are powered by the main grid via two 400 / 140 V autotransformers. VSC2 however, is powered via an isolation transformer connected to the grid simulator which controls its voltage to 140 V_{L-L} as well.

The dSPACE DS 1005 performs data acquisition, monitoring and controlling of each VSC. Digital and analogue signals are transmitted back and forth between the dSPACE and the RTDS through the interface board [139]. Its control desk uses a Simulink interface. AC grids can also be modelled in this Simulink interface and directly controlled by the dSPACE.

5.2.2 DC Network Cabinet

The dc network cabinet shown in Figure 5.2(a) represents the dc cable models which can be used to form the dc grid. It consists of a scaled down representation of dc cable circuits, dc short circuit generator and an IGBT-controlled variable resistor [140]. The interior of the VSC cabinet is shown in Figure 5.2(b). The specifications of the VSC-HVDC test rig and dc network cabinet are provided in

Appendix III. In this experiment, a meshed dc network is formed as in Figure 5.1 and the dc cables in the MTDC grid are represented using resistors and dc inductors.

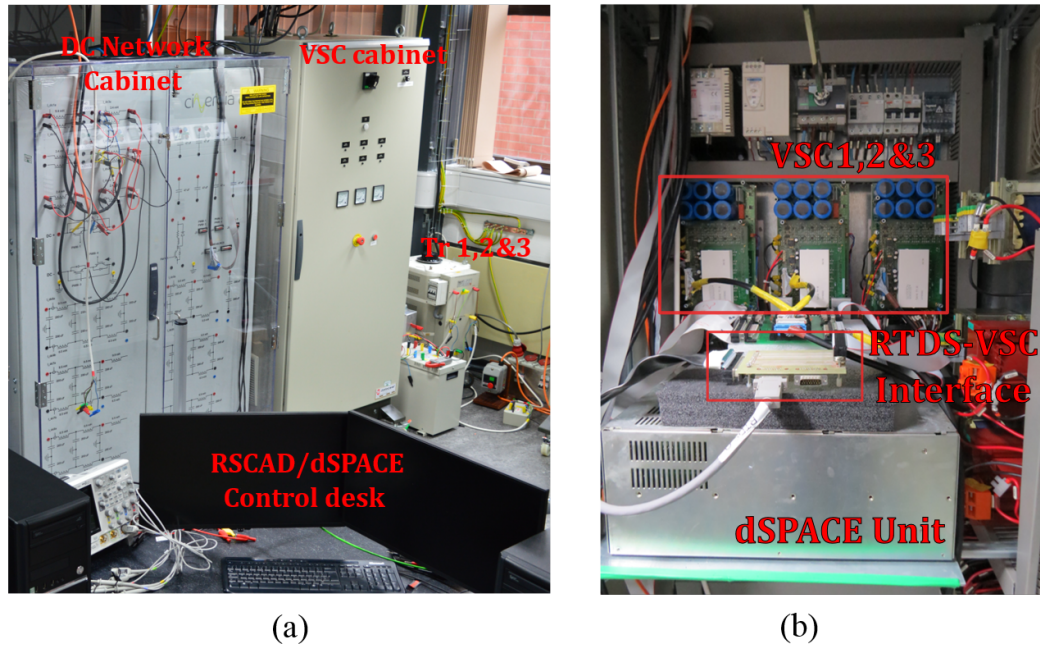


Figure 5.2: VSC experimental test rig set-up: (a) DC network cabinet, VSC 1,2 & 3 cabinet; Transformers 1,2 & 3 and dSPACE control desk (b) Interior of VSC cabinet and dSPACE unit.

5.2.3 AC Grid Simulator

The GS, shown in Figure 5.3(a), serves as the interface between the RTDS and the VSC test rig. It is a four-quadrant power amplifier rated 2 kVA and 270 V_{L-G} rms. The amplifier absorbs the power from the VSC2 and injects it back to the laboratory supply. The GS receives a low voltage signal from the analogue output cards (GTAO) of the RTDS. With this, it produces a three-phase mains supply voltage of 140 V. This three-phase supply voltage is the input voltage of the isolation transformer connected to VSC2 of the VSC test rig. Therefore, 140 V in the test rig is equivalent to 400 kV in the RTDS. This is the forward path between the RTDS and VSC test rig. Finally, a three-phase current measurement from the test rig is fed back to the RTDS via its analogue input cards (GTAI). This closes the loop between the RTDS and VSC test rig [139], [141].

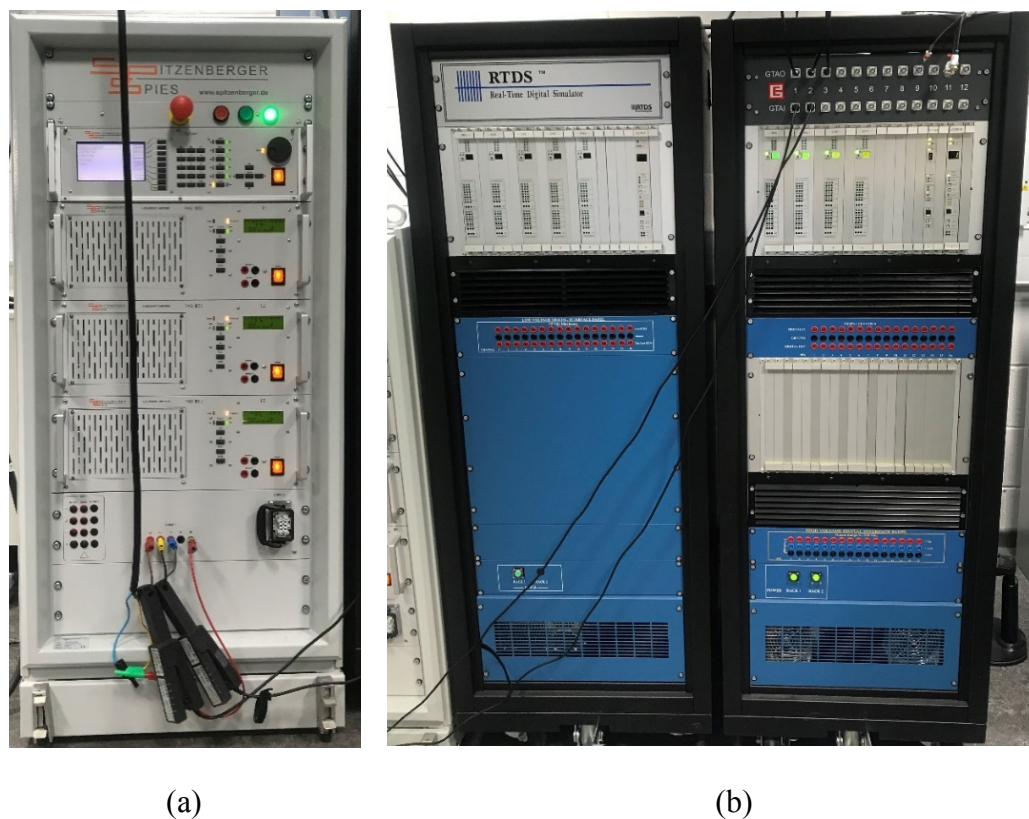


Figure 5.3: Real-time system setup: (a) AC Grid Simulator; (b) RTDS.

5.2.4 Real Time Digital Simulator

The RTDS, shown in Figure 5.3(b), is used for performing real-time power system simulations. The RSCAD software is used to build power system models for the RTDS. The 400 kV 3-machine GB power system was modelled with RSCAD and a node voltage measurement of this ac system is scaled down and transformed to an analogue output signal via the GTA0 of the RTDS firmware. This analogue output signal is exported to the GS. The RTDS also receives analogue current measurements from the GS through the GTAI of the RTDS firmware. This current measurement is scaled up and is represented in the simulator as a current source connected to the same node.

The components of the experimental rig discussed above were pre-existing in the Cardiff University HVDC laboratory. During this PhD, the three-machine GB system had to be newly modelled into the RSCAD platform for its use in frequency response. Also, the ADC system was newly modelled. They are discussed in the following sections.

5.3 RSCAD Modelling

The initial step in carrying out this experimental validation was modelling the ac system in RSCAD. The three-machine GB system with same parameters described in Chapter 3, shown in Figure 5.4, was modelled in RSCAD and compared against the PSCAD model to confirm their frequency response was similar. The two models were tested for a sudden loss of generation of 1320 MW and the response is shown in Figure 5.5.

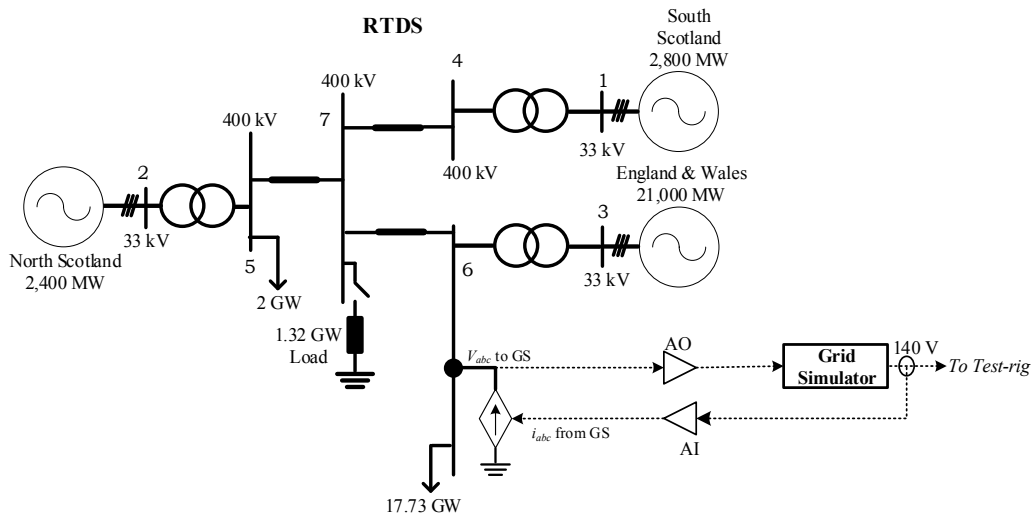


Figure 5.4 : Three-machine GB system

As it can be observed in Figure 5.5(b), the frequency response of both systems is very similar showing agreement in their frequency behaviour without the MTDC connected to them. Also, the inertial response (i.e. instantaneous increase in power due to frequency event) from the synchronous generators of both RSCAD and PSCAD models, shown in Figure 5.5(a), gives some similarities in amplitude but the oscillations from both models are different. This is assumed to be so because of the differences in generator modelling in both PSCAD and RSCAD. Based on these results, hardware-in-the-loop tests were now carried out to demonstrate the fast frequency control schemes effectiveness. These are shown in the following sections.

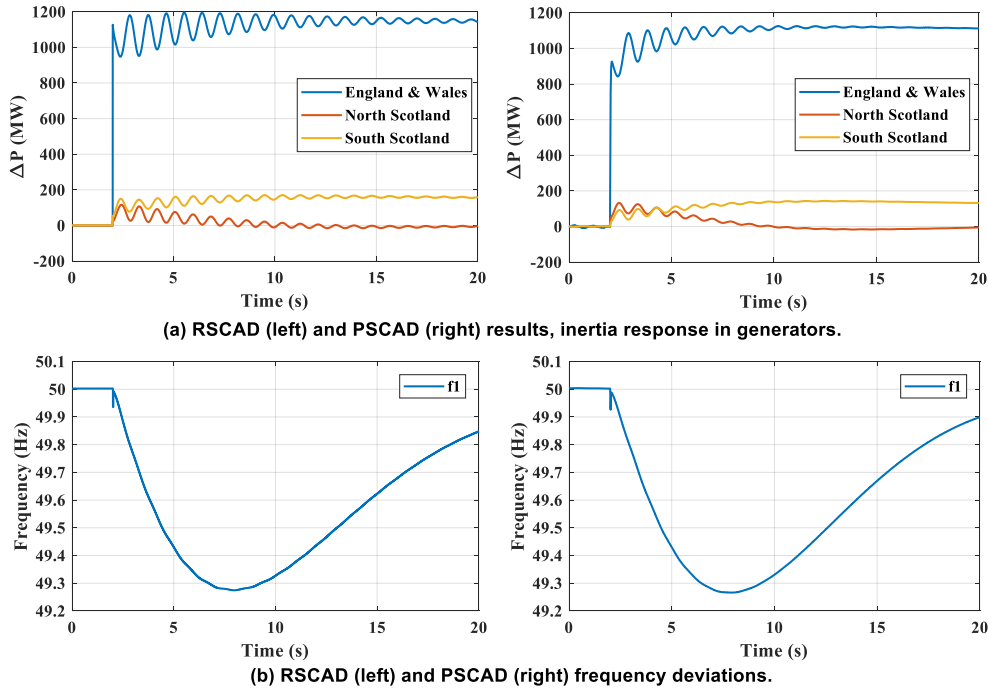


Figure 5.5: Three-machine GB system: Comparison of PSCAD results vs RSCAD results.

5.4 Master-Slave Control

The master-slave control is used to initialise the experimental system control. In this scheme, the dc voltage is regulated by only one converter station (in constant voltage control mode). This converter station is called the master terminal. The other converter stations (slave terminals) regulate the power, i.e. in constant power mode. The master terminal is responsible for maintaining the stable operation of the entire grid. If there is an outage of that terminal, the dc voltage control would be lost, leading to the entire grid loss. For this reason, the master-slave control's main drawback is reliability [125]. The master and slave terminals are shown in Figure 5. 6 and Figure 5. 7 respectively. The phase-locked loop (PLL) synchronizes the converter to the point of common coupling (PCC) voltage and provides the reference angle for the VSC [128], [130]. The three phase currents and voltages are measured at the PCC and via Park Transformation are converted to dq components, v_{dq} and i_{dq} [31].

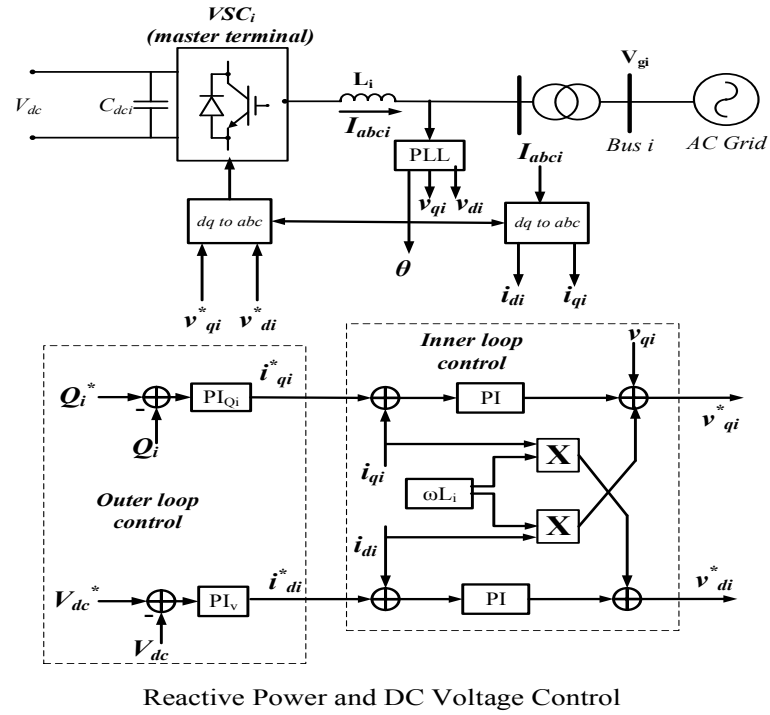


Figure 5. 6: Master-slave control - master terminal.

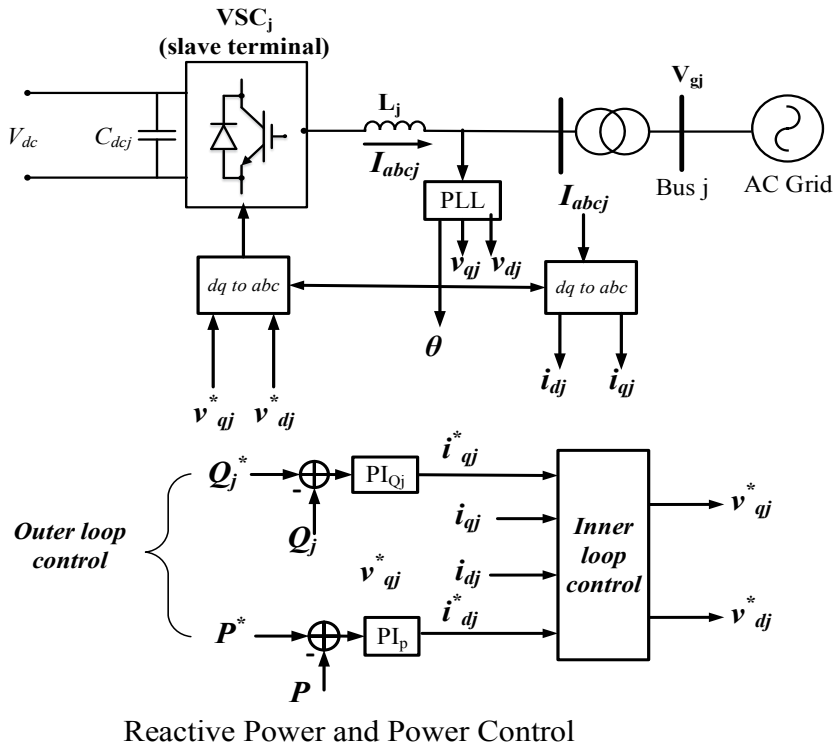


Figure 5. 7: Master-slave control - slave terminal.

5.5 Experimental System Setup

Figure 5.8 shows the setup of the experimental platform to validate the fast frequency control schemes. AC Grids 1 and 3 are modelled in the Simulink interface of the dSPACE control desk. They are represented as simplified models with a base load capacity of 40 GW, while AC Grid 2 is the three-machine GB system which has been modelled in RSCAD (as discussed in section 5.3). The voltage at the selected node of the three-machine system is converted to an analogue signal and passed to the GS, which produced a 140 V AC which is input to transformer 2 connected to VSC2 of the test rig.

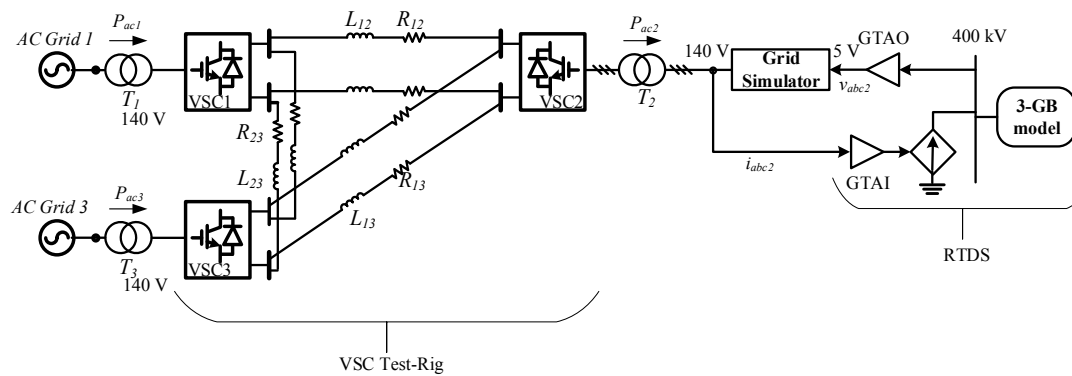


Figure 5.8: Real-time HiL implementation

Figure 5.9(a) shows the transformation process from the RTDS node voltage to the test rig voltage. With the aid of the GS, the 400 kV of the RTDS is seen as a 140 V ac voltage at the VSC test rig, i.e. a 400 kV/140 V transformation is achieved. Also, as shown in Figure 5.9(b), the current from the VSC converter is transmitted to the RTDS through the GTAI and a phase compensator is also implemented to remove the transmission delay of the VSC2 current [139].

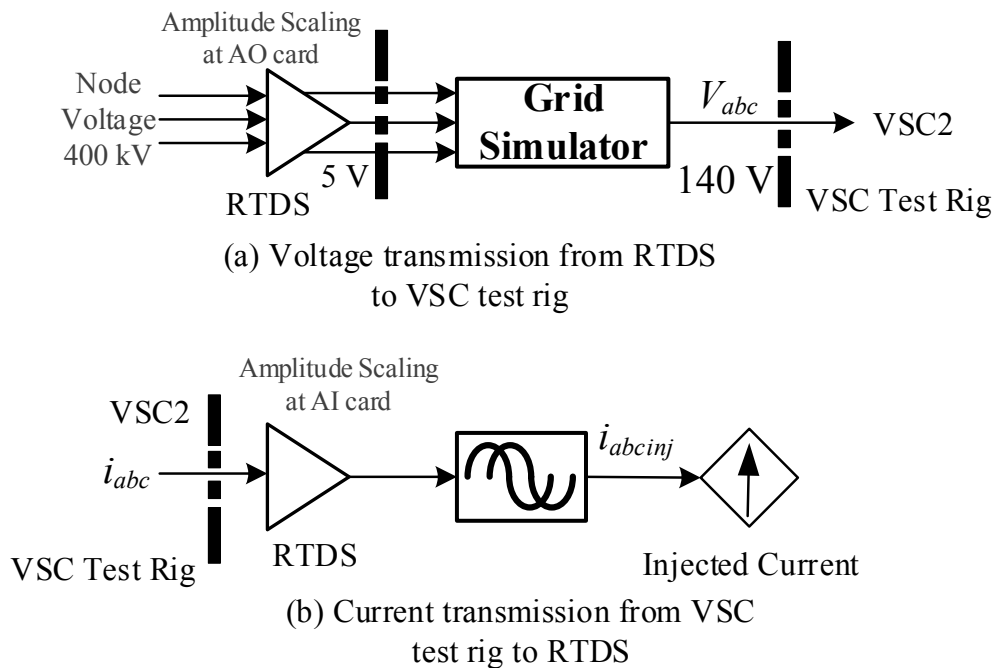


Figure 5.9: Signal transmission between RTDS and VSC Test-rig

On start-up, the three VSCs are operated initially in master-slave mode. VSC1 is in dc voltage and reactive power control mode (i.e. master), while VSC2 and VSC3 were operated in active power and reactive power control mode (slave). In steady-state, droop control is achieved by switching the slave converters first into droop (V_{dc} - P droop) and then the master converter is finally switched to droop i.e. P - V_{dc} droop. VSCs 1 and 3 export power into the dc grid, while VSC2 imports power from the dc grid into the Grid 2. Throughout this chapter, a negative sign indicates power flowing into the dc grid while a positive sign indicates power flowing out of the dc grid. The power flow direction is also indicated in Figure 5.8. The VSC test rig and dc line parameters as used in this study are shown in Appendix IV.

After setup of the MTDC RT-HiL system, its primary function of power transfer among the converters and ac grids is tested. At 0.8 s, the power set-point of VSC2 was changed from 0.2 p.u. to 0.6 p.u. The results are shown in Figure 5.10. The dc voltage is seen to reduce by about 0.02 p.u as shown in Figure 5.10(a). Also, as droop control is being used here, the change in power set-point of VSC2 also changes the power set-points of all converters. In master-slave control, when the power set-point of a slave converter is changed, the power of that slave converter

and the master converter only change. However, with droop control, there is a power sharing between all converters. Because the MTDC system is connected to the three-machine GB ac system, there is an increase in power flowing into it from VSC2. This leads to an increase in the system frequency and the generator reducing its output power, causing the line current to also reduce.

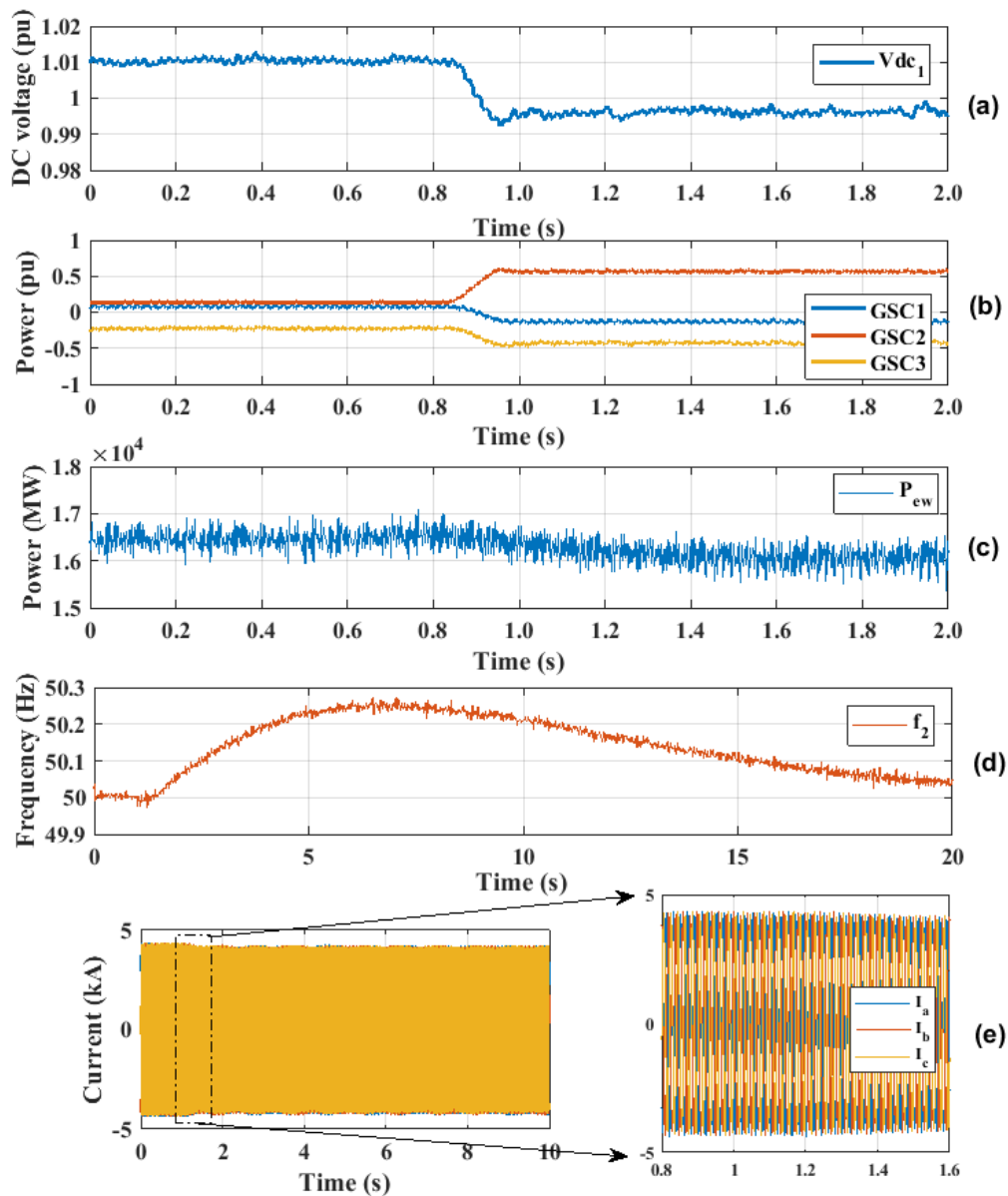


Figure 5.10: System response in VSC2 power setpoint change (a) DC Voltage variation (b) Power flow in converters (c) England & Wales generator power (d) AC grid 2 frequency (e) AC grid current.

Table 5.1: Control mode of the converters

	Start up	Steady-state	ACC	DLC
VSC1	Constant V_{dc} & Q Control	P - V_{dc} droop	f - V_{dc} droop	P - V_{dc} & f - V_{dc} droop
VSC2	Constant P & Q control	V_{dc} - P droop	f - P droop	V_{dc} - P & f - P droop
VSC3	Constant P & Q control	V_{dc} - P droop	f - P droop	V_{dc} - P & f - P droop

For a generation loss of 1320 MW at 2s in AC grid 2 (i.e. three-machine GB system), the following tests were carried out:

- No fast frequency support or no control (NC)
- Fast frequency support with supplementary ACC scheme only in VSC2.
- Fast frequency support with supplementary DLC scheme only in VSC2.
- Supplementary ACC scheme fitted in all converters.
- Supplementary DLC scheme fitted in all converters.

5.7.1 No Control

A loss of generation or increase in demand of 1320 MW is represented in the system by the addition of a sudden load in the AC grid 2. This causes the system frequency to drop. Since there is no fast frequency support from the MTDC scheme, the dc voltage and power of the VSC test-rig do not change during the frequency imbalance event, as shown in Figure 5.12(a) and (b). This is because the systems are decoupled from each other.

The system frequency, shown in Figure 5.12(c), drops to 49.28 Hz i.e. a frequency deviation $\Delta f = 0.72$ Hz. The other ac systems do not have a change in their frequencies because they are decoupled and there is no control system to inform them to provide frequency support.

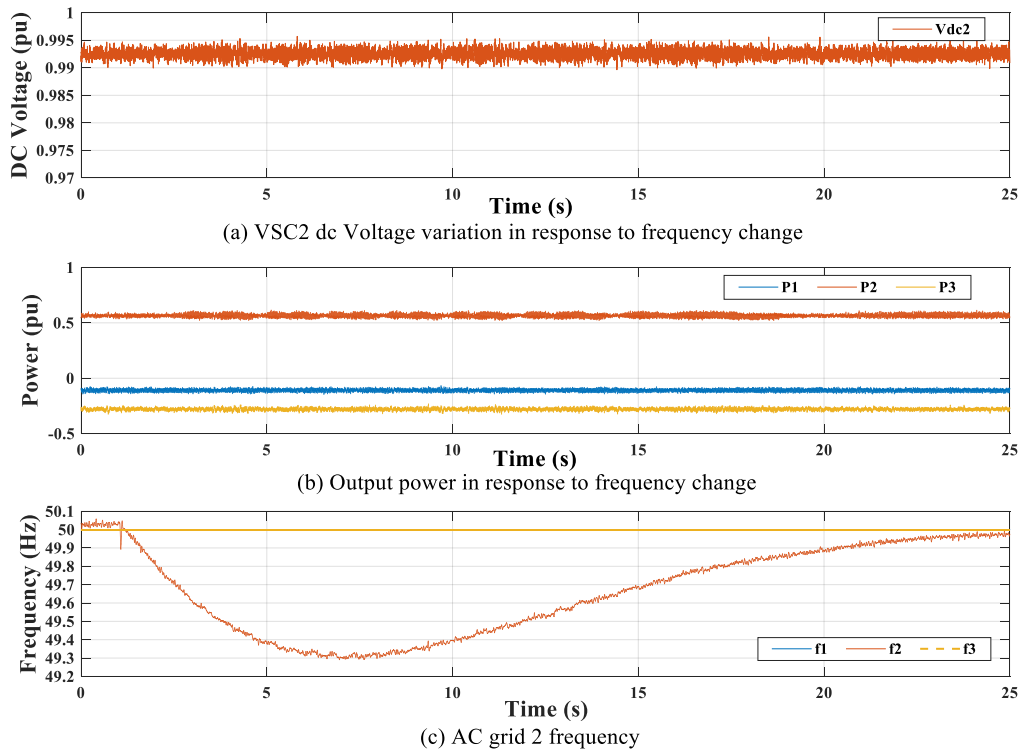


Figure 5.12: Experimental results: System response after loss of 1320 MW (No Control).

5.7.2 ACC scheme fitted in VSC2 only

In the ACC scheme, during normal operation the $V_{dc}-P$ droop is active, however when a frequency event occurs, $V_{dc}-P$ droop is deactivated while the $f-P$ droop takes over (see Chapter 4 for more information). Figure 5.13 shows the results from the test with ACC scheme fitted only in VSC2.

In response to the supplementary f-P droop, it can be seen in Figure 5.13(b) that the VSCs 1 and 3 provide extra power to VSC2 connected to the three-machine model (where the frequency event occurred). There is a frequency deviation of about 0.43 Hz and about 0.5 pu extra power is delivered to VSC2, as shown in Figure 5.13(c). The frequency of the other two grids drops to 49.91 Hz.

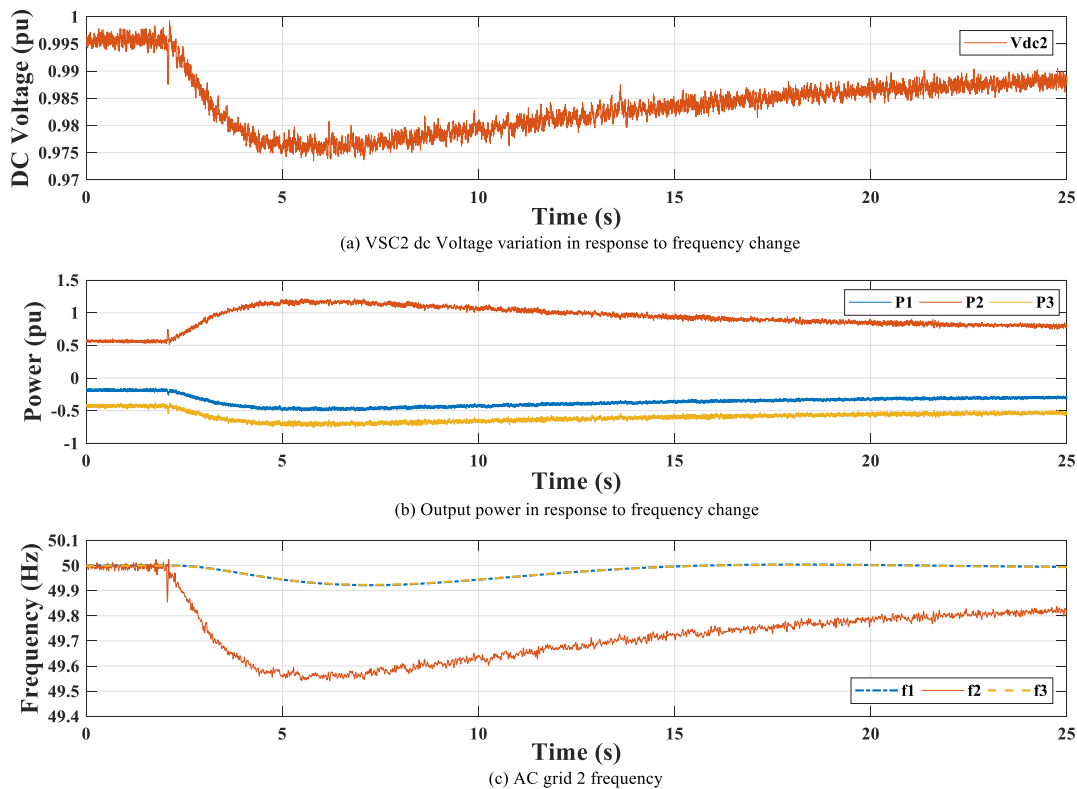


Figure 5.13: Experimental results: System response after loss of 1320 MW (ACC FS fitted in VSC2 only).

5.7.3 DLC scheme fitted in VSC2 only

In the DLC scheme, the system is operating in $P-V_{dc}$ droop during normal conditions, however when a frequency event occurs, the $f-P$ droop is activated and the $P-V_{dc}$ droop remains active unlike in the ACC scheme (see Chapter 4 for more information). Figure 5.14 shows the system response with the DLC scheme fitted in VSC2 only. The frequency (shown in Figure 5.14(c)) drops to 49.53 Hz (i.e. a frequency deviation of 0.47 Hz) which shows the reduced effectiveness of the DLC scheme compared to the ACC scheme due to its droops operating simultaneously.

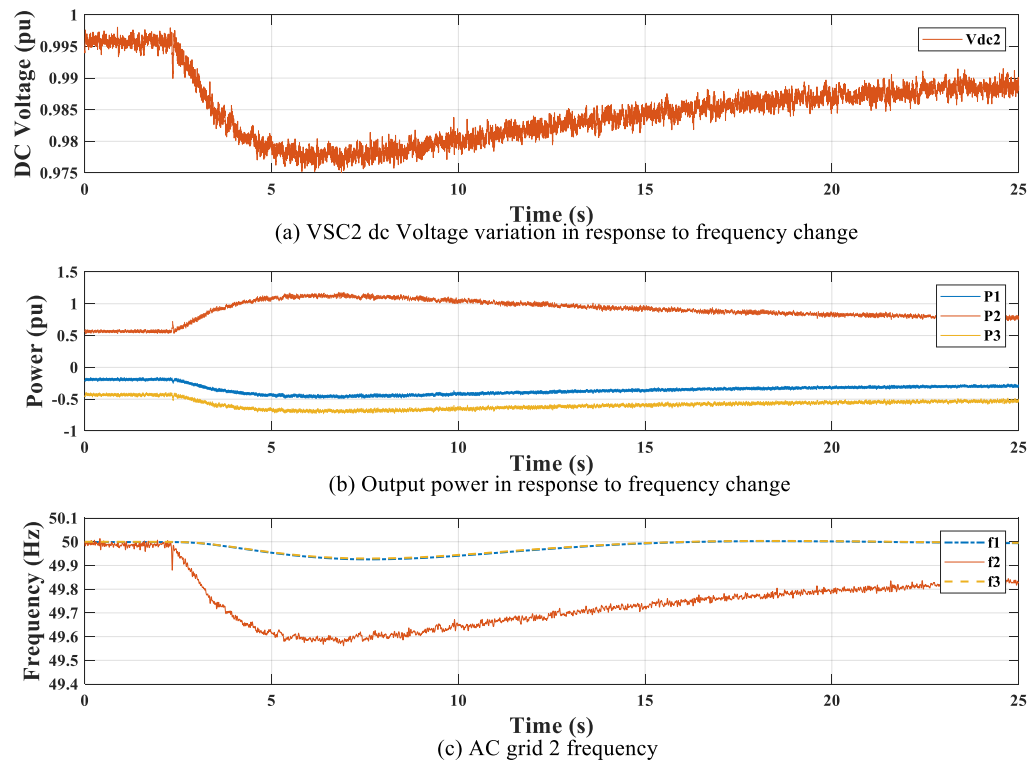


Figure 5.14: Experimental results: System response after loss of 1320 MW (DLC FS fitted in VSC2 only).

5.7.4 ACC scheme fitted in all converters

The experimental results when the ACC scheme fitted in all converters is shown in Figure 5.15, the dc voltage (shown in Figure 5.15 (a)) suddenly changes at 4 s and at 12.5 s causing the power flows from VSC1 and 3 to change as well. This is due to the frequencies of AC grids 1 and 3 dropping below 0.02 Hz, thus activating the frequency sensitive mode of their converter controls. When this occurs, the V_{dc} - P droop is deactivated and only the f - P droop is active. As discussed in chapter 4, the supplementary frequency controller is fitted in all converters in to enable the MTDC grid provide frequency support to any disturbed ac grid. However, this sudden change in power and dc voltage due to the other ac grids switching to frequency sensitive modes is undesirable for the operation of the MTDC grid. The frequency deviation at ac grid 2, Δf_2 is 0.43 Hz, as shown in Figure 5.15(c).

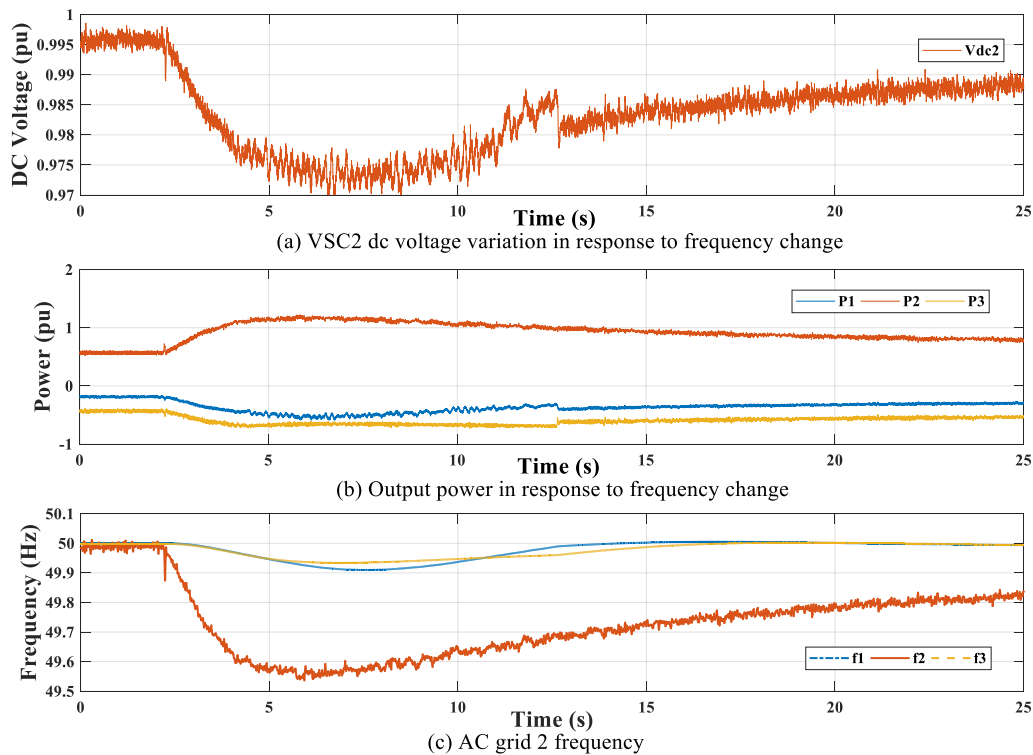


Figure 5.15: Experimental results: System response after loss of 1320 MW (ACC FS fitted in all converters)

5.7.5 DLC scheme fitted in all converters

Figure 5.16 shows the system response when DLC scheme is fitted in all converters. In this scenario, there are no power oscillations like when the ACC scheme is fitted in all converters. This, as discussed in Chapter 4, is because of the f - P and V_{dc} - P droops operating simultaneously. Since the V_{dc} - P droop is still active, a converter is still available to provide dc voltage control despite the grids 1 and 3 entering frequency sensitive mode. The DLC scheme does not need the ADC because of this property. The results are very similar for when DLC is fitted in all converters and when it is only fitted in VSC2 with a Δf_2 of 0.47 Hz like in section 5.7.3.

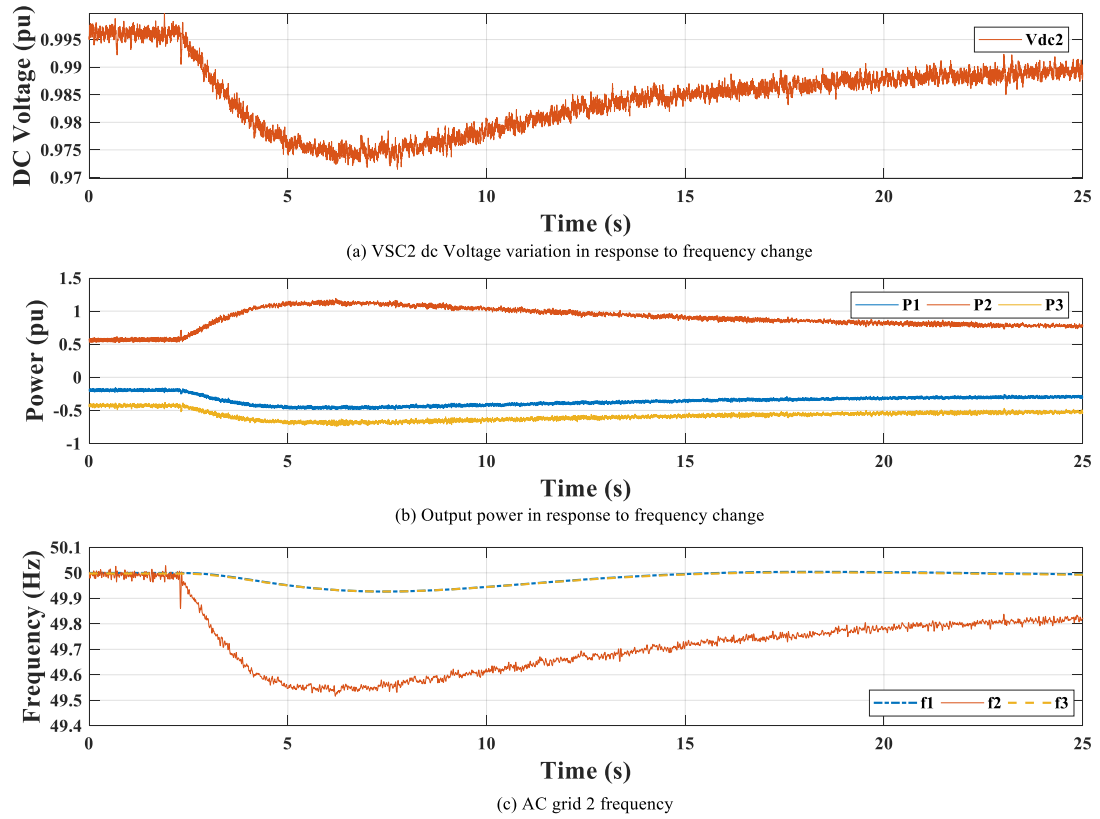


Figure 5.16: Experimental results: System response after loss of 1320 MW (DLC FS fitted in all converters).

5.8 Comparison of Simulation and Experimental Results

A comparison of the PSCAD and experimental results is made in this section. The ADC is fitted with the supplementary controls to enable the responding ac grids to change their dead-bands to 0.1 Hz, while the troubled ac grids keep their dead-band at 0.02 Hz during a frequency disturbance. The experimental results are then compared against the simulation. As the two systems are of different bases, the results are given in per unit, with the base values stated in Table 5.2. This allows for easy comparison between both models. Also, to compare both models, the following success criteria is set

- a) The frequency change in both simulation and experimental should be similar as a result of similar changes in power.
- b) To achieve a similar change in power (per unit) in both systems, the dc voltage will change in both systems. However, due to different bases and

using the same droop constant will cause different changes in voltage. However, these changes in voltage in both experimental and simulation platform must not exceed $0.9V_{dc}$.

- c) DC voltage must change in the same direction i.e. the dc voltage must drop to cause an increase in power to the ac system for both experimental and simulation platforms.

Table 5.2: Experimental and PSCAD base values

	Experiment	Simulation
Power	700 W	1000 MW
AC Voltage	140 V	400 kV
DC voltage	250 V	640 kV
Frequency	50 Hz	50 Hz

Figure 5.17 shows the comparison between the experimental results and simulation results when the supplementary ACC frequency support scheme is fitted in all converters. In Figure 5.17(a), the dc voltage deviation is as a result of the operation of the f - P droops, the dc voltage deviation is non-linear however due to VSC2 and VSC3 entering the frequency sensitive modes around 3.5 s (as seen in the yellow and blue trace of Figure 5.17(c)). In the simulation, this causes the VSC1 to reduce its power export to VSC2, and VSC3 increases its export to compensate for the power reduction from VSC1. In the experimental platform, there is also this non-linear change in the dc voltage when VSC 1 and VSC3 enter the frequency sensitive mode causing a sudden change in the power transferred through VSC1 and VSC3.

The power being supplied to VSC2 in both experimental and simulation results shows agreement as a power increase of about 0.65 pu is seen to flow from VSC 2 to the AC grid in both cases as shown in Figure 5.17(b). Also, the ac grid 2 frequency deviation in both cases shows agreement with a Δf_2 of 0.43 Hz. In this study, where the supplementary frequency controller is fitted in all converters, sudden undesirable changes in the power and dc voltage occur in both experiment and simulations. These could have more negative impact if a worse frequency event

occurs (e.g. a higher increase in demand or loss of generation) and if the system inertia of the onshore ac grids reduces. The dc voltages in both results are unequal as they are a function of the power-voltage droop acting on different voltage bases as defined in the success criteria. Also, they both fail to allow more power flow into GSC2 and do not fall below 0.9p.u.

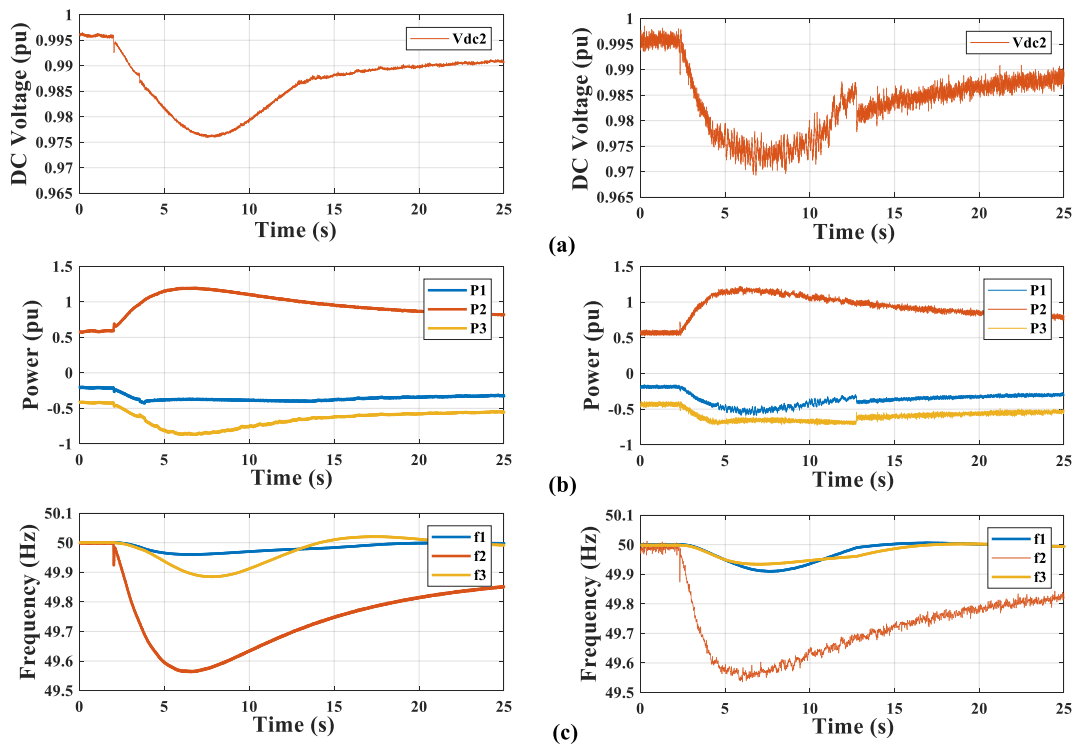


Figure 5.17: PSCAD results (left column) and experimental results (right column) of system response due to 1320 MW generation loss, ACC fitted in all converters. (a) DC Voltage (pu) (b) VSCs 1, 2 and 3 Power (pu) and (c) Frequency of AC Grids 1, 2 and 3.

5.8.1 Experimental Validation of Auxiliary Dead-band Controller

The ADC, discussed in Chapter 4, was fitted with the controls of all three converters in the Simulink interface of the dSPACE control desk. Figure 5.18 shows the simulation and experimental results when the ADC is fitted with the supplementary control schemes. The ADC works to delay the responding converters from entering their frequency sensitive modes unless their Δf and $RoCoF$ are both greater/less than 0.02 Hz and 0.1 Hz/s. Therefore, VSC1 and VSC3 did not enter the frequency sensitive mode despite their frequency dropping above 0.02 Hz.

This allows for a linear change in dc voltage and removes the power oscillations which occurred without the ADC.

The experimental and simulation results show agreement in AC grid 2 frequency deviation and the power flow through VSC2, as shown in Figure 5.18(b) and (c).

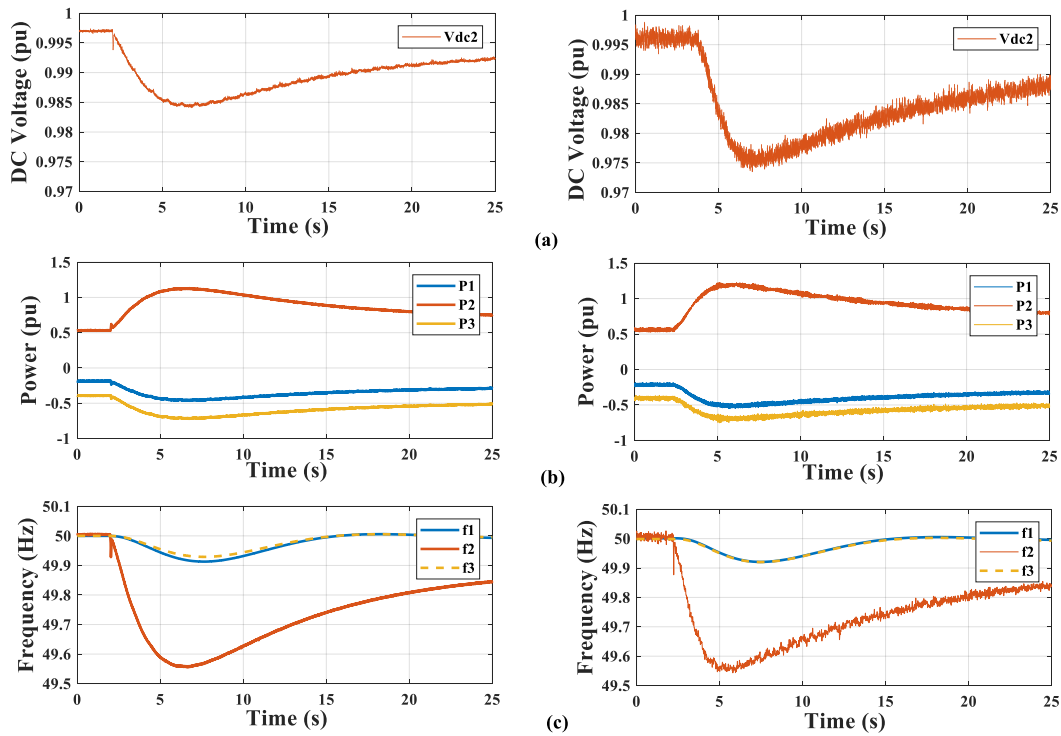


Figure 5.18: PSCAD results (left column) and experimental results (right column) of system response due to 1320 MW generation loss, ACC+ADC fitted in all converters. (a) DC Voltage (pu) (b) VSCs 1, 2 and 3 Power (pu) and (c) Frequency of AC Grids 1, 2 and 3.

5.9 Summary

In this chapter, an experimental RT-HiL platform was introduced, it is made up of RTDS, GS, dc network and a three-terminal VSC-HVDC test rig. The three-machine GB power system was modelled in the RSCAD interface of RTDS and this was connected to the three-terminal VSC system. With the converters operating in droop control, the MTDC grid’s primary operation was demonstrated.

Furthermore, with this experimental platform, the capabilities of the ACC and DLC fast frequency schemes were demonstrated. Tests were carried out when these schemes were fitted in only VSC2 and when fitted in all converters. It was observed

that having ACC frequency support schemes fitted in all converters leads to sudden changes in power and dc voltage when responding to a frequency disturbance. However, in DLC, there were no sudden changes in the power and voltage of the system because the $P-V_{dc}$ droop was always in operation during normal and disturbed modes.

A PSCAD model of the three-machine GB system connected to a three-terminal VSC-HVDC system was also introduced. The ADC was fitted with the ACC scheme and its operations were validated in the experimental platform, it has been proven that with the use of the ADC algorithm, the converters 1 and 3 are delayed from entering the frequency sensitive mode when responding to AC grid 2 frequency disturbance. Finally, the experimental results were compared against the results from the PSCAD model and a very similar response was obtained in both platforms.

Chapter 6

Conclusions

6.1 General Conclusions

An increase in the penetration of renewable energy from offshore wind, solar and other sources is expected soon. HVDC technology will play a major role in integrating this renewable energy with grids and generally aid in the attainment of low carbon energy systems in the future. Also, VSC-based MTDC grids will also allow for the development of super-grids, which allow for trading of energy and ancillary services provision between the grids of different countries. However, for this technology to become reliable and to achieve major deployment, several technical issues need to be addressed. This thesis investigated the effects of reduced inertia due to increasing HVDC and OWF connections.

6.1.1 Inertial contribution from large scale VSWTs

Power electronics in WT's decouple their rotor speed from the network frequency and are seen as inertia-less. Therefore, if a power system is highly penetrated by WT's, there will be a decline in the total power system inertia. Chapter 3 investigated the impact of large-scale connection of Type-4 FPC based variable speed WT's on a power system. To do this, the three-machine GB system was modelled in PSCAD. The inertia contribution at different penetration levels of WT generators connected to the GB system was made. An $x\%$ increase in the penetration from WT's signified an $x\%$ reduction in the power system inertia. With wind capacities of 10% and 20% in the system, the system frequency response was studied following a loss of generation of the largest infeed unit of 1800 MW in the GB system. The studies showed that at higher wind penetration levels, a deeper frequency deviation occurred and with more reduction of inertia, this will affect other parts of operation of the power system such as protection if corrective actions are not taken.

Also, to enable the WT's to provide an inertial contribution to the grid, the TO scheme was introduced and modelled. The impacts of the wind speed, control parameters in the TO scheme and the value of the predefined torque on the frequency support capability were tested. The results showed that at higher wind speeds, more frequency response could be provided, however, the recovery energy was greater. With a higher step in torque, a quick burst of power can be achieved

but it may have a negative impact on the system frequency stability due to a higher recovery energy. With a correct selection of the torque increase, a good reduction in the *RoCoF* and Δf can be achieved. Also, selectively tuning the control parameters of the supplementary controller improves the system frequency response. Therefore, it is concluded that WTs connected to the grid can contribute to the system inertia, but the amount of inertial contribution needs to be carefully selected to avoid the issues of recovery and more frequency decline.

6.1.2 Fast frequency support from MTDC grids and offshore wind farms

It is important to ensure system stability and security with MTDC grids connecting different grids and OWFs. MTDC grids may provide fast frequency support as needed to any of the ac grids connected to it via supplementary control algorithms. In Chapter 4, the coordination of fast frequency support from MTDC grids and OWFs was studied.

A four terminal MTDC system was modelled in MATLAB/Simulink for this study. The effectiveness of 3 supplementary fast frequency control schemes i.e. CC, ACC and DLC was assessed. In literature, most frequency control schemes were only fitted in one converter in an MTDC grid. It was observed that when all converters within the MTDC grid were fitted with the supplementary frequency controllers, an unstable dc grid operation and reduced power transfers between the converters occurred during a power imbalance. This occurred due to multiple frequency oscillations occurring on the different ac systems connected to the MTDC system during provision of frequency support thus activating the supplementary controllers on all grids.

In this thesis, an ADC which uses the Δf and *RoCoF* measurement to determine what ac grid is disturbed i.e. location of the frequency event is proposed. This solution allows each VSC to modify the dead-band setpoint of its local frequency control. This prevents the VSC from entering a frequency sensitive mode when it is not disturbed and allows to control how much the VSCs interact with the

frequency changes. Simulations showed that with the inclusion of the ADC improved system behaviour when responding to power imbalances.

Finally, the small signal stability of the system with the CC scheme fitted to the converters was studied and compared against time domain simulations with good agreement obtained following a 10% step increase in power from the OWF. The effect of the frequency and power droops on the system was studied and it was shown that the frequency droop does not affect the small signal stability of the studied system.

6.1.3 Experimental validation of fast frequency support from MTDC Grids

All solutions made in HVDC and power electronics research intend to drive development of their use in the real world, therefore validation is important. To confirm findings and proposed frequency support schemes and ADC in Chapter 4, RT-HiL experimental tests were carried out. The experimental platform consists of a VSC test rig, dc network, GS and a RTDS. A meshed three-terminal VSC system connecting three onshore ac grids was setup. One of the ac grids was the three-machine GB system which was modelled in the RTDS.

In the experiment, ACC scheme was fitted in all converters and power oscillations due to all converters entering the frequency sensitive mode occurred. This validated the findings in the simulations in Chapter 4. This issue was however removed by fitting the ADC in the converters as in the ACC+ADC scheme. Both simulation and experimental results showed similarities. The test with the DLC scheme fitted in all converters proved the findings in Chapter 4, that the DLC does not require the ADC for stable operation.

The operation of the ADC was therefore validated through these experimental tests. The ADC allows the converters to determine the location of the frequency event and then determine when to enter the frequency sensitive mode through its use of the frequency deviation and derivative measurements. With it fitted to the converters, an MTDC can participate in frequency support to any of the ac grids it is connected to as needed.

6.2 Future Research

Based on the work carried out in this thesis, the following future work are outlined below:

6.2.1 Frequency Support from VSWTs considering varying wind speeds

Offshore wind farms will be geographically distributed around the seas and connected to the grid. Therefore, they will receive winds at different speeds and thus generate different amounts of power. In chapter 3, the studies assumed otherwise for simplification purposes. It is important to study how this variability affects their inertial contribution and capability and recovery power [142], [143].

6.2.2 Small-signal study of reduced 29 bus GB model considering increased VSC-HVDC penetration in grid

In Chapter 4, the small signal stability study only focused on a four-terminal system connected to ac systems modelled as an ideal voltage source with impedance. However, more realistic modelling and representation of ac systems is important, and the 29 bus GB system provides this without too much complexity. In this system, the amount of renewable which can be added to the GB system without causing the system to be unstable can be determined [130], [144]. Also, the effects of having multiple HVDC converters in the GB grid on frequency stability can be determined. The study can also determine the effects of different proposed frequency control schemes on the system stability.

6.2.3 Selective frequency support from onshore ac grids connected to MTDC grids

It is possible that some ac grids may choose to not participate in frequency response i.e. choose not to provide extra power to another onshore grid experiencing frequency imbalance and keep its power constant during this period. This may be because the ac grid at that moment is heavily loaded and providing extra power to another grid may add more stress to its own frequency stability. An algorithm to enable each grid to selectively participate in frequency support can be developed. This control may require fuzzy logic or an algorithm which is able to

determine in real-time the “health” state of the ac grid as a numeric output which is fed to the supplementary frequency droop and determines whether they participate or not [143], [145].

Appendices

Appendix I

Three-Machine GB System Parameters

Tables show the system parameters of the three-machine GB model including the generators' electrical parameters, the governor, turbine and exciter information.

Table A1. 1: Parameters of the three-machine GB system and WTs

	Parameter	Value
England and Wales	Power	21000 MVA
	Inertia constant	5 s
North Scotland	Power	2400 MVA
	Inertia constant	2.89 s
South Scotland	Power	2800 MVA
	Inertia constant	3.84 s
AC Lines	R_{5-7}	1.6 Ω
	L_{5-7}	0.0509 H
	R_{4-7}	0.16 Ω
	L_{4-7}	0.00509 H
	R_{6-7}	0.025465 Ω
	L_{6-7}	0.8 H
AC System	System Frequency (f_b)	50 Hz
	Base Power (S_b)	1000 MVA
	Base Voltage (V_b)	400 kV
WT	Rated Power (S_b)	5 MVA
	WT inertia (J)	$30 \cdot 10^6$ kg·m ²
	Rated wind speed (V_w)	12.5 m/s
	Cut-in and Cut-out wind speeds	4 m/s and 25 m/s
	Pole pairs	125
	Rated AC Voltage	0.69 kV
	Rated DC Voltage	± 600 V

Table A1. 2: Generator parameters (in per unit)

$R_a = 0.002$	$X_d = 2.13$	$X_q = 2.07$	$X_d' = 0.308$
$X_q'' = 0.234$	$T_{do}' = 6.08$ s	$X_q' = 0.906$	$X_d'' = 0.234$
$T_{do}'' = 0.0526$ s	$T_{qo}' = 1.653$ s	$T_{qo}'' = 0.3538$ s	

Table A1. 3: Governor parameters

Permanent Droop $R_p = 0.04 \text{ p.u}$	Minimum Gate Position $G_{\min} = 0.0 \text{ p.u}$
Maximum Gate Position $G_{\max} = 1.0 \text{ p.u}$	Max. Gate Opening Rate MXGTOR = 0.16 pu
Max. Gate closing rate MXGTCR = 0.16 p.u	Reset or Dashpot time constant $T_r = 5.0 \text{ s}$
Servomotor Time Constant $T_p = 0.05 \text{ s}$	Servo Gain $Q = 5.0 \text{ p.u}$
Main servo time constant $T_g = 0.2 \text{ s}$	Temporary Droop $R_t = 0.4 \text{ p.u}$

Table A1. 4: Turbine parameters

Water Starting Time $T_w = 0.3 \text{ s}$	Penstock head loss coefficient $f_p = 0.02 \text{ p.u}$
Turbine Damping Constant $D = 1.0 \text{ p.u}$	Initial Operating Head $H = 1 \text{ p.u}$
Gate Position $G = 1.0 \text{ p.u}$	No load water flow $q_{NL} = 0.05 \text{ p.u}$

Table A1. 5: AC1A exciter

Lead time constant TC = 0.0 s	Lag Time Constant TB = 0.0 s
Regulator Gain KA = 400 p.u	Regulator Time Constant KA = 0.02 s
Max. Regulator Internal Voltage VAMAX = 14.5 p.u	Min. Regulator Internal Voltage VAMIN = -14.5 p.u
Max. Regulator Output VRMAX = 6.03 p.u	Min. Regulator Output VRMIN = -5.43 p.u
Rate Feedback Gain KF = 0.03 p.u	Rate Feedback Time Constant TF = 1.0 s
Exciter Time Constant TE = 0.80 p.u	Exciter Constant Related to Field KE = 1 p.u
Field Circuit Commutating Reactance KC = 0.20 p.u	Demagnetizing Factor KD = 0.38 p.u
Saturation at VE1 SE(VE1) = 0.10 p.u	Exciter Voltage for SE1 VE1 = 4.18 p.u
Saturation at VE2 SE(VE2) = 0.03 p.u	Exciter Voltage for SE2 VE2 = 3.14 p.u

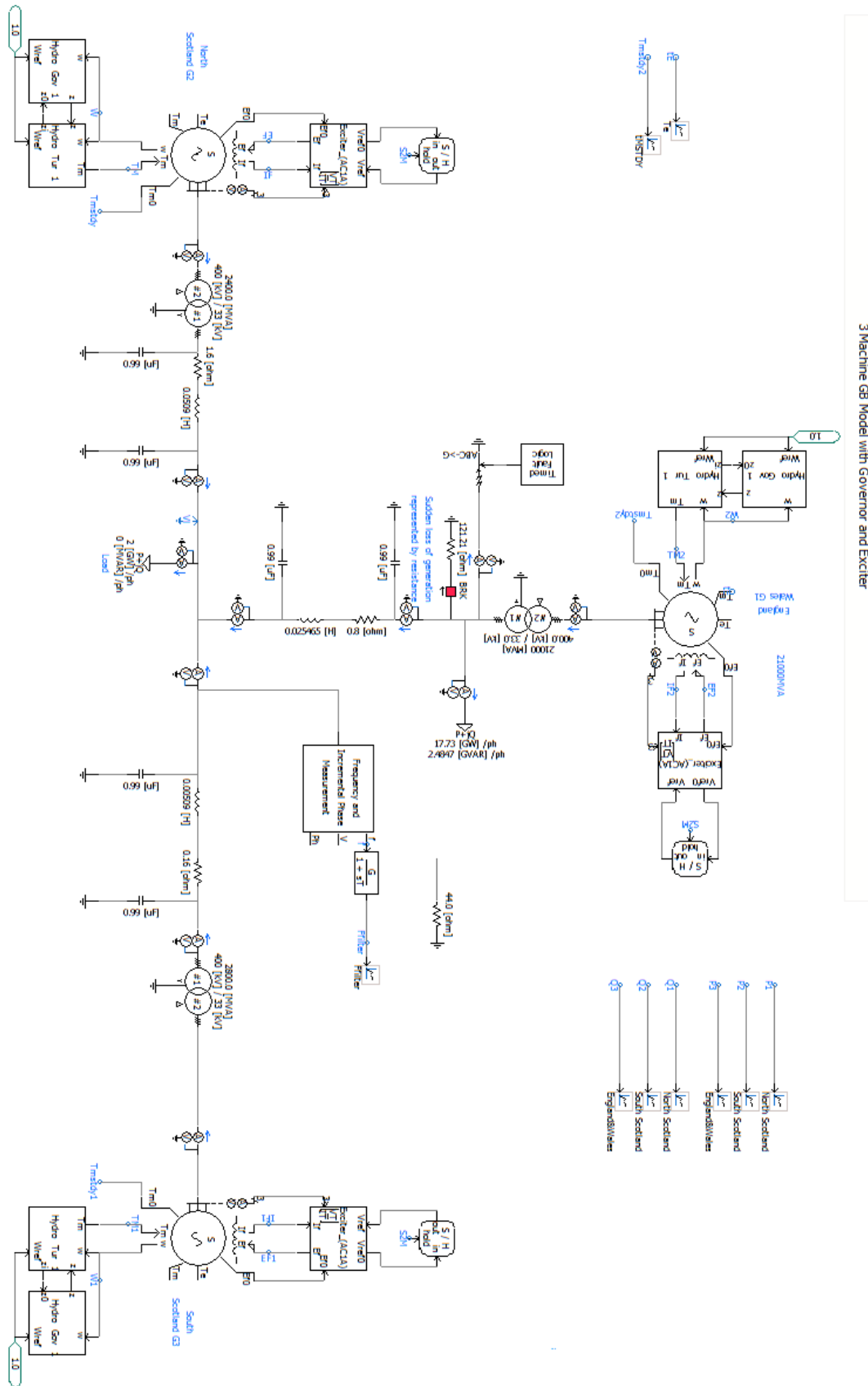


Figure A1. 1: Three-machine GB system in PSCAD

Appendix II

Wind Turbine Parameters

Switching frequency = 2 kHz

Table A2. 1: Back-to-back converters control parameters

Network Side Converter (NSC)	dc voltage control	$k_{p,dc} = 5.9713; k_{i,dc} = 111.5$
	q-axis inner loop control	$k_{pl} = 0.01764; k_{il} = 0.1$
	d-axis inner loop control	$k_{ps} = 0.01764; k_{is} = 0.1$
		$L = 0.01764$ mH
Generator Side Converter (GSC)	Torque control	$\lambda_m = 1.04$
	q-axis inner loop control	$k_{ps} = 14.85; k_{is} = 100$
	d-axis inner loop control	$k_{ps} = 14.85; k_{is} = 100;$ $X_q = 0.28 \Omega; X_d = 0.28 \Omega;$

Table A2. 2: Aerodynamic model parameters

$c_1 = 0.5$	$c_2 = 67.56$	$c_3 = 0$
$c_4 = 0$	$c_5 = 0$	$c_6 = 1.52$
$c_7 = 16.29$	$c_8 = 0.08$	$c_9 = 0.035$
$R = 61$ m	$\beta = 0$	$n_p = 125$
$K_{opt} =$	$J_t = 30 * 10^6$ kg.m ²	Ψ_{pm}
ω_e	L_s	R_s
$f_b = 30$ Hz	$S_b = 5$ MVA	$V_b = 690$ V

Appendix III

4-machine System Parameters

Table A3. 1: Parameters of VSCs and droop coefficients [28].

Converter Parameters	
Power Rating	1000 MW
AC Voltage	380 kV
DC Voltage	± 320 kV
DC Capacitor	223.26 μ F
AC Inductor	11.35 mH
DC Cables	
$L_{GSC1-WFC3}$	43.12 mH
$L_{GSC2-WFC3}$	11.01 mH
$L_{GSC3-WFC3}$	11.01 mH
$R_{GSC1-WFC3}$	1.0752 Ω
$R_{GSC2-WFC3}$	0.2408 Ω
$R_{GSC3-WFC3}$	0.2408 Ω
Supplementary Frequency Control Parameters	
k_{pv}	0.05 kV/MW
$k_{vp} = 1/k_{pv}$	20 MW/kV
k_{fv}	65 kV/Hz
$k_{fp} = k_{fv}/k_{pv}$	1300 MW/Hz
k_{off}	0.025 Hz/kV

Table A3. 2: AC System Parameters [136]

T_g (s)	T_1 (s)	T_2 (s)	T_t (s)	H_{eq} (s)	$1/R_{eq}$ (pu)	D (pu)	Dead-band
0.2 s	2 s	20 s	0.3 s	4.44 s	-11	1	0.0003 pu

Appendix IV

Experimental Parameters

Table A4. 1: VSC test rig specifications.

Device	Specifications	Equipment Rating	Operating Rating
Voltage Source Converters (3 units)	Topology	Two-level, three-phase without neutral wire, IGBT switcher	
	Manufacturer	CINERGIA	
	Rated power	10 kW	2 kW
	Rated ac voltage	415 V	140 V
	Rated dc voltage	800 V	250 V
	DC Capacitors	1020 μ F	
	Coupling Inductor	2.2 mH	
Embedded computer (dSPACE)		DS1005	

Table A4. 2: Real time simulator specifications.

Manufacturer	RTDS Technologies
Racks	2
Cards	2 GTWIF, 4 PB5 (2 GTDI, 2 GTDO, 2 GTAI, 2 GTAQ, 2 GTNET)

Table A4. 3: Grid simulator specifications.

Manufacturer	Spitzenberger
Rating	Continuous: 1 kVA; short-time: 2 kVA
Nominal Voltage	270 Vrms AC; \pm 382 V DC
Power supply	230 V
Input	\pm % V, 8 k Ω , Slew rate: $>$ 52V/ μ s
Protection	16 A

Table A4. 4: Parameters of experimental VSC test rig.

	Parameter	Rating
Converters	Topology	2-level VSCs, symmetrical monopole
	Rated power	700 W
	DC voltage	250 V
	AC voltage	140 V
DC lines	R_{12}	0.26 Ω
	R_{13}	0.78 Ω
	R_{23}	0.98 Ω
	L_{12}	2.4 mH
	L_{13}	5.8 mH
	L_{23}	11.8 mH
DC Capacitors	$C_{vsc1}, C_{vsc2}, C_{vsc3}$	1020 μ F
Droop	k_{pv}	50
	k_{vp}	0.05
	k_{fv}	20
	k_{fp}	1000

Table A4. 5: Technical parameters of MTDC rig in PSCAD.

	Parameter	Rating
Converters	Topology	2-level VSCs, symmetrical monopole
	Rated power	1000 MW
	DC voltage	640 kV
	AC voltage	400 kV
DC lines	R_{12}	1.1926 Ω
	R_{13}	3.58 Ω
	R_{23}	4.49 Ω
	L_{12}	11.01 mH
	L_{13}	26.61 mH
	L_{23}	54.13 mH
DC Capacitors	$C_{vsc1}, C_{vsc2}, C_{vsc3}$	223.46 μF
	k_{pv}	0.02
	k_{vp}	50
	k_{fv}	20
	k_{fp}	1000

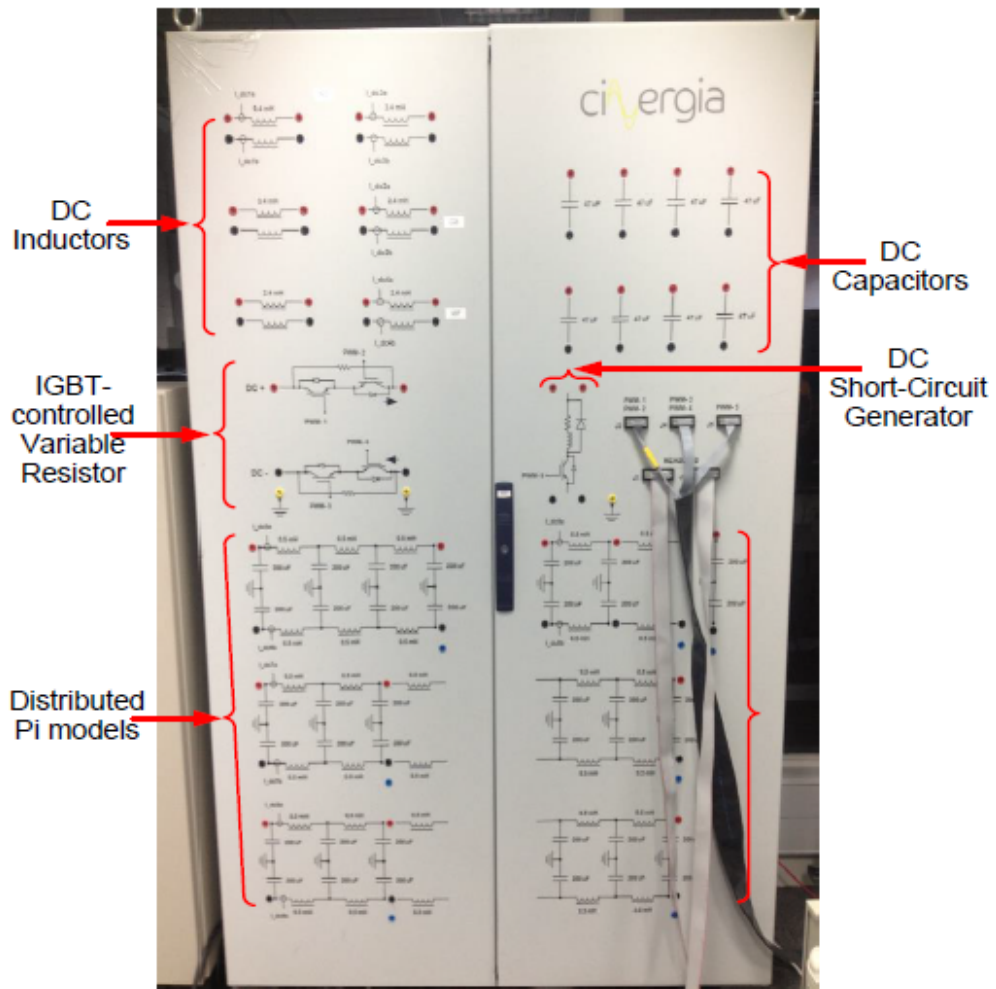


Figure A4. 1: : DC Network Cabinet

DC Network Cabinet Parameters

DC Inductors: 1 pair of 9.4 mH, 2 pairs of 3.4 mH and 3 pairs of 2.4 mH inductors

DC Capacitors: Eight 47µF capacitors

DC Short-Circuit Generator: Diode in parallel with shunt branch connected by an IGBT.

Current flow controller: Two IGBT-controlled variable resistors

Distributed PI models: DC cables with inductors of 0.5 mH and capacitors of 200 µF.

References

- [1] A. Neslen, “Renewables cut Europe’s carbon emissions by 10% in 2015, says EEA | Environment | The Guardian,” 2017. [Online]. Available: <https://www.theguardian.com/environment/2017/apr/03/renewables-cut-europes-carbon-emissions-by-10-in-2015-says-eea>. [Accessed: 28-Aug-2018].
- [2] Ministry of Petroleum and Energy, “Renewable energy production in Norway,” 2016. [Online]. Available: <https://www.regjeringen.no/en/topics/energy/renewable-energy/renewable-energy-production-in-norway/id2343462/>. [Accessed: 01-Jul-2018].
- [3] F. O’Sullivan, “Sweden Could Meet Its 2030 Green Energy Target in 2018 - CityLab,” 2018. [Online]. Available: <https://www.citylab.com/environment/2018/07/sweden-will-meet-its-2030-green-energy-target-12-years-early/565709/>. [Accessed: 04-Sep-2018].
- [4] “Germany powers through 2018 with 42% renewables record,” *Climate Action*, 2018. .
- [5] European Energy Agency (EEA), “Europe’s onshore and offshore wind energy potential: An assessment of environmental and economic constraints,” Copenhagen, 2009.
- [6] WindEurope, “The European offshore wind industry - Key trends and statistics,” *WindEurope*, 2018. [Online]. Available: <https://windeurope.org/about-wind/statistics/offshore/european-offshore-wind-industry-key-trends-statistics-2017/>. [Accessed: 23-Aug-2018].
- [7] GWEC, “Global Wind Report: Annual Market Update 2017,” 2017.
- [8] EWEA, “Wind energy scenarios for 2030,” *EWEA*, pp. 1–8, 2015.
- [9] G. Kuenzel, “Modelling and control of an ACDC system with significant generation from wind,” Imperial College London, 2014.
- [10] ABB, “Why HVDC Economic and environmental advantages - Why choose HVDC over HVAC?,” 2016. [Online]. Available: <http://new.abb.com/systems/hvdc/why-hvdc/economic-and-environmental-advantages>. [Accessed: 23-Aug-2018].
- [11] K. Meah and S. Ula, “Comparative evaluation of HVDC and HVAC transmission systems,” in *2007 IEEE Power Engineering Society General Meeting, PES*, 2007, pp. 1–5.
- [12] D. van Hertem, O. Gomis-Bellmunt, and J. Liang, *HVDC grids for transmission of electrical energy: Offshore grids and a future supergrid*, 1st ed. Wiley, 2016.
- [13] GE Grid Solutions, “High Voltage Direct Current (HVDC) Systems,” 2017.

[Online]. Available:
<http://www.gegridsolutions.com/PowerD/catalog/HVDC.htm>. [Accessed:
23-Aug-2018].

- [14] 50hertz, “Kriegers Flak - Combined Grid Solution,” 2016. [Online]. Available:
<https://www.50hertz.com/en/Grid/Griddevelopment/Offshoreprojects/CombinedGridSolution>. [Accessed: 22-Mar-2019].
- [15] T. M. Haileselassie and K. Uhlen, “Power system security in a meshed north sea HVDC grid,” *Proc. IEEE*, vol. 101, no. 4, pp. 978–990, 2013.
- [16] T. K. Vrana, R. E. Torres-Olguin, B. Liu, and T. M. Haileselassie, “The North Sea super grid - a technical perspective,” in *9th IET International Conference on AC and DC Power Transmission (ACDC 2010)*, 2010, pp. 1–5.
- [17] A. Ulbig, T. S. Borsche, and G. Andersson, “Impact of Low Rotational Inertia on Power System Stability and Operation,” in *Proceedings of the 19th IFAC World Congress*, 2014, pp. 7290–7297.
- [18] National Grid, “System Operability Framework 2016,” 2016.
- [19] R. S. Whitehouse, “Technical challenges of realising multi-terminal networking with VSC,” in *Proceedings of the 2011-14th European Conference on Power Electronics and Applications (EPE 2011)*, 2011, pp. 1–12.
- [20] A. Junyent-Ferré, Y. Pipelzadeh, and T. C. Green, “Blending HVDC-Link Energy Storage and Offshore Wind Turbine Inertia for Fast Frequency Response,” *IEEE Trans. Sustain. Energy*, vol. 6, no. 3, pp. 1059–1066, 2015.
- [21] D. Gautam, L. Goel, R. Ayyanar, V. Vittal, and T. Harbour, “Control strategy to mitigate the impact of reduced inertia due to doubly fed induction generators on large power systems,” *IEEE Trans. Power Syst.*, vol. 26, no. 1, pp. 214–224, 2011.
- [22] Q. Gao and R. Preece, “Improving frequency stability in low inertia power systems using synthetic inertia from wind turbines,” *2017 IEEE Manchester PowerTech*, pp. 1–6, 2017.
- [23] J. Van De Vyver, J. D. M. De Kooning, B. Meersman, L. Vandeveldel, and T. L. Vandoorn, “Droop Control as an Alternative Inertial Response Strategy for the Synthetic Inertia on Wind Turbines,” *IEEE Trans. Power Syst.*, vol. 31, no. 2, pp. 1129–1138, 2016.
- [24] A. D. Hansen, M. Altin, I. D. Margaris, F. Iov, and G. C. Tarnowski, “Analysis of the short-term overproduction capability of variable speed wind turbines,” *Renew. Energy*, vol. 68, pp. 326–336, 2014.
- [25] S. Engelken, A. Mendonca, and M. Fischer, “Inertial response with improved variable recovery behaviour provided by type 4 WTs,” *IET*

- Renew. Power Gener.*, vol. 11, no. 3, pp. 195–201, 2017.
- [26] B. Silva, C. L. Moreira, L. Seca, Y. Phulpin, and J. A. Pecas Lopes, “Provision of inertial and primary frequency control services using offshore multiterminal HVDC networks,” *IEEE Trans. Sustain. Energy*, vol. 3, no. 4, pp. 800–808, 2012.
- [27] S. Akkari, M. Petit, J. Dai, and X. Guillaud, “Interaction between the voltage-droop and the frequency-droop control for multi-terminal HVDC systems,” *IET Gener. Transm. Distrib.*, vol. 10, no. 6, pp. 1345–1352, 2016.
- [28] O. D. Adeuyi, M. Cheah-Mane, J. Liang, and N. Jenkins, “Fast Frequency Response from Offshore Multi-terminal VSC-HVDC Schemes,” *IEEE Trans. Power Deliv.*, vol. 32, no. 6, pp. 2442–2452, 2017.
- [29] J. N. Sakamuri, M. Altin, A. D. Hansen, and N. A. Cutululis, “Coordinated frequency control from offshore wind power plants connected to multi terminal DC system considering wind speed variation,” *IET Renew. Power Gener.*, vol. 11, no. 8, pp. 1226–1236, 2017.
- [30] L. Q. Liu and C. X. Liu, “VSCs-HVDC may improve the Electrical Grid Architecture in future world,” *Renew. Sustain. Energy Rev.*, vol. 62, pp. 1162–1170, 2016.
- [31] P. Kundur, *Power System Stability and Control*, Volume 7. New York: McGraw-Hill, 1994.
- [32] A. Kalair, N. Abas, and N. Khan, “Comparative study of HVAC and HVDC transmission systems,” *Renew. Sustain. Energy Rev.*, vol. 59, pp. 1653–1675, 2016.
- [33] E. Pierri, O. Binder, N. G. A. Hemdan, and M. Kurrat, “Challenges and opportunities for a European HVDC grid,” *Renew. Sustain. Energy Rev.*, vol. 70, no. October 2015, pp. 427–456, 2017.
- [34] DECC, “UK Renewable Energy Roadmap,” 2011. [Online]. Available: <https://www.gov.uk/government/collections/uk-renewable-energy-roadmap>. [Accessed: 25-Jul-2015].
- [35] National Grid, “Future Energy Scenarios,” 2018. [Online]. Available: <http://fes.nationalgrid.com/media/1363/fes-interactive-version-final.pdf>. [Accessed: 30-Jul-2018].
- [36] National Grid, “Future Energy Scenarios: GB gas and electricity transmission,” 2016. [Online]. Available: <http://fes.nationalgrid.com/media/1292/2016-fes.pdf>. [Accessed: 11-Apr-2018].
- [37] National Grid, “Future Energy Scenarios - Data Workbook,” 2018. [Online]. Available: <http://fes.nationalgrid.com/fes-document/>. [Accessed: 20-Aug-2018].
- [38] A. Korompili, Q. Wu, and H. Zhao, “Review of VSC HVDC connection

for offshore wind power integration,” *Renew. Sustain. Energy Rev.*, vol. 59, pp. 1405–1414, 2016.

- [39] GWEC, “Global Wind Report 2016,” *Wind energy technology*, 2017. [Online]. Available: <http://files.gwec.net/files/GWR2016.pdf>. [Accessed: 30-Jul-2017].
- [40] Wind Europe, “A new identity,” 2018. [Online]. Available: <https://windeurope.org/about-us/new-identity/>. [Accessed: 05-Apr-2018].
- [41] J. P. Lyons, M. C. Robinson, P. Veers, and R. W. Thresher, “Wind turbine technology - The path to 20% US electrical energy,” in *IEEE Power and Energy Society 2008 General Meeting: Conversion and Delivery of Electrical Energy in the 21st Century*, 2008, pp. 1–4.
- [42] GE Renewable Energy, “World’s Largest Offshore Wind Turbine | Haliade-X,” 2018. [Online]. Available: <https://www.gerenewableenergy.com/wind-energy/turbines/haliade-x-offshore-turbine>. [Accessed: 05-Apr-2018].
- [43] O. Anaya-Lara, N. Jenkins, J. Ekanayake, P. Cartwright, and M. Hughes, *Wind energy generation: modelling and control*. New York: Wiley, 2009.
- [44] D. Roberts, “Wind turbine power energy blades,” *vox*, 2018. [Online]. Available: <https://www.vox.com/energy-and-environment/2018/3/8/17084158/wind-turbine-power-energy-blades>. [Accessed: 20-Jul-2018].
- [45] Y. Lin, L. Tu, H. Liu, and W. Li, “Hybrid Power Transmission Technology in a Wind Turbine Generation System,” *IEEE/ASME Trans. Mechatronics*, vol. 20, no. 3, pp. 1218–1225, 2015.
- [46] US Department of Energy, “How Does a Wind Turbine Work,” 2014. [Online]. Available: <http://energy.gov/eere/wind/how-does-wind-turbine-work>. [Accessed: 20-Jul-2018].
- [47] N. . Prashanth and P. Sujatha, “Commonly used Wind Generator Systems: A Comparison Note,” *Indones. J. Electr. Eng. Comput. Sci.*, vol. 7, no. 2, pp. 299–311, 2017.
- [48] H. Li and Z. Chen, “Overview of different wind generator systems and their comparisons,” *Renew. Power Gener. IET*, vol. 2, no. 2, pp. 123–138, 2008.
- [49] A. D. Hansen and L. H. Hansen, “Wind turbine concept market penetration over 10 years (1995-2004),” *Wind Energy*, vol. 10, no. 1, pp. 81–97, 2007.
- [50] A. Beainy, C. Maatouk, N. Moubayed, and F. Kaddah, “Comparison of different types of generator for wind energy conversion system topologies,” in *2016 3rd International Conference on Renewable Energies for Developing Countries (REDEC)*, 2016, pp. 1–6.
- [51] J. Serrano-González and R. Lacal-Arantegui, “Technological evolution of onshore wind turbines—a market-based analysis,” *Wind Energy*, vol. 19,

- pp. 2171–2187, 2016.
- [52] M. Michas, “Control of turbine-based energy conversion systems,” Cardiff University, 2018.
- [53] O. Apata and D. T. O. Oyedokun, “Wind Turbine Generators: Conventional and Emerging Technologies,” in *2017 IEEE PES PowerAfrica*, 2017, pp. 606–611.
- [54] Z. Q. Zhu and J. Hu, “Electrical machines and power-electronic systems for high-power wind energy generation applications: Part I – market penetration, current technology and advanced machine systems,” *COMPEL Int. J. Comput. Math. Electr. Electron. Eng.*, vol. 32, no. 1, pp. 7–33, 2012.
- [55] M. Barnes and A. Beddard, “Voltage source converter HVDC links - The state of the art and issues going forward,” *Energy Procedia*, vol. 24, no. December 2012, pp. 108–122, 2012.
- [56] P. Christoforidis, “The Effect of an Embedded VSC-HVDC link on the Transient stability of the Dutch and German Transmission Systems,” Delft University of Technology, 2014.
- [57] D. Tiku, “dc Power Transmission: Mercury-Arc to Thyristor HVdc Valves,” *IEEE Power Energy Mag.*, vol. 12, no. 2, pp. 76–96, 2014.
- [58] C. E. Sheridan, “Assessment of HVDC Technologies for an Offshore MTDC Grid,” Imperial College London, 2015.
- [59] O. E. Oni, I. E. Davidson, and K. N. I. Mbangula, “A review of LCC-HVDC and VSC-HVDC technologies and applications,” in *2016 IEEE 16th International Conference on Environment and Electrical Engineering (EEEIC)*, 2016, pp. 1–7.
- [60] D. Jovcic and K. Ahmed, *High Voltage Direct Current Transmission: Converters, Systems and DC grids*. Wiley-Blackwell, 2015.
- [61] G. Li, “Analysis and Protection of HVDC Systems Subject to AC and DC Faults,” Cardiff University, 2018.
- [62] A. Beddard and M. Barnes, “Modelling of MMC-HVDC systems - An overview,” *Energy Procedia*, vol. 80, pp. 201–212, 2015.
- [63] A. Nami, J. Liang, F. Dijkhuizen, and G. D. Demetriades, “Modular multilevel converters for HVDC applications: Review on converter cells and functionalities,” *IEEE Trans. Power Electron.*, vol. 30, no. 1, pp. 18–36, 2015.
- [64] TBEAenergy, “The World’s First-ever ± 800 kV Modular Multilevel Converter Valve has been Developed,” 2017. [Online]. Available: http://en.tbeaenergy.com/content/details144_1804.html. [Accessed: 15-Jun-2018].
- [65] M. Barnes and A. Beddard, “Voltage source converter HVDC links - The state of the art and issues going forward,” *Energy Procedia*, vol. 24, no.

January, pp. 108–122, 2012.

- [66] ABB, “HVDC Light ® - The original VSC technology Reference list,” 2013. [Online]. Available: https://library.e.abb.com/public/80b8069429b147d984f16c8118027ef4/POW0027_REV25.pdf. [Accessed: 14-Jan-2018].
- [67] J. Cao and J. Y. Cai, “HVDC in China,” in *2013 HVDC and FACTS Conference*, 2013, pp. 539–561.
- [68] ABB, “Skagerrak,” 2015. [Online]. Available: <http://new.abb.com/systems/hvdc/references/skagerrak>. [Accessed: 21-Dec-2015].
- [69] Siemens, “Siemens wins major HVDC order to connect British and Belgian power grid,” 2015. [Online]. Available: [https://www.siemens.com/press/en/pressrelease/?press=/en/pressrelease/2015/energymanagement/pr2015060244emen.htm&content\[\]=EM](https://www.siemens.com/press/en/pressrelease/?press=/en/pressrelease/2015/energymanagement/pr2015060244emen.htm&content[]=EM). [Accessed: 15-Jun-2018].
- [70] I. A. Erinmez, D. O. Bickers, G. F. Wood, and W. W. Hung, “NGC experience with frequency control in England and Wales-provision of frequency response by generators,” *IEEE Power Eng. Soc. 1999 Winter Meet. (Cat. No.99CH36233)*, vol. 1, 1999.
- [71] OFGEM, “Security and Quality of Supply Standard,” 2018. [Online]. Available: <https://www.nationalgrid.com/uk/electricity/codes/security-and-quality-supply-standards>. [Accessed: 19-Nov-2018].
- [72] J. Ekanayake, N. Jenkins, and G. Strbac, “Frequency Response from Wind Turbines,” *Wind Eng.*, vol. 32, no. 6, pp. 573–588, 2008.
- [73] M. Cheng, “Dynamic Demand for Frequency Response Services in the Great Britain Power System,” Cardiff University, 2014.
- [74] J. Licari, J. Ekanayake, and I. Moore, “Inertia response from full-power converter-based permanent magnet wind generators,” *J. Mod. Power Syst. Clean Energy*, vol. 1, pp. 26–33, 2013.
- [75] F. Teng, Y. Mu, H. Jia, J. Wu, P. Zeng, and G. Strbac, “Challenges on primary frequency control and potential solution from EVs in the future GB electricity system,” *Appl. Energy*, vol. 194, pp. 353–362, 2017.
- [76] Y. Mu, J. Wu, J. Ekanayake, N. Jenkins, and H. Jia, “Primary Frequency Response From Electric Vehicles in the Great Britain Power System,” *IEEE Trans. Smart Grid*, vol. 4, no. 2, pp. 1142–1150, 2013.
- [77] National Grid, “Frequency Response Services,” 2018. [Online]. Available: <https://www.nationalgrid.com/uk/electricity/balancing-services/frequency-response-services>. [Accessed: 10-May-2018].
- [78] National Grid, “Enhanced Frequency Response,” 2018. [Online]. Available: <https://www.nationalgrid.com/uk/electricity/balancing-services/frequency-response-services/enhanced-frequency-response->

efr?technical-requirements. [Accessed: 10-May-2018].

- [79] P. Wall and V. Terzija, "Simultaneous estimation of the time of disturbance and inertia in power systems," *IEEE Trans. Power Deliv.*, vol. 29, no. 4, pp. 2018–2031, 2014.
- [80] National Grid, "System Operability Framework 2014," 2014. [Online]. Available: <http://www2.nationalgrid.com/UK/Industry-information/Future-of-Energy/System-Operability-Framework/>. [Accessed: 21-May-2015].
- [81] P. Tielens and D. van Hertem, "Grid Inertia and Frequency Control in Power Systems with High Penetration of Renewables," in *Proceedings of the 6th IEEE Young Researchers Symposium in Electrical Power Engineering*, 2012, pp. 1–6.
- [82] Drax, "Why we need the whole country on the same frequency," 2017. [Online]. Available: <https://www.drax.com/energy-policy/need-whole-country-frequency/>. [Accessed: 20-Aug-2018].
- [83] G. Ramtharan, J. B. Ekanayake, and N. Jenkins, "Frequency support from doubly fed induction generator wind turbines," *Renew. Power Gener. IET*, vol. 1, no. 1, pp. 3–9, 2007.
- [84] National Grid, "System Needs and Product Strategy UK electricity transmission," 2017. [Online]. Available: <https://www.nationalgrid.com/sites/default/files/documents/8589940795-System Needs and Product Strategy - Final.pdf>. [Accessed: 27-Feb-2018].
- [85] National Grid, "System Operability Framework 2015," 2015. [Online]. Available: <http://www2.nationalgrid.com/UK/Industry-information/Future-of-Energy/System-Operability-Framework/>. [Accessed: 29-Jan-2016].
- [86] F. Díaz-González, M. Hau, A. Sumper, and O. Gomis-Bellmunt, "Participation of wind power plants in system frequency control: Review of grid code requirements and control methods," *Renew. Sustain. Energy Rev.*, vol. 34, pp. 551–564, 2014.
- [87] National Grid, "The Grid Code," no. 5. National Grid Electricity Transmission plc, 2018.
- [88] A. B. Attya, J. L. Dominguez-Garcia, and O. Anaya-Lara, "A review on frequency support provision by wind power plants: Current and future challenges," *Renew. Sustain. Energy Rev.*, vol. 81, no. June 2017, pp. 2071–2087, 2018.
- [89] Z. Wu *et al.*, "State-of-the-art review on frequency response of wind power plants in power systems," *J. Mod. Power Syst. Clean Energy*, vol. 6, no. 1, pp. 1–16, 2017.
- [90] J. Zhu, J. M. Guerrero, C. D. Booth, H. Zhang, and G. P. Adam, "A generic Inertia Emulation Controller for multi-terminal VSC-HVDC systems," *2nd IET Renewable Power Generation Conference (RPG 2013)*. Beijing, pp. 1–6, 2013.

- [91] M. Garmroodi, G. Verbic, and D. J. Hill, "Frequency Support From Wind Turbine Generators With A Time Variable Droop Characteristic," *IEEE Trans. Sustain. Energy*, vol. 3029, no. c, pp. 1–1, 2017.
- [92] M. Dreidy, H. Mokhlis, and S. Mekhilef, "Inertia response and frequency control techniques for renewable energy sources: A review," *Renew. Sustain. Energy Rev.*, vol. 69, no. July 2016, pp. 144–155, 2017.
- [93] M. Cheah-Mane, J. Liang, and N. Jenkins, "Permanent magnet synchronous generator for wind turbines: Modelling, control and Inertial Frequency Response," in *2014 49th International Universities Power Engineering Conference (UPEC)*, 2014, no. 1, pp. 1–6.
- [94] J. Licari and J. Ekanayake, "Coordinated inertia response from permanent magnet synchronous generator (PMSG) based wind farms," *J. Natl. Sci. Found. Sri Lanka*, vol. 43, no. 4, pp. 347–355, 2016.
- [95] M. Cheah-Mane, "Frequency Response from DC grids." Barcelona, 2016.
- [96] M. Altin, R. Teodorescu, B. . Jensen, U. . Annakkage, F. Iov, and P. . Kjaer, "Methodology for assessment of inertial response from wind power plants," in *2012 IEEE Power and Energy Society General Meeting*, 2012, pp. 1–8.
- [97] M. Wang-Hansen, R. Josefsson, and H. Mehmedovic, "Frequency Controlling Wind Power Modeling of Control Strategies," *IEEE Trans. Sustain. Energy*, vol. 4, no. 4, pp. 954–959, 2013.
- [98] N. R. Ullah, T. Thiringer, and D. Karlsson, "Temporary Primary Frequency Control Support by Variable Speed Wind Turbines— Potential and Applications," *IEEE Trans. Power Syst.*, vol. 23, no. 2, pp. 601–612, 2008.
- [99] I. M. Sanz, B. Chaudhuri, and G. Strbac, "Inertial Response From Offshore Wind Farms Connected Through DC Grids," *IEEE Trans. Power Syst.*, vol. 30, no. 3, pp. 1518–1527, 2015.
- [100] Z. Miao, L. Fan, D. Osborn, and S. Yuvarajan, "Wind farms with HVdc delivery in inertial response and primary frequency control," *IEEE Trans. Energy Convers.*, vol. 25, no. 4, pp. 1171–1178, 2010.
- [101] Y. Pipelzadeh, B. Chaudhuri, and T. C. Green, "Inertial response from remote offshore wind farms connected through VSC-HVDC links: A Communication-less scheme," in *2012 IEEE Power and Energy Society General Meeting*, 2012, pp. 1–6.
- [102] CIGRE Working Group B4.58, "Control methodologies for direct voltage and power flow in a meshed HVDC Grid," 2017.
- [103] J. Huang and R. Preece, "HVDC-based Fast Frequency Support for Low Inertia Power Systems," in *13th IET International Conference on AC and DC Power Transmission (ACDC 2017)*, 2017, pp. 1–6.
- [104] R. Meere, M. O'Malley, and A. Keane, "VSC-HVDC link to support voltage and frequency fluctuations for variable speed wind turbines for grid

- connection,” in *2013 IEEE PES Innovative Smart Grid Technologies Conference Europe (ISGT Europe)*, 2012, pp. 1–5.
- [105] C. L. Moreira, J. R. Gouveia, and B. Silva, “Participation of multi-terminal HVDC grids in frequency regulation services,” in *2015 9th International Conference on Compatibility and Power Electronics (CPE 2015)*, 2015, pp. 202–209.
- [106] J. Rafferty, L. Xu, Y. Wang, G. Xu, and F. Alsokhiry, “Frequency support using multi-terminal HVDC systems based on DC voltage manipulation,” *IET Renew. Power Gener.*, vol. 10, no. 9, pp. 1393–1401, 2016.
- [107] L. Pan-Dian, Y. Zhi-Chang, C. Sheng, Z. Liang-He, and Y. Fen-Yan, “Review of Frequency Support Control Strategies for Asynchronous AC Systems Connected Through VSC-HVDC,” in *2nd International Conference on Energy, Power and Electrical Engineering (EPEE 2017)*, 2017, pp. 414–421.
- [108] I. M. Sanz, B. Chaudhuri, and G. Strbac, “Frequency changes in AC systems connected to DC grids: Impact of AC vs. DC side events,” in *2014 IEEE PES General Meeting | Conference & Exposition*, 2014, pp. 1–5.
- [109] R. Doherty, A. Mullane, G. Nolan, D. J. Burke, A. Bryson, and M. O’Malley, “An Assessment of the Impact of Wind Generation on System Frequency Control,” *IEEE Trans. Power Syst.*, vol. 25, no. 1, pp. 452–460, 2010.
- [110] A. Žertek, G. Verbič, and M. Pantoš, “Optimised control approach for frequency-control contribution of variable speed wind turbines,” *IET Renew. Power Gener.*, vol. 6, no. 1, p. 17, 2012.
- [111] F. Gonzalez-Longatt, E. Chikuni, and E. Rashayi, “Effects of the Synthetic Inertia from wind power on the total system inertia after a frequency disturbance,” in *IEEE International Conference on Industrial Technology (ICIT)*, 2013, pp. 826–832.
- [112] K. V. Vidyanandan and N. Senroy, “Primary frequency regulation by deloaded wind turbines using variable droop,” *IEEE Trans. Power Syst.*, vol. 28, no. 2, pp. 837–846, 2013.
- [113] A. Junyent Ferré, “Control of power electronic converters for the operation of wind generation systems under grid disturbances,” *Universitat Politècnica de Catalunya*, 2011.
- [114] A. M. Eltamaly and H. M. Farh, “Maximum power extraction from wind energy system based on fuzzy logic control,” *Electr. Power Syst. Res.*, vol. 97, pp. 144–150, 2013.
- [115] J. Licari, C. E. Ugalde-Loo, J. B. Ekayanake, and N. Jenkins, “Damping of Torsional Vibrations in a Variable-Speed Wind Turbine,” *IEEE Trans. Energy Convers.*, vol. 28, no. 1, pp. 172–180, 2013.
- [116] H. Huang, C. Mao, J. Lu, and D. Wang, “Small-signal modelling and

- analysis of wind turbine with direct drive permanent magnet synchronous generator connected to power grid,” *IET Renew. Power Gener.*, vol. 6, no. 1, pp. 48–58, 2012.
- [117] F. Wu, X. P. Zhang, and P. Ju, “Small signal stability analysis and control of the wind turbine with the direct-drive permanent magnet generator integrated to the grid,” *Electr. Power Syst. Res.*, vol. 79, no. 12, pp. 1661–1667, 2009.
- [118] R. Gao and Z. Gao, “Pitch control for wind turbine systems using optimization, estimation and compensation,” *Renew. Energy*, vol. 91, pp. 501–515, 2016.
- [119] M. Asmine, C. Langlois, and N. Aubut, “Inertial Response from Wind Power Plants during a Frequency Disturbance on the Hydro-Quebec System – Event Analysis and Validation,” *IET Renew. Power Gener.*, vol. 12, no. 5, pp. 515–522, 2017.
- [120] D. Caldas, M. Fischer, and S. Engelken, “Inertial Response Provided by Full-Converter Wind Turbines,” in *Brazil Windpower 2015 Conference and Exhibition*, 2015, pp. 1–8.
- [121] IESO, “Market Rules for the Ontario Electricity Market,” 2017. [Online]. Available: www.ieso.ca/sector-participants/market.../1652ccacd9194496ae0b948210ec6b30.ashx. [Accessed: 27-Mar-2018].
- [122] C. E. Ugalde-Loo, J. B. Ekanayake, and N. Jenkins, “Subsynchronous resonance in a series-compensated Great Britain transmission network,” *IET Gener. Transm. Distrib.*, vol. 7, no. 3, pp. 209–217, 2013.
- [123] I. Moore and J. Ekanayake, “Frequency response from wind turbines,” *2009 44th Univ. Power Eng. Conf.*, pp. 1–5, 2009.
- [124] I. Duncan, “Energy Union - Realising a North Sea Energy Grid,” 2015. [Online]. Available: [http://www.ianduncan.org.uk/sites/default/files/Energy Union - Realising a North Sea Grid.pdf](http://www.ianduncan.org.uk/sites/default/files/Energy%20Union%20-%20Realising%20a%20North%20Sea%20Grid.pdf). [Accessed: 23-Dec-2015].
- [125] F. D. Bianchi, J. L. Domínguez-García, and O. Gomis-Bellmunt, “Control of multi-terminal HVDC networks towards wind power integration: A review,” *Renew. Sustain. Energy Rev.*, vol. 55, pp. 1055–1068, 2016.
- [126] J. Liang, T. Jing, O. Gomis-Bellmunt, J. Ekanayake, and N. Jenkins, “Operation and Control of Multiterminal HVDC Transmission for Offshore Wind Farms,” *IEEE Trans. Power Deliv.*, vol. 26, no. 4, pp. 2596–2604, 2011.
- [127] T. Joseph, J. Gonçalves, C. E. Ugalde-Loo, and J. Liang, “Wind-Thermal Generation Coordination in Multi-Terminal HVDC-Connected AC Systems for Improved Frequency Support,” in *13th IET International Conference on AC and DC Power Transmission (ACDC 2017)*, 2017.
- [128] J. Zhu, C. D. Booth, G. P. Adam, A. J. Roscoe, and C. G. Bright, “Inertia

- emulation control strategy for VSC-HVDC transmission systems,” *IEEE Trans. Power Syst.*, vol. 28, no. 2, pp. 1277–1287, 2013.
- [129] K. Liao, Z. He, and B. Sun, “Small Signal Model for VSC - HVDC Connected DFIG - Based Offshore Wind Farms,” *J. Appl. Math.*, vol. 2014, 2014.
- [130] L. Shen, M. Barnes, R. Preece, J. V. Milanovic, K. Bell, and M. Belivanis, “The Effect of VSC-HVDC Control on AC System Electromechanical Oscillations and DC System Dynamics,” *IEEE Trans. Power Deliv.*, vol. 31, no. 3, pp. 1085–1095, 2016.
- [131] N. R. Chaudhuri, R. Majumder, B. Chaudhuri, and J. Pan, “Stability analysis of VSC MTDC grids connected to multimachine AC systems,” *IEEE Trans. Power Deliv.*, vol. 26, no. 4, pp. 2774–2784, 2011.
- [132] G. Kalcon, G. Adam, O. Anaya-Lara, S. Lo, and K. Uhlen, “Small-Signal Stability Analysis of Multi-Terminal VSC-Based DC Transmission Systems,” *IEEE Trans. Power Syst.*, vol. 27, no. 4, pp. 1818–1830, 2012.
- [133] X. Chen, C. Zhang, Q. Huang, and M. Ofori-Oduro, “Small-Signal Modeling and Analysis of Grid-Connected Inverter with Power Differential Droop Control,” *Math. Probl. Eng.*, vol. 2016, 2016.
- [134] X. Hu, J. Liang, S. Member, D. J. Rogers, and Y. Li, “Power Flow and Power Reduction Control Using Variable Frequency of Offshore AC Grids,” vol. 28, no. 4, pp. 3897–3905, 2013.
- [135] P. Rodriguez, E. Rakhshani, A. Mir Cantarellas, and D. Remon, “Analysis of derivative control based virtual inertia in multi-area high-voltage direct current interconnected power systems,” *IET Gener. Transm. Distrib.*, vol. 10, no. 6, pp. 1458–1469, 2016.
- [136] H. J. Yunfei Mu, Jianzhong Wu, J Ekanayake, N Jenkins, “Primary Frequency Response from Electric Vehicles in the GB Power System,” *IEEE Trans. Smart Grid*, vol. 4, no. 2, 2013.
- [137] U. Tamrakar, D. Shrestha, M. Maharjan, B. Bhattarai, T. Hansen, and R. Tonkoski, “Virtual Inertia: Current Trends and Future Directions,” *Appl. Sci.*, vol. 7, no. 654, pp. 1–29, 2017.
- [138] K. Dallmer-Zerbe, E. Spahic, G. Kuhn, R. Morgenstern, and G. Beck, “Fast Frequency Response in UK Grid – Challenges and Solution,” in *13th IET International Conference on AC and DC Power Transmission (ACDC 2017)*, 2017, pp. 1–6.
- [139] T. Joseph, “Operation and Control of Voltage Source Converters in Transmission Networks for AC System Stability Enhancement,” Cardiff University, 2017.
- [140] M. Cheah-Mane, “Offshore Wind Integration through High Voltage Direct Current Systems,” Cardiff University, 2017.
- [141] O. D. Adeuyi, “Grid Connection of Offshore Wind Farms through Multi-

Terminal High Voltage Direct Current Networks,” Cardiff University, 2016.

- [142] L. Wu and D. Infield, “Investigation on the interaction between inertial response and droop control from variable speed wind turbines under changing wind conditions,” *Proc. Univ. Power Eng. Conf.*, 2012.
- [143] L. Miao, J. Wen, H. Xie, C. Yue, and W. J. Lee, “Coordinated Control Strategy of Wind Turbine Generator and Energy Storage Equipment for Frequency Support,” *IEEE Trans. Ind. Appl.*, vol. 51, no. 4, pp. 2732–2742, 2015.
- [144] R. Rabbani, A. F. Zobaa, and G. A. Taylor, “Applications of simplified models to investigate oscillation damping control on the GB transmission system,” *IET Conf. Publ.*, vol. 2012, 2012.
- [145] X. Chen, L. Wang, H. Sun, and Y. Chen, “Fuzzy Logic Based Adaptive Droop Control in Multiterminal HVDC for Wind Power Integration,” *IEEE Trans. Energy Convers.*, vol. 32, no. 3, pp. 1200–1208, 2017.